Master's Thesis

Czech
Technical
University
in Prague

F3

Faculty of Electrical Engineering
Department of Control Engineering

Real-time optimization-based control for dielectrophoresis

Tomáš Michálek
Cybernetics and Robotics

May 2015
Supervisor: Jiří Zemánek

Acknowledgement

First of all, I would like to thank Mr. Jiří Zemánek for his leadership, improving ideas and valuable advice. I would also like to express great gratitude to my family and my girlfriend for their support, patience and calm study environment they provided for me.

Declaration

I declare that I wrote the presented thesis on my own and that I cited all the used information sources in compliance with the Methodical instructions about the ethical principles for writing an academic thesis.

Prague, 10th May 2015

Abstrakt / Abstract

Tato práce popisuje návrh řízení pro bezkontaktní manipulaci s mikro- a mezoskopickými objekty pomocí dielektroforézy. Konkrétně je dokumentován výchozí stav systému založeného na optimalizaci v reálném čase. Řešený problém je dále rozšířen tak, aby byly umožněny současné změny amplitud a fázových posunů napěťových signálů použitých k ovládání. Pro řešení dané optimalizační úlohy je zvolena vhodná numerická metoda a systém je experimentálně ověřen. Použita jsou dvě různá elektrodová pole umožňující pohyb po přímce a ploše. Dále jsou analyzovány a řešeny problémy spojené se škálovatelností systému, jako jsou rostoucí výpočetní nároky a vzájemné silové působení částic.

Klíčová slova: dielektroforéza; řízení polohy mikročástic; optimalizace.

Překlad titulu: Řízení dielektroforézy založené na optimalizaci v reálném čase

This thesis describes the control design for a noncontact manipulation of micro- and mesoscale objects utilizing the dielectrophoresis. Specifically, the currently available system based on an optimization in real-time is documented. The optimization problem is further extended so that changes in both the amplitudes and the phase shifts of the voltage signals are used for actuation. A suitable numerical solver is chosen for the given optimization task and the system is experimentally verified. The two different electrode arrays allowing linear and planar motion are used. Furthermore, the issues related to the system scalability, such as the growing computational demands and mutual particle force interactions, are analyzed and appropriate solutions proposed.

Keywords: dielectrophoresis; microparticle position control; optimization.

/ Contents

Tables / Figures

Chapter 1
Introduction

1.1 Micromanipulation

Precise noncontact manipulation of micro- and mesoscale objects gained a huge interest in the last four decades. The possible applications range from diverse engineering problems (such as micro assembly [1]) to scientific areas of biology and biochemistry [2]. Since lately, a special interest is particularly directed towards the so-called *lab-on-a-chip* devices. Their main characteristic is integration of several functions (like separation, concentration and diagnosis) on a single device. The controlled micromanipulation plays a major role in their function [3].

There are many ways to accomplish this task including optical tweezers [4], ultrasound [5], magnetic sorting (MACS) [6], fluorescence (FACS) [7] or electric field-based approaches. Each of them has its advantages and disadvantages. In this thesis I will deal with a dielectrophoresis (DEP), a subclass of the last mentioned approach. The DEP has currently undoubtedly a great unexplored potential. Owing to the ease with which such a manipulator can be fabricated and the fact that the DEP is non-invasive to the manipulated objects like living cells [8], it can easily become a central part of the lab-on-a-chip devices [3].

1.2 Dielectrophoresis

The DEP is capable of inducing a force on polarizable particles. It usually takes place in a liquid medium. This makes it a very promising method of noncontact manipulation.

The DEP force acting on a manipulated object is in fact a resultant of the well-known Coulomb forces. These arise as a consequence of a dipole (or multi-pole) forming inside the object, while it is located in a spatially nonhomogeneous electric field. That is in our case generated by a set of microelectrodes constituting our manipulator. By changing parameters of voltage signals applied to the electrodes (like frequency, phase shift or amplitude), it is possible to "shape" the electric field. Creating the different electric field inhomogeneities then, as a consequence, influences the forces acting on the manipulated objects. Two basic types of the DEP are distinguished: the conventional DEP (cDEP) and the traveling wave DEP (twDEP). The first term refers to a situation when the force is caused by a field with a spatially varying magnitude, whereas the second term denotes the force arising from a field with a spatially varying phase. The cDEP is further divided into a positive and a negative. The former means, that the particles are attracted towards locations of the biggest electrical field gradient (typically to edges of the electrodes). The latter means that they are repelled from such places. The DEP type is determined by the excitation voltage frequency and material properties of the particle and the medium, namely their conductivity and permittivity. In this work, only the negative DEP will be utilized for the manipulation. More details can be found for example in [3, 9–10] and were also discussed in my bachelor's thesis [11]. In this text I will only state and further use the final formulas for the DEP derived in the mentioned literature.

1.3 State-of-the-art

There can be found a number of relevant works dealing with the dielectrophoretic micromanipulation and focusing on its control point of view. In this section I will summarize the interesting results achieved until now and also highlight the contribution of this work in their context.

Manaresi et al. [12–13] achieved the micromanipulation using a 2D array of 320 × 320 square electrodes fabricated as a part of a CMOS chip and another extra electrode on a lid covering the whole manipulation area. The DEP was used to create the so-called force cages above individual electrodes, in which the particle or particles could be trapped. By changing position of these cages, the manipulation was achieved. However, no precise feedback position control was applied since the sensing was realized just by a sparse distribution of photo-diodes. Manipulation precision is therefore limited to the electrode dimensions. The same method was also earlier demonstrated fora 1D case by the same group [14]. Edwards and Engheta [15] developed the so-called electric tweezers, which are constituted of circular electrodes arranged in a circle around the manipulation area. For N particles, at least $2N + 1$ electrodes are necessary to individually control the forces acting on the objects together with the orientation of the objects. The appropriate voltage values generating the desired forces are found bya numerical optimization. Kharboutly et al. [16–17] used four triangular electrodes pointing towards the center of the manipulation area. Control of the force acting on the particle is realized using an inverted simplified 2D model together with the Newton-Raphson method for finding the proper voltages. Although, manipulation with only one particle was demonstrated, ideas for extending their work for an unlimited planar manipulation were sketched.

This thesis is focused on allowing the DEP micromanipulation to be controlled [18] by means of the voltage phase shifts modulation instead of the amplitude modulation. This approach is advantageous because of the simple implementation – no amplifiers are required compared to the voltage amplitude modulation method. Furthermore, an effort was made to investigate and solve the computational issues related to the system scalability. All of this should direct the system under development towards the high precision large range micromanipulator.

1.4 Goals of the work

The goal of this work is to document and further extend the currently existing control system for 1D micromanipulation using the DEP and a parallel electrode array. This system is capable of the simultaneous and independent manipulation of several polystyrene beads. A method based on the utilization of the inherent system noise for overcoming the controllability issues was tested experimentally. As a result of this previous work there were parts of the software and hardware, which I utilized as the foundations upon which my work is built. Results of the mentioned work were presented also in a journal paper [18], which I coauthored with Jiří Zemánek and Zdeněk Hurák. For convenience, I will use some parts of the text here (with allowance of the coauthors) and mark these passages by the reference number.

The particular problems tackled in this thesis include:

- inspection of the existing approaches to “force allocation” in various force fields,
- extension of the existing optimization problem formulation so that it can find both the amplitudes and the phases of the voltages applied to the electrodes. This would enable the control of both the cDEP and the twDEP,
- selection of a suitable numerical solver that can handle this optimization problem in real time,
- conduction of experiments showing the performance of the control system with the standard parallel and a four-sector electrode arrays,
- investigation of the computational issues related to the increased number of the electrodes and the manipulated particles,
- consideration of the mutual interaction of the particles, including
- the extension of the optimization problem so that it takes into account the uncertainty in the position measurement.

1.5 Link to the previous work

This thesis freely builds on my previous work, which itself culminated in the bachelor’s thesis [11]. Objective of the work was to use a 6×5 matrix microelectrode array for a control of the microobject manipulation. First part of the work dealt with the completion of the hardware setup (design and fabrication of a suitable electrode array connector). In the second part, I created the DEP simulation scheme and utilizing it, I designed a few control algorithms. These were supposed to use just the changes of the electric field phase gradient as a mean of actuation. The final outcome of the work was then a collection of several control algorithms ranging from the simple ones to the more advanced using look-up tables with optimal actions computed in advance (for a discrete set of positions and directions of movement).

Chapter 2

Force allocation approaches

One of the key characteristics of the manipulator scheme described in this thesis (which is by the way common for all the noncontact manipulation approaches) is that at first a force field is generated, which just thereafter causes the objects to move. In a mechanical domain this can be illustrated on an example of a difference between a robot gripper poking a ball on a desk and a robot moving the ball by tilting the whole desk. This general property classifies this approach among a much narrower class of the manipulator systems. Some of the force fields, like the one noticed as an example above, are somehow limited in control (here the force exerted in different locations has always the same direction), however, there exist ones that are almost fully adjustable. As an example can serve an array of controlled omni wheels.

The idea of the object manipulation utilizing the miscellaneous force fields is definitely not new. A number of research groups have already started exploring this subject, which is interesting from both the theoretical and the practical point of view. Applications in a macro as well as micro scale are considered. In the macro scale, the concept itself promises a construction of the manipulation devices which are mostly composed of a large number of identical (and relatively cheap) cooperating units. This allows for a high robustness in cases of a failure of some units, easy reconfiguration of the system or an exchange of broken parts. Various authors proposed their own solutions – some differing in the most basic principles of operation or a physical phenomenon used for exertion of the force field.

Böhringer et al. [19] explored the use of the so-called programmable vector fields for an open-loop positioning and orientation of the distinct objects. By introducing two different types of a static field that can each uniquely pose the object (an ellipsoid potential field and a radial-gravity field), he improved the previous results when several fields had to be employed in a sequence to achieve the same outcome. The only difficulty his method is facing is the unique posing of geometrically symmetric objects. By designing the whole manipulation strategy in open-loop he aimed at a robust and simple practical realization. As a few examples can serve MEMS actuator arrays [20–21], vibrating plates [22] or arrays of motors. The main problem encountered in the micromanipulation systems utilizing mechanical actuation elements is the generation and control of the forces over a sufficiently large range of their magnitude [19].

Suh et al. [20] introduced a first micromachined bimorph organic ciliary array with an on-chip CMOS circuitry. It is composed of 8×8 cells (the so-called motion pixels) each having four orthogonally oriented actuators. These are capable of curling into and out of a substrate plane. This is due to different coefficients of thermal expansion of two different materials making up the structure. The deformation is controlled by a voltage supplied to a heating resistor placed between the two layers. On the manipulation area of 9.4×9.4 mm the authors showed that a force of an arbitrary direction can be exerted on one object by multiplexing the four basic actuation directions. Successful experiments with the squeeze force fields (introduced in [19]) were also performed including a demonstration of the skew squeezed field generated by applying the radial field plus tilting the whole chip by a small angle.

A manipulation principle based on combining horizontal and vertical vibrations was proposed by Frei et al. in [22]. The horizontal circular motion of the whole platform is supplemented with the vertical motion of its individual surface elements (arranged in an array). The vertical elements motion results in a change of the force normal to the surface of the object. If this force changes during one period of the circular horizontal vibratory motion, the total friction force will be nonzero, thus causing the object to move. The device is suitable for both the open-loop and the closed-loop control. In the former case, the theory of vector fields [19] is utilized. An approach based on superposing a uniform field and a moving radial force field centered on the desired position of the traveling object is suggested. This causes the position errors of the object to decrease without the need for sensors and feedback. When using feedback, the use of such squeeze fields becomes superfluous. Multiple objects can then be steered along different trajectories as they are not too close to each other. Possible applications of the proposed device include feeding, orienting, sorting, separating and arranging the objects.

Lunz et al. use an array of motor driven omni wheels for construction of an easy reconfigurable and reprogrammable parcels conveyor system [20]. The manipulated packages are significantly larger than each cell of the system (a unit consisting of four motors). The force fields generated according to [19] are used for the open-loop control. The authors also mention problems arising from the discreteness of the actuator array. The approximation of the generated force field as being continuous causes an undesirable behavior such as unstable rotational equilibria in the system. Thus the closed-loop control is suggested for this type of the manipulator.

The problem of the closed-loop control of a system with many binary degrees of freedom in actuation allocation was investigated in [23] by Fromherz and Jackson. A manipulator system exerting a force on the object by an array of air jets was used as a testing platform for various algorithms solving the force allocation problem. These range from a discrete optimal search to a continuous constrained optimization to a hierarchical approach that can be distributed. The hybrid hierarchical-optimal algorithms represent a general method of solving the high-dimensional problems. A continuous solution can be broken down into a number of similar subproblems. These are either solved through the optimal search or further decomposed.

Konishi at al. focused on the practical aspect related to the control of the array of microactuators [24]. They suggest a distributed control scheme capable of a closed-loop transportation and an orientation of one object by a sequential application of the simple uniform, the squeeze and the rotation vector force fields. Algorithms for coping with possible failures in some clusters of the actuating elements are also presented.

A distributed actuation device consisting of soft gel actuator elements intended for a manipulation with soft objects like organs was proposed by Tadokoro [25]. The driving force is generated by a friction between the manipulated object and the soft drop-like actuators deformable in a controlled manner. The object is carried by a subset of actuators by a small distance while the rest of them is returning to their original position not touching the object. Although it is a very interesting actuation scheme, it is not capable of the manipulation with very soft objects in the present form. The cause is the deformation of the manipulated object itself, which is thus in the permanent touch with all the actuator elements. The net force is therefore zero.

One another interesting way of producing an arbitrary force field for the object manipulation examined Reznik and coworkers [21]. Inspired by the minimalism in robotics they showed that a device with only a few degrees of the actuation freedom can independently manipulate several objects. In fact, they show that the number of the actuators can be traded for a more sophisticated control. By using the small number of actuators this work totally differs from all the previous solutions. The proposed approach uses a horizontally-vibrating plate moving the objects via frictional interactions (of the sliding type). By appropriately modulating the vibrations of the desk (using just four voice-coil actuators) they are capable of the independent manipulation of a theoretically unlimited number of objects.

Let me pinpoint some of the recognized key properties of all these devices, based on which it is possible to categorize them. These are:

- typical dimensions of the manipulated objects,
- need for sensors (closed-loop/open-loop control strategies),
- number of actuators (robustness/minimalism),
- actuator-object relationship (Does one actuator influence more objects at the same time and is one object influenced by more actuators at the same time? Or is there an isolation in the sense that one actuator can only influence one object like it is usually in the mechanical actuator systems?),
- possibility of an easy extension of the manipulation area.

Chapter 3
Current control system

This chapter documents the control system being available before I started writing my thesis. I participated on its creation by implementing the control algorithm and conducting the experiments. The basic capabilities of this control system were already briefly mentioned in the previous text. For a more complete image of the current manipulator function I will describe it once again here in a greater detail. I will, however, still omit the technical details of the laboratory setup which are not necessary for the most fundamental understanding. These are further detailed in Section 6.1.

3.1 Control for the parallel array

The current manipulator is capable of steering one or even more polystyrene test beads (50 µm in diameter) along a straight line using the DEP. The manipulation itself takes place in a small chamber cut out of a polydimethylsiloxane (PDMS) sheet and filled with a deionized water, in which the beads are immersed. Its bottom is covered by the actuators — microelectrodes on a glass substrate (see Figure 6.1). The limitation to just 1D motion control arises from the used microelectrode arrangement. The simple configuration of eight parallel electrodes is used. For the illustration of the described system, see Figure 3.1. By applying appropriate voltages to the individual electrodes, the DEP force acting on the particle is induced and it starts to move. The core problem here is to find a way how to determine the voltage values, such that the induced force acting on the particle has the desired magnitude and direction. This is the responsibility of the proposed controller. The input to the controller is the particle position and the force value we want to affect it. The output is then the set of the appropriate voltages that should be applied to the electrodes. The particle position is measured using a microscope with mounted camera providing a top view image of the manipulation area. The images acquired from the camera are processed on a PC by a computer vision algorithm and the position of the particle is extracted. Only the x of the two coordinates of interest can be measured [18].

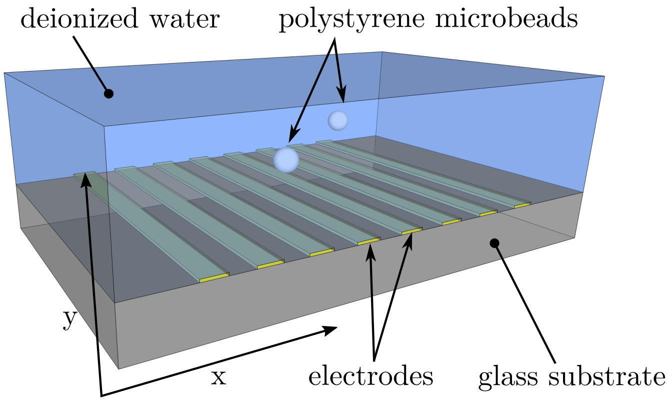

Figure 3.1. Illustration of the parallel array manipulator. Redrawn from [18].

Although it is possible to move the bead by dragging it along the bottom surface, it is much more practical to levitate it (by overcoming the sedimentation force). Then it can be moved in some height above the electrodes and parallel to the glass substrate. This way, it is prevented from sticking to the bottom, which otherwise regularly happens. In such a case, the particle stays static and do not respond to the generated force. The other good reason for maintaining the bead levitating is a better accuracy of the mathematical model in a greater distance from the electrodes (a consequence of the point-dipole approximation, see 4.2). The role of the model in the control algorithm will be discussed further below.

Now, when the basic understanding of the overall system function was established I will proceed with the description of the control strategy itself. Since we are interested in controlling the movement of the bead arising from the DEP force effect, it would be convenient for us to be able to directly dictate this force. The control problem would be then separable into two actually independent parts: **computation of the desired force** and **the desired force allocation**. The DEP force is, however, nonlinearly dependent on the voltages applied to the electrodes and on the position of the particle.

Initially, we will elaborate the first stated subproblem. The used micro beads have negligible inertia [26] and their velocity is thus determined simply as their terminal velocity in the viscous fluid medium. This can be computed using the Stokes' law

$$\mathbf{F}_{\mathrm{d}} = 6\pi\mu r\mathbf{v}, \tag{3.1}$$

where the frictional force $\mathbf{F}_{\mathrm{d}}$ is equal to the force acting on the particle. The symbol μ denotes the dynamic viscosity of the fluid, r is the radius of the spherical particle and $\mathbf{v}$ the flow velocity relative to the object. The bold symbols are used to represent vectors and matrices. The first subproblem thus leads through this simple force-velocity connection to a linear system

$$\begin{bmatrix} \dot{x} \\ \dot{y} \end{bmatrix} = \frac{1}{6\pi\mu r}\begin{bmatrix} F_x \\ F_y \end{bmatrix}, \tag{3.2}$$

and can be controlled by even the most simplest proportional controller.

The second stated subproblem is much more challenging. We start with building up a very simple model of the DEP based on the point-dipole approximation. Since in this case the electric field is constant along the electrodes, it is sufficient to consider just a planar cross-section of the array. Then x represents the coordinate along the horizontal direction orthogonal to the electrodes and y stands for the levitation height (this coordinate system is also shown in Figure 3.1. Nevertheless, if necessary, the presented algorithm can also be extended to the third dimension by simply adding the z coordinate.

The principle of superposition is applied to express the electric field potential at the given coordinates (x, y) as

$$\Phi(x,y) = \sum_i u_i \Phi_i(x,y) = \bar{\mathbf{u}}^T \bar{\mathbf{\Phi}}(x,y), \quad i = 1, 2, \dots, 8, \tag{3.3}$$

where u_i denotes the voltage on the ith electrode and $\Phi_i(x,y)$ is the potential corresponding to a unit voltage applied to the ith electrode while the rest of them is kept at zero. The calculation of these potentials was done by numerically solving the Laplace's equation using a solver for the finite elements method (FEM), namely Comsol Multiphysics (version 4.3). The second part of the expression is just a matrix-vector form of the same. Variables with a bar placed over them then denote a special kind of vectors where each element corresponds to one electrode. Knowing the potential, it is possible to express the vector of the electric field intensity [18]

$$\mathbf{E}(x,y) = \begin{bmatrix} E_x(x,y) \\ E_y(x,y) \end{bmatrix} = -\nabla\Phi(x,y), \tag{3.4}$$

where

$$E_a(x,y) = -\bar{\mathbf{u}}^T \frac{\partial\bar{\boldsymbol{\Phi}}(x,y)}{\partial a} = \bar{\mathbf{u}}^T\bar{\mathbf{E}}_a, \quad a \in \{x,y\}. \tag{3.5}$$

Finally, the time-averaged conventional DEP force acting on the spherical homogeneous particle of the radius of r is [10]

$$\mathbf{F}_{\mathrm{cDEP}}(x,y) = \begin{bmatrix} F_{\mathrm{cDEP},x}(x,y) \\ F_{\mathrm{cDEP},y}(x,y) \end{bmatrix} = k\nabla\mathbf{E}^2(x,y), \tag{3.6}$$

where k is a real constant dependent on the voltage frequency and the material properties of both the particle and the medium. Specifically,

$$k = \pi\varepsilon_{\mathrm{m}} r^3 \mathcal{R}\left[\frac{\varepsilon_{\mathrm{p}}^* - \varepsilon_{\mathrm{m}}^*}{\varepsilon_{\mathrm{p}}^* + 2\varepsilon_{\mathrm{m}}^*}\right], \quad \varepsilon_{\mathrm{r}}^* = \varepsilon_0\varepsilon_{\mathrm{r}} - j\frac{\sigma}{\omega}, \tag{3.7}$$

where ε^* is the so-called complex permittivity with the subscripts p and m standing for the particle and the medium, respectively. Further, ε_0 is the permittivity of the vacuum, ε_{r} is the relative permittivity of the particular material, σ is its conductivity, ω is the angular frequency of the applied sinusoidal voltage and finally j denotes the imaginary unit, that is $j = \sqrt{-1}$. The operator $\mathcal{R}[\cdot]$ denotes the real part of the complex number in the parenthesis. Similarly, $\mathcal{I}[\cdot]$ will be later used to denote the imaginary components of complex numbers. The particular complex fraction present here is commonly called the Clausius–Mossotti factor.

Apart from the above mentioned assumptions, Eq. (3.6) does not take into account any mutual particle force interactions. At least for now, we will consider them as being negligible, which implies that the particles cannot be located close to each other. Next, we continue by expressing the individual force components. First, the differentiation is carried out and new symbols Ψ_{ab}, representing the partial derivatives of the a-component of electric intensity along b, are introduced

$$\bar{\boldsymbol{\Psi}}_{ab} = \frac{\partial\bar{\mathbf{E}}_a(x,y)}{\partial b}, \quad a,b \in \{x,y\}. \tag{3.8}$$

All is then again stated in the vector form

$$\begin{aligned} F_{\mathrm{cDEP},a}(x,y) &= 2k\left(E_x\frac{\partial E_x}{\partial a} + E_y\frac{\partial E_y}{\partial a}\right) = \\ &= 2k\left(\bar{\mathbf{u}}^T\bar{\mathbf{E}}_x\bar{\mathbf{u}}^T\bar{\boldsymbol{\Psi}}_{xa} + \bar{\mathbf{u}}^T\bar{\mathbf{E}}_y\bar{\mathbf{u}}^T\bar{\boldsymbol{\Psi}}_{ya}\right), \quad a \in \{x,y\}, \end{aligned} \tag{3.9}$$

utilizing the fact that by transposition of a scalar we get the same scalar, it is possible to factor out the vectors $\bar{\mathbf{u}}$ and $\bar{\mathbf{u}}^T$ and to express the force components as the quadratic forms

$$F_{\mathrm{cDEP},a}(x,y) = \bar{\mathbf{u}}^T \underbrace{2k\left(\sum_{b=x,y}\bar{\mathbf{E}}_b\bar{\boldsymbol{\Psi}}_{ba}^T\right)}_{\mathbf{P}_a}\bar{\mathbf{u}}, \quad a \in \{x,y\}. \tag{3.10}$$

Now the task is to find the potentials $\bar{\mathbf{u}}$ on the electrodes that will yield the desired DEP force at a given place. This can be formulated as an optimization task

$$\begin{aligned} \bar{\mathbf{u}}^{\mathrm{opt}} &= \arg\min_{\bar{\mathbf{u}}} \left(\left| \bar{\mathbf{u}}^T \mathbf{P}_x(x,y)\, \bar{\mathbf{u}} - F_x^{\mathrm{des}} \right| + \left| \bar{\mathbf{u}}^T \mathbf{P}_y(x,y)\, \bar{\mathbf{u}} + F_{\mathrm{sed}} - F_y^{\mathrm{des}} \right| \right), \\ &\quad \text{s. t. } \ |u_i| < U_{\max}, \end{aligned} \tag{3.11}$$

where ${F_x}^{\mathrm{des}}$ and ${F_y}^{\mathrm{des}}$ are the appropriate components of the desired force and F_{sed} is a sedimentation force acting on the particle. This way, it is possible to obtain voltages $\bar{\mathbf{u}}^{\mathrm{opt}}$ necessary to induce the given force. The optimization task is therefore solved once in every control period. Since the $\mathbf{P}_a$ matrix is in general indefinite, the optimization problem is not convex. For solving it we use an implementation of a simulated annealing algorithm in Matlab (the code written by J. Vandekerckhove is freely available [27]). Further details regarding the optimization solver choice can be found in Chapter 5 devoted to the analysis of the optimization task. In [28], it was presented how this procedure could also be interpreted as being a very close to a feedback linearization concept [18].

Sample results of the optimization for the particular desired force are shown in Figure 3.2. There are four side views of a part of the manipulation area containing the particle. The particle is represented by a circle and its position differs as well as differ the desired forces (shown by the red arrows). The blue arrows then mark the actual forces generated by the solution of the optimization task. Although the two arrows do not overlap perfectly, this performance is sufficient to be used in the feedback controller for the real system (see Chapter 6). The background color represents the electric potential field [18].

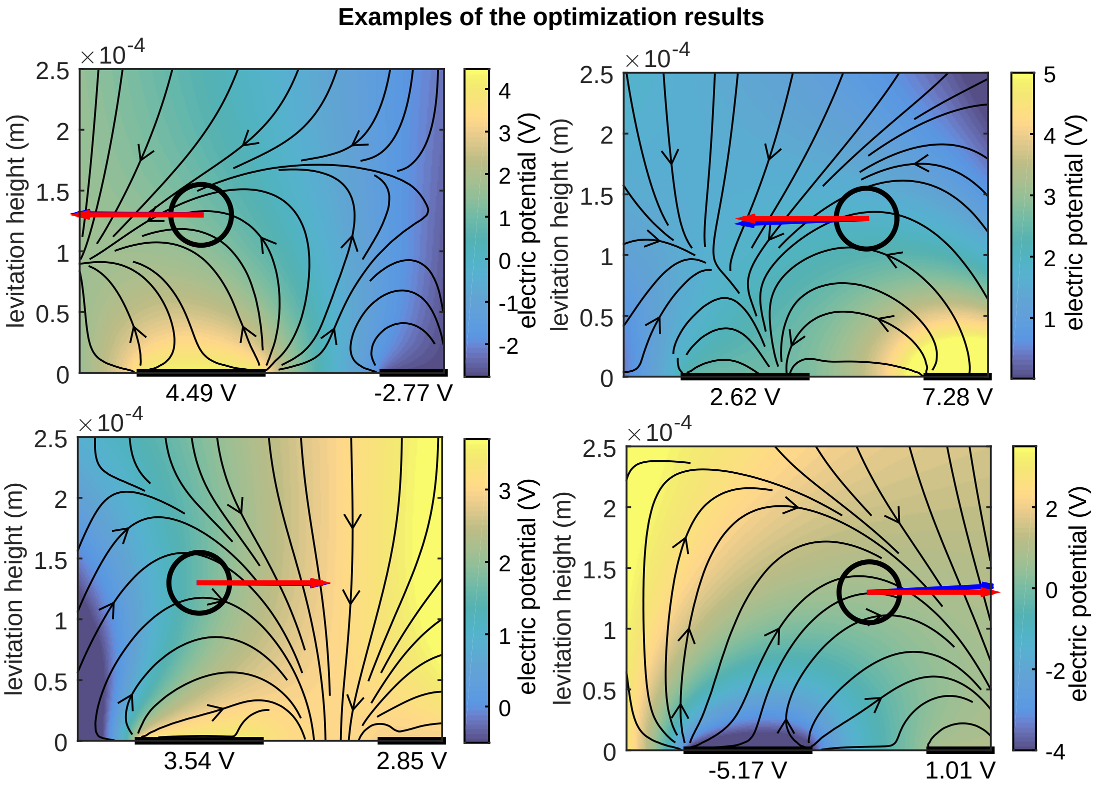

Figure 3.2. Four examples of the optimization outcomes. Redrawn from [18].

Since only the horizontal position x is currently measured and provided to the controller, the levitation height y of the particle is tried to kept constant at the initial level by the controller throughout the whole experiment. A way of doing this is by fixing the F_y^{des} component of the desired force vector at zero. This assumes that the initial levitation height is known, the mathematical model based on which the voltages are determined is totally accurate and a zero error solution is found by the optimization task. This is of course never the case. The problem would fade away if we would be able to measure the levitation height during the experiment, so that the controller would have access to it. Not only this would greatly help in steering the particle in the x axis, but it would also immediately allow the positioning in the y axis [18].

Another problem is that the measured horizontal position reaches the controller with some non-negligible delay. It takes a finite time to acquire the image, process it and execute the control algorithm. This delay should be compensated, because otherwise it could cause an undesired behavior like oscillations. We tackle this problem using a position estimator. The estimation of the horizontal position is calculated as the last known position plus the last known velocity times the duration of the delay (approximately measured as 25 ms) [18].

Prior to the experimental validation, the position control algorithm was tested in a spirit of the software-in-the-loop (SIL), with the plant simulation based on the mathematical model described above. We simply plug in the control signals into the force Eq. (3.10) and calculate $\mathbf{F}_{DEP}$. Knowing the force exerted on the particle, the Stokes' law is used to get the following relationships for the bead movement

$$\dot{x} = \frac{1}{6\pi\mu r}\bar{\mathbf{u}}^T\mathbf{P}_x\left(x,y\right)\bar{\mathbf{u}}, \quad \dot{y} = \frac{1}{6\pi\mu r}\left[\bar{\mathbf{u}}^T\mathbf{P}_y\left(x,y\right)\bar{\mathbf{u}} + F_{\mathrm{sed}}\right]. \tag{3.12}$$

Furthermore, an artificial small noise can be added to the particle velocities representing the effects of the not modeled Brownian motion and alike phenomena. These are in the most of the cases insignificant in comparison with the DEP force effects, but useful in the situations described in the subsequent Section 3.2. Although, we are simulating the position evolution in the both relevant axes to make the simulation as much realistic as it is possible, we of course respect that only the x coordinate is measured in the real experimental setup and do not provide any other information to the control algorithm. The movement along the third remaining axis (in direction parallel to the electrodes and the bottom plane) is not important in the current situation, because the DEP force should not vary in this direction. In fact, some movement which is probably caused by thermal generated fluid flows occurs, but it is negligible in comparison with the studied DEP induced motion so it is unconsidered in the model. A schematic diagram of the whole SIL simulation is in Figure 3.3.

Both the control algorithm and the plant simulation were implemented in Simulink by means of S-function blocks. The controller block runs at a frequency of 10 Hz resembling the real experiment conditions, where we are limited by real-time capabilities of the hardware. The plant simulation, solving the equations (3.2) using standard `ode45` solver, is executed with a frequency ten times higher to capture the bead position evolution even in the course of one control period. Furthermore, the components introducing artificial delays on the inputs (caused by frame grabber and the image processing blocks) and the outputs (possibly caused by the driving circuitry) are included. All the delays can be grouped and represented just as a one block preceding the control algorithm itself. The predicted value x_{pred} is then in fact not the estimate of the *current* position of the bead, but the estimate of its *future* position (at the time the control signals propagate to the electrodes).

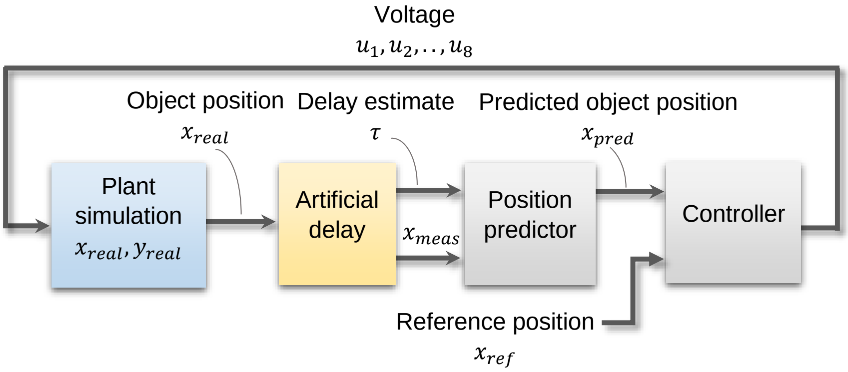

Figure 3.3. Schematic diagram of the SIL simulation. The blue block simulates the physical system (the DEP and the particles), the yellow block simulates the driving circuitry (the delay on the inputs and the outputs) and the grey block is the control algorithm itself.

In Figure 3.4 a simulation of a position reference tracking is shown. The upper graph depicts the time progress of the position of the object in the direction of the horizontal axes x and the lower one displays its levitation height. While the horizontal position can be measured and thus controlled in the closed feedback loop, the vertical position can be controlled only in the open-loop as noted above. The deviations from the desired levitation height of 130 µm are small in the steady-state regions, but increase when the bead moves. However, the feedback controller of the x position still achieves a maximal overshoot of around 12 µm and a maximal deviation from the reference in the steady state of 5 µm (that is 10 % of the particle diameter).

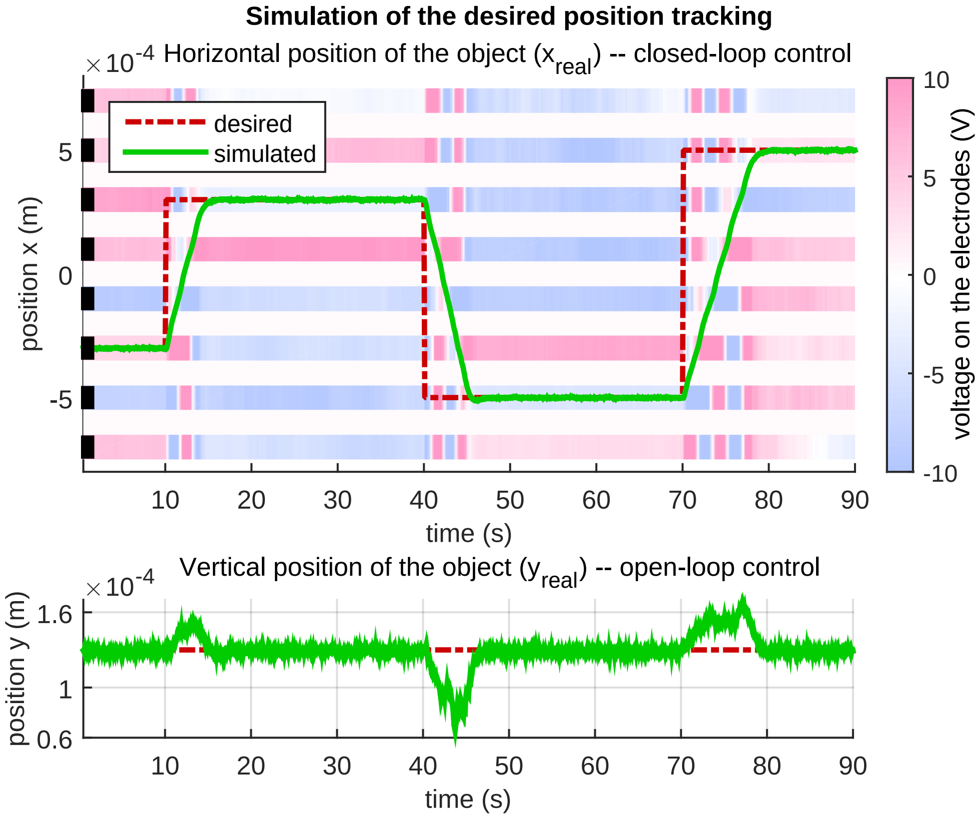

Figure 3.4. Simulation of the reference tracking. The horizontal position is controlled in the closed feedback loop while the vertical one just in the open-loop. The underlying colored stripes represent the voltage amplitudes applied to the electrodes.

Another example in Figure 3.5 shows that the bead can be steered and kept at any desired location (not only the centers or the edges of the electrodes). The experimental results verifying the simulation predictions are described in Section 6.

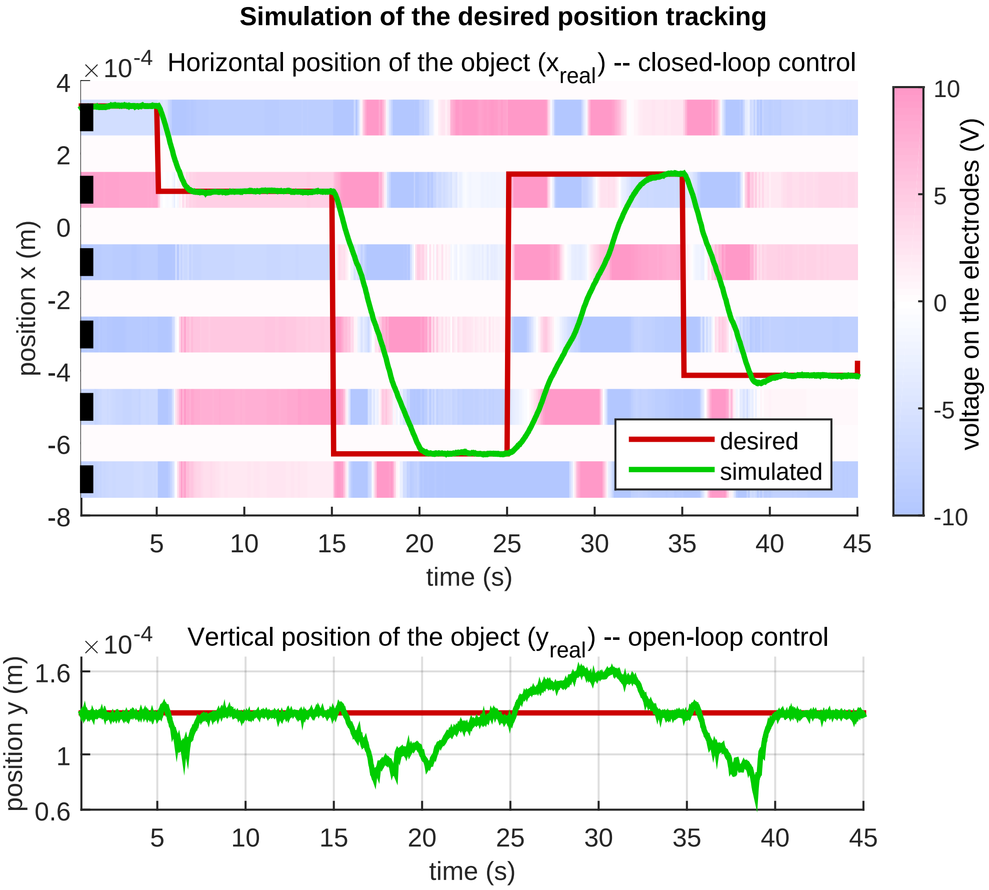

Figure 3.5. Simulation of the reference tracking with randomly chosen reference positions. The color stripes represent the voltage amplitudes applied to the individual electrodes.

3.2 Parallel manipulation of several particles

The presented optimization-based approach can be extended to an independent manipulation of several particles at the same time. It is sufficient to simply supplement the optimization task definition (3.11) by other force requirements. So, if in the current situation the minimization of the two norms is necessary for controlling just one particle (one for each significant force component), for N particles there would be a sum of $2N$ similar norms in the objective function.

Leaving aside the fact that not all the desired forces can be achieved because of the constraints imposed on the voltage amplitudes, other limitations can arise from the array geometry itself. Not only that the parallel electrode array does not allow to control the movement of the objects in the direction along the third axis z (because the corresponding DEP force component is zero), the DEP force components for the directions along the other two axes remain constant along the given z coordinate. This brings some controllability issues when dealing with the control of more particles. Imagine a situation when two identical particles (the same volume, density, permittivity, conductivity, ...) should swap their positions in the x coordinate. The control algorithm would start moving them in the corresponding directions and this would work until they reached the same x coordinate. Assuming that their levitation height is the same, both the particles would now feel an identical force. This in conjunction with the negligible inertia of the particles causes the loss of the controllability – a problem that can not be solved by any deterministic control algorithm [18].

A simple, however probabilistic, solution can be offered. First, a stable force equilibrium is used to bring the beads to the same x coordinate position as it is illustrated by a potential well in Figure 3.6. This is done naturally by the current form of the controller. Then the equilibrium is changed to an unstable. The corresponding potential illustration is shown in Figure 3.7. In this position, only a small disturbance (intrinsic in the system) is sufficient to cause the particles to move down the created potential hill. In total, there exist four possible results: both the particles will move to the left, both the particles will move to the right, one particle will move to the left and the second to the right and the other way around. Only one of these possibilities leads to the desired particle swap. If any other situation comes to pass, the whole process of using the stable and then the unstable force equilibrium repeats, until the positions of the beads are successfully exchanged. Not only the stable, but also the unstable force equilibrium is created naturally by the current form of the controller. The optimization task chooses it as the best compromise between the two desired forces acting in the opposite directions. This equilibrium is however too weak to be useful for the separation process. Therefore the situation where the separation is necessary is detected (it is sufficient to look whether the two particles are at the same x coordinate and want to move in opposite directions) and a stronger equilibrium is artificially generated [18].

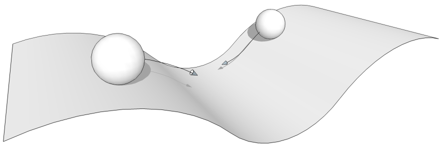

Figure 3.6. An illustration of the stable equilibrium attracting the particles to the same location. Taken from [18].

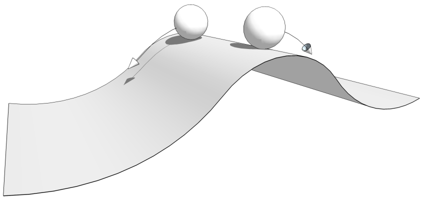

Figure 3.7. An illustration of the unstable equilibrium repulsing the particles on its two sides. Taken from [18].

The above described procedure of the position swapping of the two particles is shown in the SIL simulation in Figure 3.8. The position controller first brings them together and then the procedure of the separation begins (it is indicated by the green area). The algorithm is separating the particles by creating the unstable equilibrium at their (shared) position. In particular, three forces are set for the optimization. Zero force is demanded in the position of the particles and two forces pointing away from this location are set on either side of the particles. Their magnitude is rather large (100 pN) and their points of activity are separated by a distance of 40 µm. The desired forces are depicted by arrows and crosses. If the separation is not successful, the position controller tries to bring the particles together and the procedure of separation starts again. The procedure finishes when the particles are far away (100 µm). Experimental results demonstrating the independent manipulation with up to three particles are shown in Section 6.

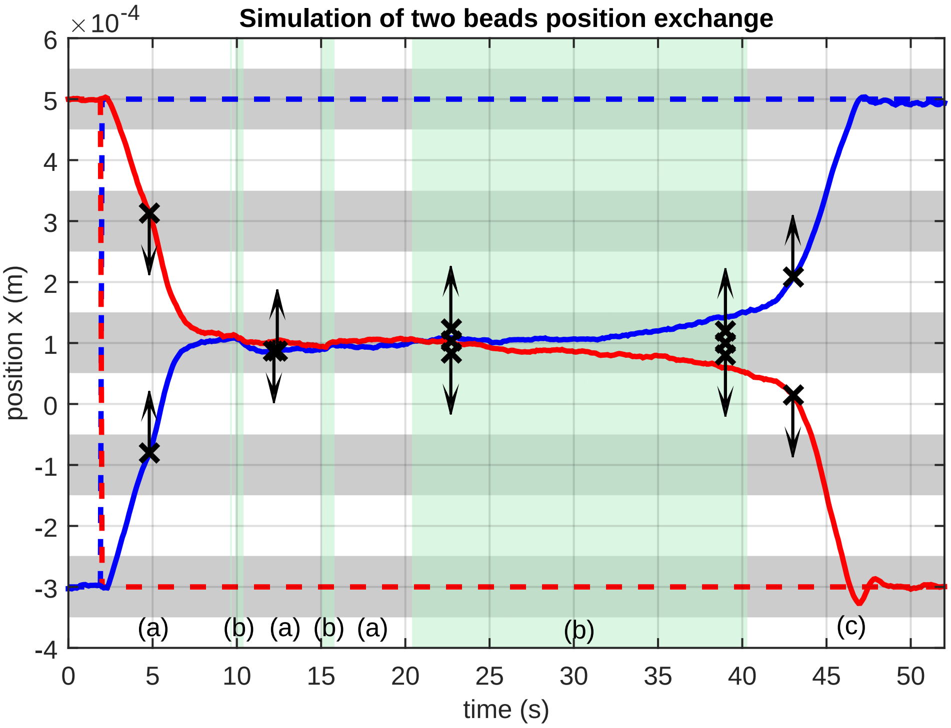

Figure 3.8. Simulation of the particles swapping their positions. (a) First, they are brought together, (b) and then the procedure of the separation begins (indicated by the green color). If it is not successful, it stops and the particles are brought again together. (c) It finishes when the particles are separated by some predefined distance. The arrows represents the desired forces at the locations of the black crosses. [18].

Chapter 4

Phase control

In the current setting, the only parameter that is used for the control is the voltage amplitude. However, the DEP can also be controlled using the voltage phase shifts. Moreover, even the traveling wave dielectrophoresis can be controlled this way.

Apart from the greater flexibility in the actuation, the phase shift control itself is also advantageous when considering the hardware implementation of the driving circuits. There is no need for the voltage amplifiers. This is also reflected by the currently available laboratory equipment (see Section 6.1). The driving circuitry for the amplitude control has only eight independent channels, so arrays with more electrodes can not be utilized. On the other hand the driving circuitry for the phase control has 64 independent channels. The phase control thus allows us to experiment with arrays consisting of much more electrodes.

The derivation procedure of the model is very similar to the one seen in the previous section, where just the case of amplitude control was considered. This time, we will take into account all the three axes. Again, the basic point-dipole approximation is used. The key extension here is that the elements of the optimization variable vector $\bar{\mathbf{u}}$ are now represented by voltage phasors. These incorporate the amplitude as well as the phase of the resulting harmonic signal. The phasors can be decomposed to their real and imaginary parts and used in the subsequent calculations.

We start again by applying the principle of superposition to express the electric field potential at the given coordinates (x, y, z), this time separately for the real and the imaginary part

$$\tilde{\Phi}\left(x,y,z\right) = \Phi_{\mathrm{R}}\left(x,y,z\right) + j\Phi_{\mathrm{I}}\left(x,y,z\right), \tag{4.1}$$

$$\Phi_{\mathrm{R}}\left(x,y,z\right) = \sum_i u_{\mathrm{R}i}\Phi_{\mathrm{R}i}\left(x,y,z\right) = \bar{\mathbf{u}}_{\mathrm{R}}^T\bar{\mathbf{\Phi}}\left(x,y,z\right), \quad i = 1,2,...,n, \tag{4.2}$$

$$\Phi_{\mathrm{I}}\left(x,y,z\right) = \sum_i u_{\mathrm{I}i}\Phi_{\mathrm{I}i}\left(x,y,z\right) = \bar{\mathbf{u}}_{\mathrm{I}}^T\bar{\mathbf{\Phi}}\left(x,y,z\right), \quad i = 1,2,...,n, \tag{4.3}$$

where $u_{\mathrm{R}i}$, $u_{\mathrm{I}i}$ denote the real and imaginary part of the voltage phasor corresponding to the ith electrode (there are n electrodes in total) and $\bar{\Phi}_i\left(x,y,z\right)$ are the potentials arising from a unit voltage applied to the ith electrode while the rest of them was kept at zero potential. These potentials were again calculated numerically by solving the Laplace's equation in Comsol. The second parts of the expressions are again just the matrix-vector forms of the same. Variables denoted by bars are the vectors whose elements relate to the particular electrodes. From the known potential, it is possible to express the vector of the electric field intensity

$$\begin{aligned}\tilde{\mathbf{E}}\left(x,y,z\right) = \begin{bmatrix}\tilde{E}_x\left(x,y,z\right)\\ \tilde{E}_y\left(x,y,z\right)\\ \tilde{E}_z\left(x,y,z\right)\end{bmatrix} &= \mathbf{E}_{\mathrm{R}}\left(x,y,z\right) + j\mathbf{E}_{\mathrm{I}}\left(x,y,z\right) = \\ &= -\nabla\Phi_{\mathrm{R}}\left(x,y,z\right) - j\nabla\Phi_{\mathrm{I}}\left(x,y,z\right),\end{aligned} \tag{4.4}$$

where the individual components of the electric intensity vector can be stated again in the vector form with the explicitly expressed inputs

$$E_{\mathrm{R}a}\left(x,y,z\right) = -\bar{\mathbf{u}}_{\mathrm{R}}^{T}\frac{\partial\bar{\mathbf{\Phi}}\left(x,y,z\right)}{\partial a} = \bar{\mathbf{u}}_{\mathrm{R}}^{T}\bar{\mathbf{E}}_{a}, \quad a \in \left\{x,y,z\right\}, \tag{4.5}$$

$$E_{\mathrm{I}a}\left(x,y,z\right) = -\bar{\mathbf{u}}_{\mathrm{I}}^{T}\frac{\partial\bar{\mathbf{\Phi}}\left(x,y,z\right)}{\partial a} = \bar{\mathbf{u}}_{\mathrm{I}}^{T}\bar{\mathbf{E}}_{a}, \quad a \in \left\{x,y,z\right\}, \tag{4.6}$$

The time-averaged cDEP force component acting on the spherical homogeneous particle of the radius of r is given by [3]

$$\mathbf{F}_{\mathrm{cDEP}}\left(x,y,z\right) = \begin{bmatrix} F_{\mathrm{cDEP},x}\left(x,y,z\right) \\ F_{\mathrm{cDEP},y}\left(x,y,z\right) \\ F_{\mathrm{cDEP},z}\left(x,y,z\right) \end{bmatrix} = k_1\nabla\left(\tilde{\mathbf{E}}\cdot\tilde{\mathbf{E}}^{*}\right) = k_1\nabla\left|\tilde{\mathbf{E}}\right|^{2} \tag{4.7}$$

where k_1 is defined the same way as k in the previous derivation, $(\cdot)^{*}$ denotes the complex conjugate and $|\tilde{\mathbf{E}}|^2 = |\mathcal{R}[\tilde{\mathbf{E}}]|^2 + |\mathcal{I}[\tilde{\mathbf{E}}]|^2$. The force can be thus rewritten as

$$\mathbf{F}_{\mathrm{cDEP}}\left(x,y,z\right) = k_1\nabla(|\underbrace{\mathcal{R}[\tilde{\mathbf{E}}]}_{\mathbf{E}_{\mathrm{R}}}|^2 + |\underbrace{\mathcal{I}[\tilde{\mathbf{E}}]}_{\mathbf{E}_{\mathrm{I}}}|^2), \tag{4.8}$$

and by differentiation we get

$$\begin{aligned} F_{\mathrm{cDEP},a}\left(x,y,z\right) &= k_1\left(\frac{\partial\mathbf{E}_{\mathrm{R}}^{2}}{\partial a} + \frac{\partial\mathbf{E}_{\mathrm{I}}^{2}}{\partial a}\right) = \\ &= k_1\left(\frac{\partial}{\partial a}\left(E_{\mathrm{R}x}^{2} + E_{\mathrm{R}y}^{2} + E_{\mathrm{R}z}^{2}\right) + \frac{\partial}{\partial a}\left(E_{\mathrm{I}x}^{2} + E_{\mathrm{I}y}^{2} + E_{\mathrm{I}z}^{2}\right)\right) = \\ &= 2k_1\begin{pmatrix} E_{\mathrm{R}x}\frac{\partial E_{\mathrm{R}x}}{\partial a} + E_{\mathrm{R}y}\frac{\partial E_{\mathrm{R}y}}{\partial a} + E_{\mathrm{R}z}\frac{\partial E_{\mathrm{R}z}}{\partial a} + \\ +E_{\mathrm{I}x}\frac{\partial E_{\mathrm{I}x}}{\partial a} + E_{\mathrm{I}y}\frac{\partial E_{\mathrm{I}y}}{\partial a} + E_{\mathrm{I}z}\frac{\partial E_{\mathrm{I}z}}{\partial a} \end{pmatrix}, \quad a = \left\{x,y,z\right\}. \end{aligned} \tag{4.9}$$

Next, a symbol Ψ_{ab} defined by Eq. (3.8) is again used the force expression above is possible to get in the vector form

$$\begin{aligned} F_{\mathrm{cDEP},a} =& 2k\begin{pmatrix} \bar{\mathbf{u}}_{\mathrm{R}}^{T}\bar{\mathbf{E}}_{x}\bar{\mathbf{u}}_{\mathrm{R}}^{T}\bar{\mathbf{\Psi}}_{xa} + \bar{\mathbf{u}}_{\mathrm{R}}^{T}\bar{\mathbf{E}}_{y}\bar{\mathbf{u}}_{\mathrm{R}}^{T}\bar{\mathbf{\Psi}}_{ya} + \bar{\mathbf{u}}_{\mathrm{R}}^{T}\bar{\mathbf{E}}_{z}\bar{\mathbf{u}}_{\mathrm{R}}^{T}\bar{\mathbf{\Psi}}_{za} + \\ +\bar{\mathbf{u}}_{\mathrm{I}}^{T}\bar{\mathbf{E}}_{x}\bar{\mathbf{u}}_{\mathrm{I}}^{T}\bar{\mathbf{\Psi}}_{xa} + \bar{\mathbf{u}}_{\mathrm{I}}^{T}\bar{\mathbf{E}}_{y}\bar{\mathbf{u}}_{\mathrm{I}}^{T}\bar{\mathbf{\Psi}}_{ya} + \bar{\mathbf{u}}_{\mathrm{I}}^{T}\bar{\mathbf{E}}_{z}\bar{\mathbf{u}}_{\mathrm{I}}^{T}\bar{\mathbf{\Psi}}_{za} \end{pmatrix}, \\ & a \in \left\{x,y,z\right\}. \end{aligned} \tag{4.10}$$

Utilizing once again the fact that the transposition of a scalar does not make any change, it is possible to factor out the vectors $\bar{\mathbf{u}}_{\mathrm{R}}$,$\bar{\mathbf{u}}_{\mathrm{I}}$,$\bar{\mathbf{u}}_{\mathrm{R}}^{T}$ and $\bar{\mathbf{u}}_{\mathrm{I}}^{T}$ and to express the force components as the quadratic forms

$$\begin{aligned} F_{\mathrm{cDEP},a} =& \bar{\mathbf{u}}_{\mathrm{R}}^{T}\underbrace{2k_1\left(\sum_{b=\{x,y,z\}}\bar{\mathbf{E}}_{b}\bar{\mathbf{\Psi}}_{ab}^{T}\right)}_{\mathbf{P}_{\mathrm{cDEP},a,1,1}}\bar{\mathbf{u}}_{\mathrm{R}} + \bar{\mathbf{u}}_{\mathrm{I}}^{T}\underbrace{2k_1\left(\sum_{b=\{x,y,z\}}\bar{\mathbf{E}}_{b}\bar{\mathbf{\Psi}}_{ab}^{T}\right)}_{\mathbf{P}_{\mathrm{cDEP},a,2,2}}\bar{\mathbf{u}}_{\mathrm{I},} \\ & a \in \left\{x,y,z\right\}. \end{aligned} \tag{4.11}$$

The purpose of the numerical indexes of the $\mathbf{P}$ matrices will become clear later in this section. Next, we express the traveling wave component of the time-averaged DEP force. From [3] we have

$$\mathbf{F}_{\mathrm{twDEP}}\left(x,y,z\right)=\begin{bmatrix}F_{\mathrm{twDEP},x}\left(x,y,z\right)\\F_{\mathrm{twDEP},y}\left(x,y,z\right)\\F_{\mathrm{twDEP},z}\left(x,y,z\right)\end{bmatrix}=k_2\left(\nabla\times\left(\mathcal{R}[\tilde{\mathbf{E}}]\times\mathcal{I}[\tilde{\mathbf{E}}]\right)\right)= \\ =k_2\left(\nabla\times\left(\mathbf{E}_{\mathrm{R}}\times\mathbf{E}_{\mathrm{I}}\right)\right), \tag{4.12}$$

where k_2 is again a real constant dependent on the voltage frequency and the material properties of both the particle and the medium, this time equal to

$$k_2=2\pi\varepsilon_{\mathrm{m}}r^3\mathcal{I}\left[\frac{\varepsilon_{\mathrm{p}}^*-\varepsilon_{\mathrm{m}}^*}{\varepsilon_{\mathrm{p}}^*+2\varepsilon_{\mathrm{m}}^*}\right]. \tag{4.13}$$

By performing the vector cross product and applying the curl operator, we get the expression

$$\mathbf{F}_{\mathrm{twDEP}}\left(x,y,z\right)=k_2\begin{bmatrix}\frac{\partial\left(E_{\mathrm{R}x}E_{\mathrm{I}y}-E_{\mathrm{R}y}E_{\mathrm{I}x}\right)}{\partial y}-\frac{\partial\left(E_{\mathrm{R}z}E_{\mathrm{I}x}-E_{\mathrm{R}x}E_{\mathrm{I}z}\right)}{\partial z}\\\frac{\partial\left(E_{\mathrm{R}y}E_{\mathrm{I}z}-E_{\mathrm{R}z}E_{\mathrm{I}y}\right)}{\partial z}-\frac{\partial\left(E_{\mathrm{R}x}E_{\mathrm{I}y}-E_{\mathrm{R}y}E_{\mathrm{I}x}\right)}{\partial x}\\\frac{\partial\left(E_{\mathrm{R}z}E_{\mathrm{I}x}-E_{\mathrm{R}x}E_{\mathrm{I}z}\right)}{\partial x}-\frac{\partial\left(E_{\mathrm{R}y}E_{\mathrm{I}z}-E_{\mathrm{R}z}E_{\mathrm{I}y}\right)}{\partial y}\end{bmatrix}. \tag{4.14}$$

Next, we proceed with the differentiation and we get this simple expression for each force component

$$F_{\mathrm{twDEP},a}\left(x,y,z\right)=k_2\left(E_{\mathrm{R}a}\frac{\partial E_{\mathrm{I}b}}{\partial b}+E_{\mathrm{I}b}\frac{\partial E_{\mathrm{R}a}}{\partial b}-E_{\mathrm{R}b}\frac{\partial E_{\mathrm{I}a}}{\partial b}-E_{\mathrm{I}a}\frac{\partial E_{\mathrm{R}b}}{\partial b}\right), \\ a\in\left\{x,y,z\right\},b\in\left\{x,y,z\right\}\backslash a. \tag{4.15}$$

By its conversion to a vector form we have

$$F_{\mathrm{twDEP},a}\left(x,y,z\right)=k_2\begin{pmatrix}\bar{\mathbf{u}}_{\mathrm{R}}^T\bar{\mathbf{E}}_a\bar{\mathbf{u}}_{\mathrm{I}}^T\bar{\boldsymbol{\Psi}}_{bb}+\bar{\mathbf{u}}_{\mathrm{R}}^T\bar{\boldsymbol{\Psi}}_{ab}\bar{\mathbf{u}}_{\mathrm{I}}^T\bar{\mathbf{E}}_b-\\-\bar{\mathbf{u}}_{\mathrm{R}}^T\bar{\mathbf{E}}_b\bar{\mathbf{u}}_{\mathrm{I}}^T\bar{\boldsymbol{\Psi}}_{ab}-\bar{\mathbf{u}}_{\mathrm{R}}^T\bar{\boldsymbol{\Psi}}_{bb}\bar{\mathbf{u}}_{\mathrm{I}}^T\bar{\mathbf{E}}_a\end{pmatrix}, \\ a\in\left\{x,y,z\right\},b\in\left\{x,y,z\right\}\backslash a. \tag{4.16}$$

Now we apply again the transpositions where suitable and factor out the vectors $\bar{\mathbf{u}}_{\mathrm{I}}$ and $\bar{\mathbf{u}}_{\mathrm{R}}^T$. This yields the force components again as the quadratic forms

$$F_{\mathrm{twDEP},a}=\bar{\mathbf{u}}_{\mathrm{R}}^T\underbrace{k_2\left[\sum_{b\in\{x,y,z\}\backslash a}\begin{pmatrix}\bar{\mathbf{E}}_a\bar{\boldsymbol{\Psi}}_{bb}^T+\bar{\boldsymbol{\Psi}}_{ab}\bar{\mathbf{E}}_b^T-\\-\bar{\mathbf{E}}_b\bar{\boldsymbol{\Psi}}_{ab}^T-\bar{\boldsymbol{\Psi}}_{bb}\bar{\mathbf{E}}_a^T\end{pmatrix}\right]}_{P_{\mathrm{twDEP},a,1,2}}\bar{\mathbf{u}}_{\mathrm{I}},\quad a\in\left\{x,y,z\right\}. \tag{4.17}$$

Now we have all the necessary force components and they can be joined together into a single expression suitable for the optimization task

$$F_{\mathrm{DEP},a}\left(x,y,z\right)=\mathbf{F}_{\mathrm{cDEP},a}\left(x,y,z\right)+\mathbf{F}_{\mathrm{twDEP},a}\left(x,y,z\right)= \\ =\bar{\mathbf{u}}_{\mathrm{R}}^T\mathbf{P}_{\mathrm{cDEP},a,1,1}\bar{\mathbf{u}}_{\mathrm{R}}+\bar{\mathbf{u}}_{\mathrm{I}}^T\mathbf{P}_{\mathrm{cDEP},a,2,2}\bar{\mathbf{u}}_{\mathrm{I}}+\bar{\mathbf{u}}_{\mathrm{R}}^T\mathbf{P}_{\mathrm{twDEP},a,1,2}\bar{\mathbf{u}}_{\mathrm{I}}= \\ =\underbrace{\begin{bmatrix}\bar{\mathbf{u}}_{\mathrm{R}}^T & \bar{\mathbf{u}}_{\mathrm{I}}^T\end{bmatrix}}_{\bar{\mathbf{u}}'^T}\underbrace{\begin{bmatrix}\mathbf{P}_{\mathrm{cDEP},a,1,1} & \mathbf{P}_{\mathrm{twDEP},a,1,2}\\0 & \mathbf{P}_{\mathrm{cDEP},a,2,2}\end{bmatrix}}_{\mathbf{P}_a}\underbrace{\begin{bmatrix}\bar{\mathbf{u}}_{\mathrm{R}}\\\bar{\mathbf{u}}_{\mathrm{I}}\end{bmatrix}}_{\bar{\mathbf{u}}'},\quad a\in\left\{x,y,z\right\}. \tag{4.18}$$

As promised, this expression is fairly universal and can be used for both the voltage amplitude and the phase shift optimization, separately or even together. Moreover, it is possible to decide whether to incorporate the twDEP force in the model or not.

Unfortunately, we are currently unable to induce the twDEP experimentally. Although the imaginary part of the Clausius–Mossotti factor, which influences the twDEP force magnitude (see Eqs. (4.12) and (4.13)) and is a basic precondition for the twDEP observation should be theoretically high enough at a suitable frequency range of the voltage (around 40 kHz), the twDEP was never experienced. By using a much higher frequency (in our case 300 kHz) corresponding to an almost zero values of the imaginary part of the Clausius–Mossotti factor, we may consider the twDEP with a sufficient certainty as being negligible. The individual optimization cases will be detailed in the following overview:

- **optimization only over the voltage amplitudes**
  by only the voltage amplitude modulation it is not possible to induce the twDEP. This is also apparent from the derived expression. Let us assume that all the sinusoidal voltage signals are in this situation in phase (this is in our case guaranteed by the driving circuitry described later in Section 6.1). Therefore the term $\bar{\mathbf{u}}_\mathrm{I}$ will be kept zero and the amplitude will be changing only through $\bar{\mathbf{u}}_\mathrm{R}$. Thus the expression reduces to $\mathbf{F}_a = \bar{\mathbf{u}}_\mathrm{R}^T \mathbf{P}_{\mathrm{cDEP},a,1,1} \bar{\mathbf{u}}_\mathrm{R}$. The optimization task itself can then be formulated for example like (using $\bar{\mathbf{u}}$ instead of $\bar{\mathbf{u}}_\mathrm{R}$ for simplicity)

$$\begin{aligned} \bar{\mathbf{u}}^\mathrm{opt} &= \arg\min_{\bar{\mathbf{u}}} \left[\begin{array}{l} \left(\sum\limits_{a\in\{x,y\}} \left| \bar{\mathbf{u}}^T \mathbf{P}_{\mathrm{cDEP},a,1,1}(x,y,z)\, \bar{\mathbf{u}} - F_a^\mathrm{des} \right| \right) + \\ + \left| \bar{\mathbf{u}}^T \mathbf{P}_{\mathrm{cDEP},z,1,1}(x,y,z)\, \bar{\mathbf{u}} + F_\mathrm{sed} - F_z^\mathrm{des} \right| \end{array} \right], \\ &\text{s.t.}\;\; |u_i| \le U_\mathrm{max}, \end{aligned} \tag{4.19}$$

  where $\bar{\mathbf{u}}$ denotes here the amplitude of applied voltage, F_x^des, F_y^des and F_z^des are the appropriate components of the desired force, F_sed is the sedimentation force acting on the particle and U_max is the maximal voltage amplitude allowable.
- **optimization only over the phases**
  by modulating the phase shifts of the voltage signals, both the cDEP and the twDEP forces may arise. The formulation of the optimization criterion is more delicate this time. In contrast with the constant phase constraint, the constant amplitude constraint is not so easy achievable. Thus the optimization task has the following form

$$\begin{aligned} \bar{\mathbf{u}}^\mathrm{opt} &= \arg\min_{\bar{\mathbf{u}}} \left[\begin{array}{l} \left(\sum\limits_{a\in\{x,y\}} \left| \bar{\mathbf{u}}^T \mathbf{P}_a(x,y,z)\, \bar{\mathbf{u}} - F_a^\mathrm{des} \right| \right) + \\ + \left| \bar{\mathbf{u}}^T \mathbf{P}_z(x,y,z)\, \bar{\mathbf{u}} + F_\mathrm{sed} - F_z^\mathrm{des} \right| \end{array} \right], \\ &\text{s.t.}\;\; \left| u_i^2 + u_{n+i}^2 \right| = U_\mathrm{max}^2, \end{aligned} \tag{4.20}$$

  where $\bar{\mathbf{u}}$ is now a vector defined the same way as $\bar{\mathbf{u}}'$ in Eq. (4.18) and $\mathbf{P}_x$, $\mathbf{P}_y$ and $\mathbf{P}_z$ are matrices of the form $\begin{bmatrix} \mathbf{P}_{\mathrm{cDEP},a,1,1} & \mathbf{P}_{\mathrm{twDEP},a,1,2} \\ 0 & \mathbf{P}_{\mathrm{cDEP},a,2,2} \end{bmatrix}$ if there is interest also in the twDEP and $\begin{bmatrix} \mathbf{P}_{\mathrm{cDEP},a,1,1} & 0 \\ 0 & \mathbf{P}_{\mathrm{cDEP},a,2,2} \end{bmatrix}$ if we want to ignore it in the model. This can simplify the computation and save the valuable execution time in the control loop if we know it is of no importance in the given setting.

In the practical implementation, when optimizing just over a discrete set of phases, it is possible to remove the inconvenient equality constraint under the condition that only feasible points will be evaluated.

- **optimization over both the amplitudes and the phases of the voltage signal**
  This, as the most general task, is in fact also the most straightforward one. Now there are no equality constraints regarding the voltage amplitude and thus it is possible to optimize simply over $\bar{\mathbf{u}}'$ (again denoted as $\bar{\mathbf{u}}$ for convenience). Through the real and imaginary part of the voltage phasor it is possible to generate any amplitude and phase shift. The constraints have to be added only for the amplitude limitation. An example of the optimization task definition is

$$\bar{\mathbf{u}}^{\mathrm{opt}} = \arg\min_{\bar{\mathbf{u}}} \left[\begin{array}{c} \left(\sum\limits_{a\in\{x,y\}} \left| \bar{\mathbf{u}}^T \mathbf{P}_a (x,y,z)\, \bar{\mathbf{u}} - F_a^{\mathrm{des}} \right| \right) + \\ \left| \bar{\mathbf{u}}^T \mathbf{P}_z (x,y,z)\, \bar{\mathbf{u}} + F_{\mathrm{sed}} - F_z^{\mathrm{des}} \right| \end{array} \right], \qquad (4.21)$$
$$\text{s. t. } u_i^2 + u_{n+i}^2 \le U_{\max}^2,$$

  where all the symbols are defined the same way as earlier. The resulting amplitude and the phase can then be extracted as $m_i = \sqrt{u_i^2 + u_{n+i}^2}$, respectively $\phi_i = atan\left(\frac{u_{n+i}}{u_i}\right)$ where n is the number of electrodes.

4.1 Control for the four-sector array

With the newly acquired ability to influence the DEP force not only by the voltage amplitudes but also by its phase shifts, it becomes possible to use the 64-channel generator capable of setting the phase shifts (see Section 6.1.2) as a driving circuit for the electrodes. Furthermore, a huge number of the individually controlled channels allows to drive electrode arrays with much more electrodes – particularly the so-called four-sector electrode array (see Figure 4.1).

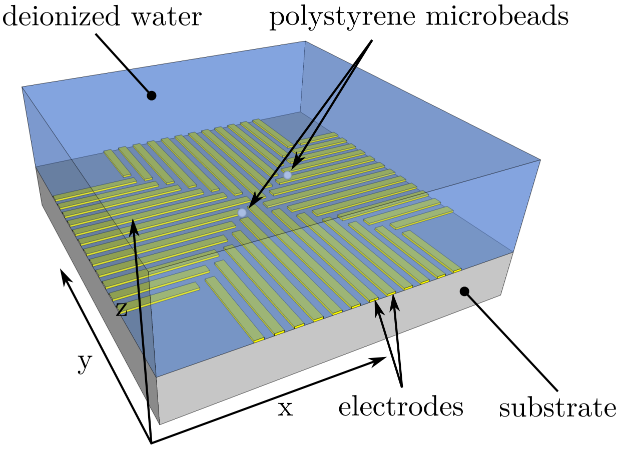

Figure 4.1. Illustration of the four-sector array manipulator.

This array consists of 48 gold electrodes fabricated again on a glass substrate. Their widths are 50 µm and their inter-electrode gaps are also of the same size. The electrodes of this array are arranged in the four identical groups (also-called sectors) of 12 electrodes rotated mutually by 90 °. This special layout was designed by Jiří Zemánek for the purpose of the 2D manipulation. A control strategy allowing for the motion in the directions perpendicular to the electrodes inside the sectors and in the directions along the interfaces of the sector was designed and successfully demonstrated [29]. The limitation of this approach is that although arbitrary location in the x and y coordinates can be reached by an object, the trajectory along which the object travels is restricted (see Figure 4.2). By deploying the optimization based control scheme described in the previous sections, this limitation will no longer be so strict.

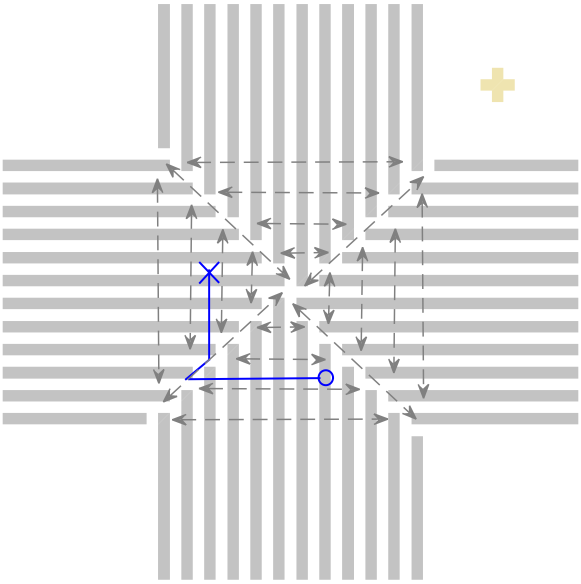

Figure 4.2. The limitations imposed on the object trajectory under the control system used so far. The gray arrows show the possible directions of the motion and the blue line is an example of the trajectory with the start denoted by the circle and ending at the cross.

A nice property of the proposed optimization based control scheme is that it can be applied (almost as it is) to an electrode array of any layout. The only thing that needs to be done is to simulate the potential distribution for the new geometry of the electrodes and to recompute the appropriate potential derivatives necessary for the DEP force calculation. The increased number of electrodes, however, brought a few technical difficulties that needed to be solved. Not only that the numerical simulations take longer time to execute (N simulations of a larger model have to be performed, where N is the number of electrodes), but also issues with the limited computer memory arose. In order to perform the numerical simulations, an adaptive meshing had to be used creating the finest mesh only where the most dramatic changes in potential are expected (in the vicinity of the single electrode to which the potential of 1 V is applied). The simulation area was then divided into a checker board like tiles and one data file for the each individual tile containing the relevant results was created. Size of the tiles was chosen such that at least nine of the associated data files could fit in the operational/random access memory (RAM) at the same time. One of the files would belong to the tile in which the particle is currently located (so the data for construction of $\mathbf{P}$ matrices would be read from it) and the remaining eight files would correspond to the directly adjacent tiles. These would be preloaded for a case when the particle leaves the currently active tile. I believed that such an algorithm taking care of loading the data that are likely to be used in a near future (and removing the other ones) would be a suitable solution. In Matlab, however, the implementation of an asynchronous file loading showed up to be at least problematic (e.g. no solution based on the parallel computing toolbox worked as expected). Because of the lack of the time a solution leaning on the direct file access from the hard disk was used in the end. Other promising approaches based e.g. on `mex` functions or on shared memory would be however interesting to investigate later.

In order to make a better notion of the movement limitations mentioned above, a few simulative experiments were conducted. A grid of 25 × 25 points at the levitation height of 130 µm covering one quarter of the array was generated. This way, I made use of the geometrical symmetry of the array. A force of the same magnitude ($50 \cdot 10^{-12}$ N) was then searched for the sixteen evenly distributed directions. The magnitudes of the actually found forces were then used to define the vertices of the polygons drawn in Figure 4.3. If the polygon resembles a circle the object in such a position can move freely in all the directions. On the other hand, the bow tie-like shape of a polygon indicates that the motion in direction perpendicular to the vertical axis of the bow tie (in the orientation it is usually worn) is hardly achievable. From the figure it is obvious that the best conditions for movement control in all the directions are at the center of the electrode array (here the lower right corner of the image) and at the boundary of the two sectors of the array (the diagonal line from the upper left to the lower right corner). However, even the worst regions of the array suggest that there exist forces other than just perpendicular to the electrodes that can be achieved and a controller could utilize this fact.

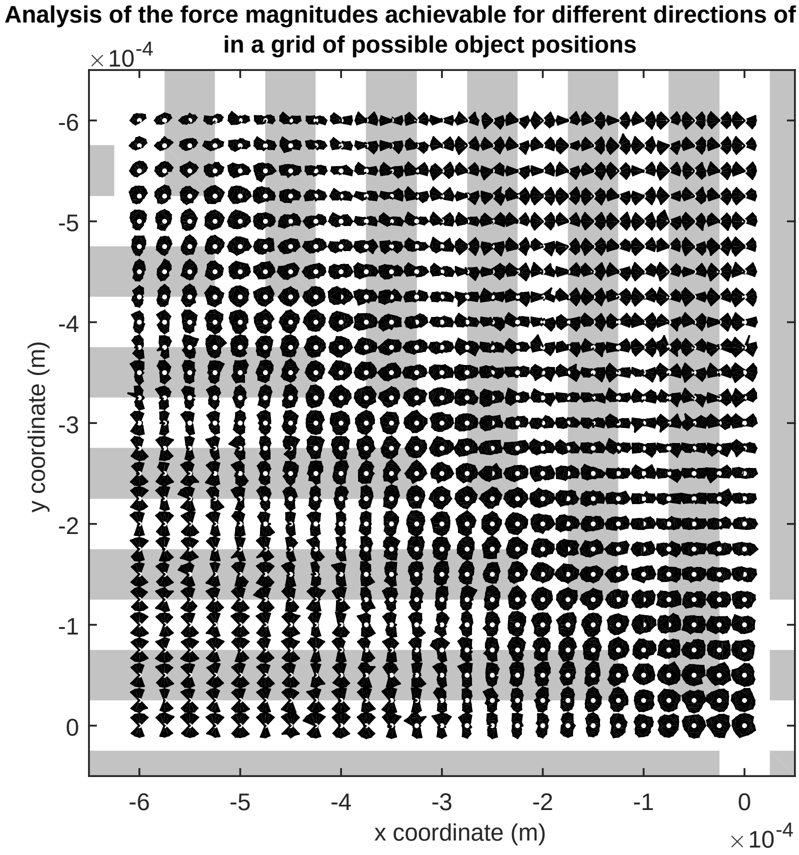

Figure 4.3. The analysis of the force magnitudes achievable in the different directions of the motion and in the grid of points (represented by the white dots).

Another simulation, whose results are presented in Figure 4.4 attempts to show, which positions are reachable by the controlled object in a given time. The initial position of the object is indicated by the white dot. This simulation was performed in an iterative way, when each iteration corresponded to one control period. At the start of the iteration there is a set of points defining the current reachability border. Next, the maximum force is found in the 16 different directions for each of the border point. The bead motion is then simulated given the corresponding control action. Finally, the iteration ends by the creation of the new reachability border based on the set union of all the starting and ending positions of the beads. This approach gives another insight into the abilities of the manipulator. It is again obvious that as soon as the object gets to the interface of the two electrode sectors, it can easily move faster and in more directions, and therefore the reachability area quickly extends.

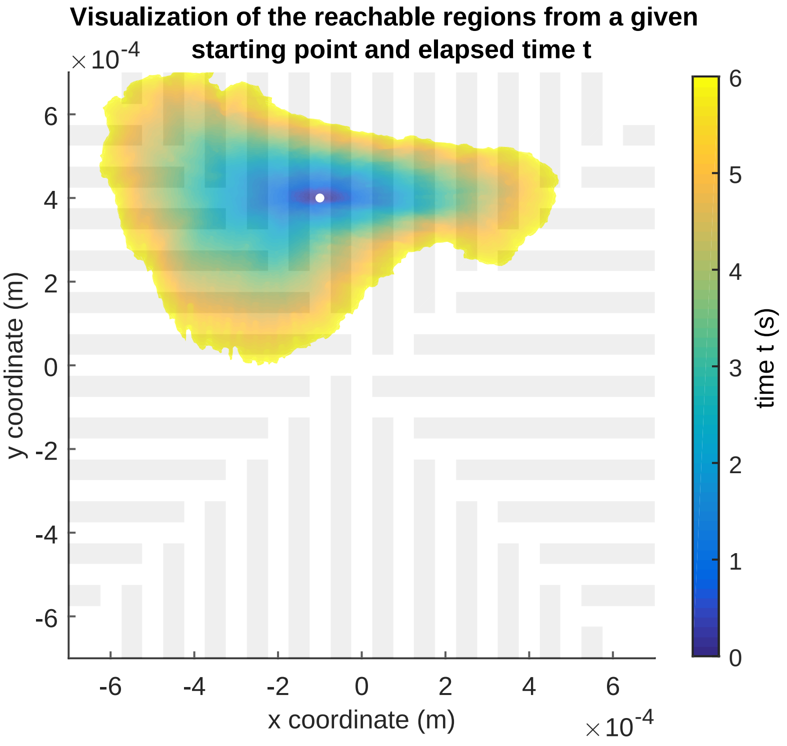

Figure 4.4. The reachable regions from one given starting point and elapsed time t.

Similarly as in the case of the parallel electrode array, the control algorithm was first tested on the SIL. The simulation again takes place in Matlab/Simulink and resembles the scheme in Figure 3.3. The only difference this time is that 48 control signals (the voltages on the electrodes) are present and the movement simulation runs over all the three space dimensions. The simulation of the reference trajectory tracking is in Figure 4.5. It should be noted that the reference signal was changing in a big steps during this simulation (as it is apparent from the graphs on the right side of the figure), so the only important points on the reference trajectory are its corners. The deviation from the dashed line on the left image showing the top view of the array was therefore not directly the objective of the minimization. Nevertheless, it still says something about the system, because with a perfectly working controller these deviations should be zero anyway. As in the case of a parallel electrode array, the levitation height of the bead (its position in the z coordinate) is again the subject of the biggest errors, especially when the bead is moving. Still, the control system is due to its inherent robustness able to track the reference signals with the maximal steady state error of 10 µm for the x coordinate and 35 µm for the y coordinate.

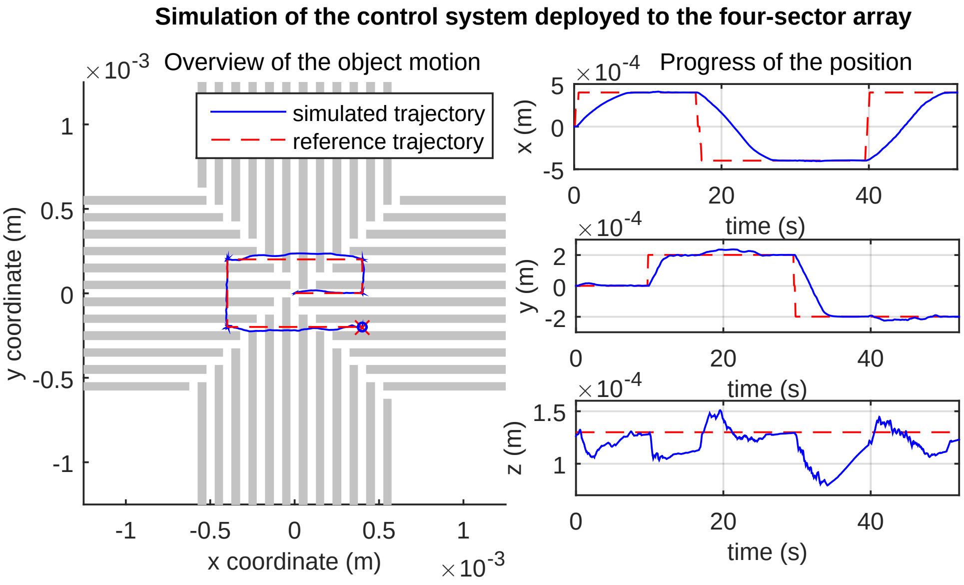

Figure 4.5. The simulation of the position reference signal tracking.

The precise trajectory tracking is shown in Figure 4.6. Here the reference path is defined by many near points located on a circle (apparent from the shown top view). Since the steps in the reference signals are small enough this time, the deviations from the trajectory are not higher than 12 µm (with the mean deviation of 2.7 µm). The problem is, however, the levitation height of the bead. The simulation shows that since this time the particle is continuously in motion, the levitation height is not being restored and the bead basically falls down until it reaches the bottom. The 2D position control still surprisingly works well, however, some problems with the particle sticking to the bottom surface of the array may arise in the practical experiments.

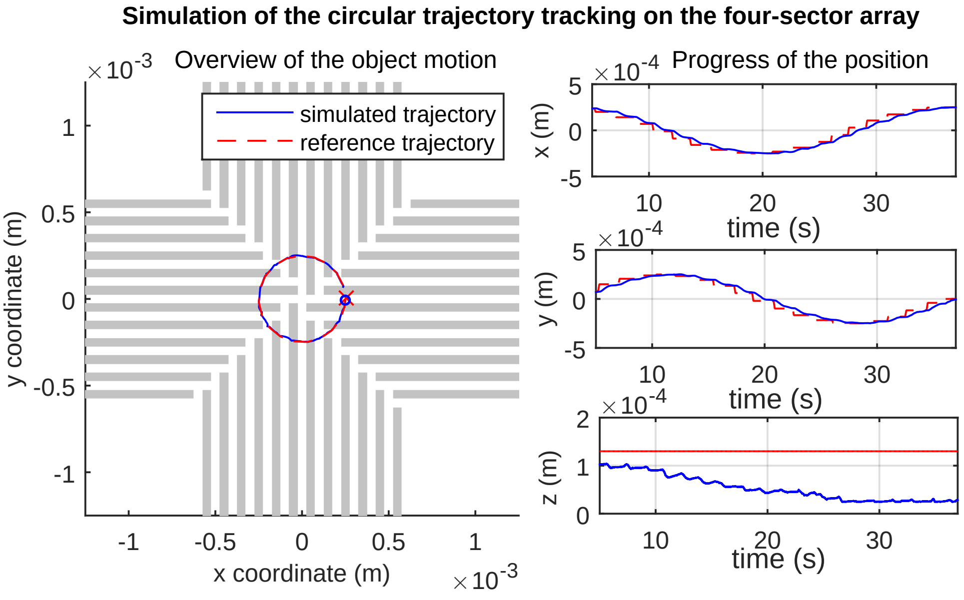

Figure 4.6. The simulation showing the results of the circular trajectory tracking.

4.2 Validity of the point-dipole approximation

Model of the DEP forces used for the control purpose in the current manipulator is based on the Eq. (2.68) from [10]. This relation is derived using many assumptions such as that the object is homogeneous and spherical, the voltages are sinusoidal and no mutual particle force interactions are considered. The most discussable one within the considered system is, however, the approximation of the particle just by the simple dipole moment. This is perfectly fine if the particle is small relatively to the inhomogeneity of the surrounding electric field so that the field does not change much within its volume. Unfortunately, this is not the case with the used 50 µm beads levitating at the height of 130 µm over the electrodes of the width of 100 µm. Yet the proposed control system using this insufficiently precise model is capable of the precise objects positioning as it will be shown in the Section 6. In order to find out how accurate the model is and how much the success is due to the feedback, the topic was investigated in a more detail.

The most correct way of calculating the DEP forces is the so-called Maxwell stress tensor method (MST) [30]. This method, described in depth in [9], does not build on any approximation or assumption and allows for a precise calculation of the DEP force acting on an arbitrarily shaped object of any dimension. Moreover, if several particles are close to each other, their mutual force interaction is also considered by the method. All of this can be achieved only by first numerically solving the electric field in the presence of the objects (at their respective positions). This has to be done for their every new constellation. The numerical computation is usually done using the FEM or an arbitrary Lagrangian-Eulerian (ALE) method. Since it takes long computational times, it is not suitable for the control purposes.

Nevertheless, the MST can serve as a reference solution for a comparing with the approximate solutions used. Rosales and Lim performed a study [30], in which they did exactly this. Solution obtained by MST for a single particle in the DEP trap made by eight circular electrodes was compared with the equivalent multipolar approaches. Spherical particles of different sizes at different positions relatively to the center of the DEP trap were used. It showed up that for small particles (with respect to the size of the electrodes), multipoles of the order higher than two (quadrupoles) or three (octopoles) are not necessary in the most cases since they do not improve the accuracy significantly. In all the studied cases the error was below 5 % compared to the MST method. For particles of greater sizes (with the considerable size in comparison with the trap) the need for higher order multipolar terms however arose. The authors suggest that the dipolar approximation should be used only for the rough estimates of the DEP force and that a special attention should be paid in the following situations:

- the bead is near the electrodes,
- the bead is relatively big compared to the electrodes,
- the bead is near the field null (a place where the electric intensity magnitude is zero and the dipolar approximation predicts zero force).

This topic is so important within this work, since the mathematical model is the basis of the used control and thus should be justified.

4.3 Using quadrupoles

An appropriate compromise between the computational demands and the model accuracy may be the second order approximation – quadrupoles.

The respective force expressions for the higher order approximations may be found in [31] and especially in [9], where both the cDEP and the twDEP are considered and the derivation of these expressions from the MST theory is present. The resulting time-averaged expressions translated into the used notation are

$$
\begin{aligned}
F_{\mathrm{DEP}} = & 2\pi\varepsilon_{\mathrm{m}} r^3 \left[\begin{array}{l} \mathcal{R}\left[\frac{\varepsilon_{\mathrm{p}}^* - \varepsilon_{\mathrm{m}}^*}{\varepsilon_{\mathrm{p}}^* + 2\varepsilon_{\mathrm{m}}^*}\right] \left(\sum\limits_{a \in \{x,y,z\}} E_{\mathrm{R}a} \nabla E_{\mathrm{R}a} + E_{\mathrm{I}a} \nabla E_{\mathrm{I}a} \right) - \\ -\mathcal{I}\left[\frac{\varepsilon_{\mathrm{p}}^* - \varepsilon_{\mathrm{m}}^*}{\varepsilon_{\mathrm{p}}^* + 2\varepsilon_{\mathrm{m}}^*}\right] \left(\sum\limits_{a \in \{x,y,z\}} E_{\mathrm{I}a} \nabla E_{\mathrm{R}a} + E_{\mathrm{R}a} \nabla E_{\mathrm{I}a} \right) \end{array} \right] + \qquad (4.22) \\
& + \frac{2\pi\varepsilon_{\mathrm{m}} r^5}{3} \left[\begin{array}{l} \mathcal{R}\left[\frac{\varepsilon_{\mathrm{p}}^* - \varepsilon_{\mathrm{m}}^*}{2\varepsilon_{\mathrm{p}}^* + 3\varepsilon_{\mathrm{m}}^*}\right] \left(\sum\limits_{a \in \{x,y,z\}} \sum\limits_{b \in \{x,y,z\}} \frac{\partial E_{\mathrm{R}a}}{\partial b} \nabla \frac{\partial E_{\mathrm{R}a}}{\partial b} + \frac{\partial E_{\mathrm{I}a}}{\partial b} \nabla \frac{\partial E_{\mathrm{I}a}}{\partial b} \right) + \\ +\mathcal{I}\left[\frac{\varepsilon_{\mathrm{p}}^* - \varepsilon_{\mathrm{m}}^*}{2\varepsilon_{\mathrm{p}}^* + 3\varepsilon_{\mathrm{m}}^*}\right] \left(\sum\limits_{a \in \{x,y,z\}} \sum\limits_{b \in \{x,y,z\}} \frac{\partial E_{\mathrm{I}a}}{\partial b} \nabla \frac{\partial E_{\mathrm{R}a}}{\partial b} - \frac{\partial E_{\mathrm{R}a}}{\partial b} \nabla \frac{\partial E_{\mathrm{I}a}}{\partial b} \right) \end{array} \right].
\end{aligned}
$$

It can be shown that the first summand in the above expression is exactly the point-dipole approximation used so far. The only aids that need to be used are the identity $\frac{\partial E_a}{\partial b} = \frac{\partial E_b}{\partial a}$, which follows from the fact that electric field is irrotational (it holds $\nabla \times \mathbf{E} = 0$) and furthermore that the electric potential meets the Laplace equation $\Delta\phi = 0$. For the sake of brevity, this treatment will not be shown here nor the reformulation of the expressions into the quadratic forms. The steps are in this case very similar to the derivations shown before. However, note that the expression contains not only the first and second derivatives of the electric potential, but also the third derivatives of the potential. More data has to be therefore computed in advance. Furthermore, accessing these data during the control period can have non-negligible performance consequences.

A set of the simulations was conducted in order to find out how much the force calculated using the quadrupole approximation differs from the one acquired using the so far used point-dipole approximation. In total, 1×10^5 random voltage sets were generated and a force at the center of the array and levitation height of 130 µm was calculated using the both methods. Histogram of the percentage difference (or the error if the force from quadrupole approximation is used as the reference value) is shown in Figure 4.7. It is apparent that although in some situations the errors might be quite significant, in the most of the cases they do not exceed 10 % for the horizontal force and around 3 % for the vertical force. Using the point-dipole approximation is therefore a reasonable compromise between the accuracy and the computational demands.

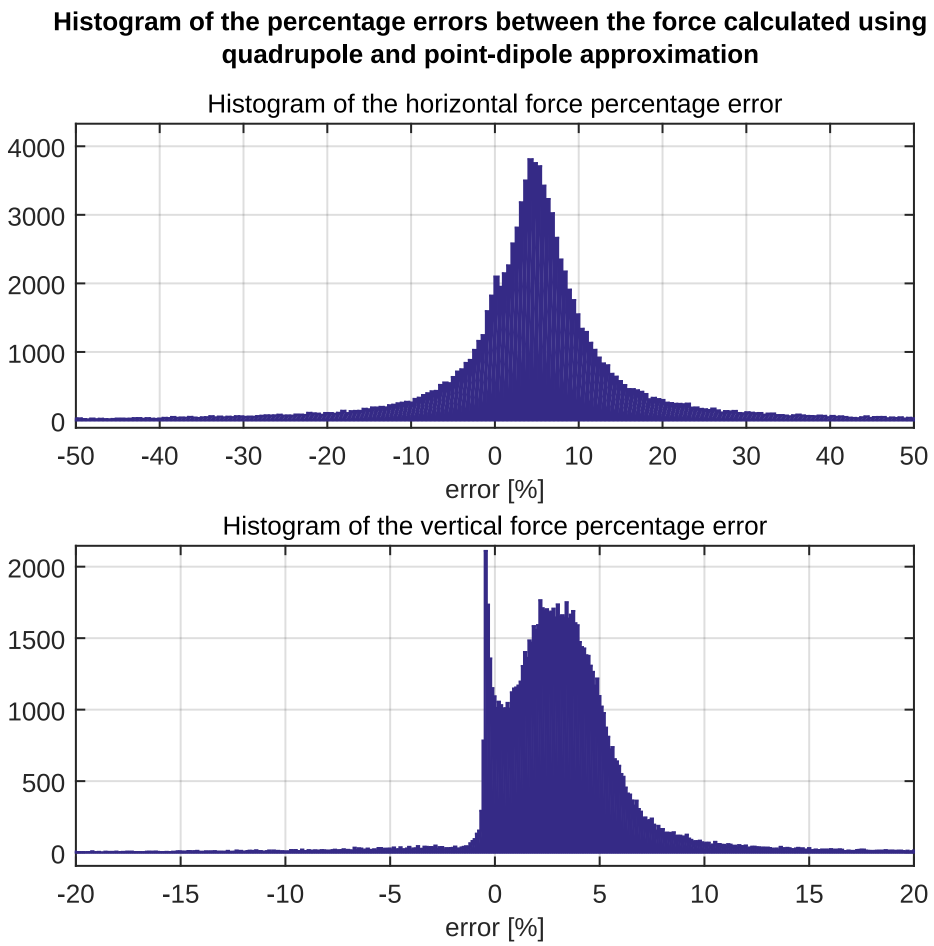

Figure 4.7. The histograms of the errors between the first order (point-dipole) and the second order (quadrupole) approximation of the DEP force based on the sample of 1×10^5 simulations with the random voltage inputs.

Chapter 5

Optimization solvers

Global optimization problems are generally very difficult to solve. Analytical methods are usually not applicable and the common optimization solvers are prone to get stuck in a local minimum. Therefore they have to be either provided with a good initial guess of the solution or started repeatedly from many random initial conditions. This approach together with other randomized strategies, however, do not guarantee to find the solution. Moreover, the aggravating fact in this case is that the solution has to be found in a very limited time (orders of milliseconds), so that a reasonable control period can be achieved. Thus it can be very helpful to analyze the given problem well and utilize as much as possible of its specific properties.

5.1 Optimization task analysis

The optimization task of finding the set of inputs $\bar{\mathbf{u}}$ (the voltage amplitudes, the phase shifts or both at the same time) establishing the required forces at the given positions can be stated basically in the two possible ways.

The first one is given by Eq. (4.21). The reffered optimization criterion contains the absolute value of the difference between the required and the actually generated force. The absolute value is necessary here, because otherwise the negative infinity (corresponding to the infinite error) would be the sought minimizer. The constraints are then used only to restrict the control variables $\bar{\mathbf{u}}$ to a given range.

The second, equivalent approach, is to define an error vector $\mathbf{e}$, which would consist of the same difference used in the criterion described above

$$e_a = F_a^{\text{des}} - \bar{\mathbf{u}}^T \mathbf{P}_a \bar{\mathbf{u}} - F_{\text{sed},a}, \quad a \in \{x, y, z\} . \tag{5.1}$$

Using this definition, the optimization criterion can be stated in the following way

$$\begin{aligned} &\min_{\bar{\mathbf{u}}} \|\mathbf{e}\| + \alpha \|\bar{\mathbf{u}}\| \\ &\text{s. t.} \; F_a^{\text{des}} - \bar{\mathbf{u}}^T P_a \bar{\mathbf{u}} - F_{\text{sed},a} - e_a = 0, \quad a \in \{x, y, z\} , \\ &\qquad\qquad u_i^2 + u_{n+i}^2 \leq U_{\max}^2, \end{aligned} \tag{5.2}$$

where all the symbols are defined the same way as in the previous sections and α is used to only set the trade-off between the error reduction and the control effort used. The type of the used norm is not firmly determined (it may be 2-norm, 1-norm, ...).

The stated formulation of the objective function is the only one of the many other possible. The error in the force may be for example expressed not only as the set of deviations corresponding to the individual force components, but also as the error in its magnitude and its direction. It is then possible to introduce some weights for these individual errors so that the optimization prefers for example the lower error in the direction over the error in the magnitude. This particular choice showed advantageous for our application.

Furthermore, the expression defining the amount of the control effort can be stated differently. The one mentioned may penalize for example a shifted solution $\bar{\mathbf{u}} + [s_{\mathrm{R}}, s_{\mathrm{R}}, ..., s_{\mathrm{R}}, s_{\mathrm{I}}, s_{\mathrm{I}}, ..., s_{\mathrm{I}}]^T$, $s_{\mathrm{R}}, s_{\mathrm{I}} \in \mathbb{R}$ if its norm is smaller, over the original $\bar{\mathbf{u}}$, although both of them have exactly the same effect. The values of s_{R} and s_{I} represent the real, respectively the imaginary part of an arbitrary potential phasor $\tilde{s}$. The only thing that has an impact on the generated force is namely the difference between the voltage phasors corresponding to the individual electrodes. This can be also imagined as one electrode being referential and defining the zero potential for the others. Utilizing this, the optimization problem can possibly be reduced by the two dimensions in the case of the optimization over both the amplitudes and the phases or by one dimension in the case of the optimization over just the amplitudes or the phases. As an example regarding the case of the amplitudes optimization, the control variables (the voltage amplitudes) can be transformed the following way

$$\bar{\mathbf{d}} = \begin{bmatrix} -1 & 0 & \cdots & 0 \\ 1 & -1 & \ddots & \vdots \\ 0 & 1 & \ddots & 0 \\ \vdots & \ddots & \ddots & -1 \\ 0 & \cdots & 0 & 1 \end{bmatrix}^T \bar{\mathbf{u}}. \tag{5.3}$$

This approach will be used later in the following section.

An important fact related to the both problem definitions is that the $\mathbf{P}$ matrices defining the quadratic forms are indefinite, thus creating sort of saddle points. Furthermore, it is known ahead that the objective function will never be negative. Therefore if a solution with a zero objective function is found, it must lie in the set of the global minimum points. The difficulty of the problem lies in the fact, that it is nonconvex in both of the described definitions (4.21) and (5.2). Indeed, in the former case the absolute value operator applied to the shifted quadratic form results in the nonconvex function. Similarly, the quadratic equality-type constraints by themselves define the nonconvex set in the latter case.

5.2 Numerical solvers

In the following paragraphs, I will describe the optimization approaches that were tried and evaluate their performance. As a benchmark will serve the problem of the voltage amplitudes optimization on the eight electrodes of the parallel array. A horizontal force of the magnitude of 50×10^{-12} N for one bead located at the center of the array in the typical levitation height of 130 µm will be searched for.

First, a simple approach using the **interior-point algorithm** (IP) of the `fmincon` Matlab function was used. As the objective function a quadratic form $\bar{\mathbf{d}}^T\bar{\mathbf{d}}$ with $\bar{\mathbf{d}}$ defined in Eq. (5.3) was used and the requirements for the forces ($F_a^{\mathrm{des}} - \bar{\mathbf{u}}^T\mathbf{P}_a\bar{\mathbf{u}} - F_{\mathrm{sed},a} = 0$) were used as the constraints. Additionally, the upper and lower element-wise bounds on $\bar{\mathbf{u}}$ were incorporated. Although no special starting point is chosen (just a random vector), the benchmark test was always successfully solved with the average run time of 0.0386 s (measured on a notebook equipped with Intel i5 (2.27 GHz), 8 GB RAM and 64-bit Windows 7). This time, however, can be reduced only slightly by adjusting the iteration count limits and at the great expense of the precision degradation. Furthermore, when adding more constraints on the forces, only the local minimum is found most of the times and a need for repeated starts with the random initial guesses arises (`MultiStart` command).

In the next attempt, the same solver was used and just the objective and constraint functions changed so that the optimization ran only over the **control variable differences** ($\bar{\mathbf{d}} = [u_2 - u_1, u_3 - u_2, ...u_N - u_{N-1}]^T$. This was achieved by using the following transformation relationship (the first element of $\bar{\mathbf{u}}$ will be without the loss of generality equal always to zero)

$$\bar{\mathbf{u}} = \begin{bmatrix} 0 & 0 & \cdots & 0 \\ 1 & 0 & \ddots & \vdots \\ 1 & 1 & \ddots & 0 \\ \vdots & \ddots & \ddots & 0 \\ 1 & \cdots & 1 & 1 \end{bmatrix} \bar{\mathbf{d}}. \tag{5.4}$$

Furthermore, we can restrict ourselves just to the vectors $\bar{\mathbf{d}}$, whose first element is positive (since the vectors $\bar{\mathbf{d}}$ and $-\bar{\mathbf{d}}$ generate the same force field).

In a similar way, the upper and the lower element-wise bounds imposed in the optimization task definition for the IP were transformed to a set of linear inequalities. Hereby, both the execution time and the solution errors were slightly reduced (the time to 25.3 ms). For the case of more particles the situation gets surprisingly even worse than in the previous case.

Next, also the variant having the **force requirements directly in the optimization criterion** was tried. Both the `fmincon` and the `fminsearchcon` [32] (which is a modificaton of the classical `fminsearch`) were used this time. The latter one uses a derivative free method (which is generally believed to be slower than supplying the derivatives), but on the other hand it can be compiled into the `mex` function and therefore it is faster in the end. Better proved to be the latter algorithm with the run time of 2.4448×10^{-4} s. Though its error in the force magnitude is around 4 %.

Another, tested tool is the specialized Matlab-based solver for the global optimization over polynomials called **Gloptipoly**¹)**.** Using it, the problem can be defined in the spirit of (5.2). A slight difference though is in the way of measuring the error size and imposing the constraints. Since Gloptipoly expects just polynomials, the absolute value has to be replaced by a power of two. Thus the error is measured as e_a^2 and the constraints look like $\bar{\mathbf{u}}^T\bar{\mathbf{u}} \leq U_{\max}^2$. To avoid the problems arising in the situations when the achievable error is zero and there is the continuous set of solutions, the regularization term $\alpha\bar{\mathbf{u}}^T\bar{\mathbf{u}}$ has to be present. Although this tool seemed promising at first, the experiments showed the opposite. Apart from the toy examples (just a few electrodes, constraints, etc.) the solution could not be found. Additionally the run time (above one second) needed by the solver to search for the solutions would prohibit its use the in real-time control.

As a next tool the so-called **Gröebner basis** was tried. It is one of the fundamental practical tools for solving the systems of polynomial equations. A Matlab implementation `groebner`²) was acquired from Matlab File Exchange (FEX) service and deployed to the problem at hand. Similarly as in the case of Gloptipoly, the only problems that were possible to solve were the simplest possible ones. With a realistic number of optimization variables and force constraints, the solver could not return any solution even if it existed. Moreover, this tool is in fact not an optimization solver since it searches only for the actual solutions.

A method based on the problem **conversion into an approximate linear program** (LP) was suggested by my colleague Jakub Tomášek. The main idea is that the **P** matrices defining the quadratic norms are subjected to the so-called joint diagonalization.

---

¹) `http://homepages.laas.fr/henrion/software/gloptipoly3/`

²) `http://www.mathworks.com/matlabcentral/fileexchange/24478-groebner`

Through this technique a common orthogonal transformation matrix $\mathbf{V}$ is found such that $\mathbf{P}_i = \mathbf{V}\mathbf{D}_i\mathbf{V}^T$. The matrices $\mathbf{D}_i$ are as diagonal as possible providing a kind of average eigen-structure shared by the matrices $\mathbf{P}_i$ [33]. The optimization variables undergo exactly the same transformation. Having diagonal matrices in the quadratic forms, it is now possible to convert the problem into the LP and solve by the standard simplex algorithm. But since the joint diagonalization is in general only approximate, the found solution is not accurate. It is, however, a good initial choice for the local gradient based solvers like `fminsearch`. I took the implementation of Jakub Tomášek, extended it to allow more force constraints (more force requirements and thus more beads) and modified it in a way that it can be compiled into a `mex` function. On a benchmark test, the algorithm works quite well although the errors of the force magnitude are larger than preferred. On the other hand, the more important errors in the direction are on average below 5 % and the average execution time is only 3 ms.

The last optimization approach I will describe here is based on the **simulated annealing** (SA) algorithm. It is a generic probabilistic metaheuristic suitable for finding the global extreme of a function dependent on many variables. Especially good results can be achieved if the search space is discrete. Hence I discretized the search space so that only integer values are allowed as the voltage amplitudes. Then I utilized the existing simulated annealing implementation [1]) found on FEX. The approximate integer solution acquired through this random method was then used as a starting point to the `fminsearchcon`[2]), a modification of the classical `fminsearch` supporting also the general inequality constraints (also from FEX). Since the process is random, a good solution is not guaranteed to be found at every run. As a sufficient workaround, however, is to let the algorithm run several times in parallel (using the multithreading capability of the `parfor` command). The benchmark results are the best so far achieved. Both the errors in the magnitude and the direction are in the fractions of the percents and the average run-time is only 1.2 ms.

Table 5.1 summarizes the performance of all the solvers that were capable of delivering the solution of the given benchmark problem. Based on these results, the SA algorithm was despite its random nature chosen as the best one so far.

Algorithm	Mag. error (%)	Dir. error (%)	Run-time (ms)
IP (req. in constr.)	0.1774	0.0981	38.6
IP (req. in constr, over $\bar{\mathbf{d}}$)	0.0479	0.0289	25.3
IP (req. in objective fcn)	0.2800	0.0656	44.4
Nelder-Mead (over $\bar{\mathbf{d}}$)	4.1797	0.6983	**0.2**
SA	$\mathbf{3.72 \times 10^{-9}}$	$\mathbf{1.14 \times 10^{-9}}$	1.2
LP	83.1560	3.6909	3.0

Table 5.1. The comparison of the tried optimization solvers. The values in the table are the averaged results from the 100 measurements of the benchmark problem.

For the second type of the optimization task used in the experiments – optimization over the voltage phase shifts – again the solver based on the SA was chosen. As will be described in Section 6.1, the used 64-channel signal generator can produce the phase shifts only in steps of $\pi/8$, thus defining the discrete search space suitable for the SA. No further calls to the `fminsearchcon` are necessary in this case.

---

[1]) `https://www.mathworks.com/matlabcentral/fileexchange/10548-general-simulated-annealing-algorithm`

[2]) `https://www.mathworks.com/matlabcentral/fileexchange/8277-fminsearchbnd--fminsearchcon`

Chapter 6
Experimental results

In order to verify and asses the performance of the designed control strategies, a number of experiments was conducted. In these, both the standard parallel electrode array and the four-sector electrode array were used. The former one for a test of the controller based on the voltage amplitude modulation and the latter for a test of the voltage phase shift control. The existing laboratory setup was used and will be briefly described in the next section.

6.1 Laboratory setup description

Although the different types of the control require the partially distinct hardware setups, the main parts are still the same:

- camera – digital black-and-white camera (Pike F-032B, Allied, Germany) with a firewire interface mounted on the microscope (Olympus BX-FM, 5× magnification lens) for the image acquisition of the manipulation area; the beads appear in the image as black spots on a light background so their position can be easily extracted using an image thresholding.
- computer – personal computer (Intel i5, 3.30 GHz, 8 GB RAM, 64-bit, Win 7) which grabs the frames from the camera, analyses them (extracts the position of the beads) and then runs the control program implemented in Matlab & Simulink. The resulting control action is then interfaced with the signal generation block via an input/output card (MF624, Humusoft, Czech Republic) or a serial port communication;
- controlled signal generator — it drives the microelectrodes with the defined signals (varying in the amplitude or the phase) based on the controller outputs;
- electrode array.

Their arrangement is for the two specific laboratory setup variants shown in Figures 6.3 and 6.4. From the above description and the information flow indicated by the arrows it is apparent how the feedback loop is closed.

One of the variable components in the setup is naturally the electrode array. This is the main part of the whole system, since it is the place where the micromanipulation occurs. It typically comprises of the non-conducting substrate (e.g. glass), on which the microelectrodes, typically from gold or Indium tin oxide (ITO), are fabricated. The techniques of the fabrication process are detailed in [34]. Above all this, the open PDMS chamber is adhered to the surface. Its purpose is to hold the deionized water (conductivity of 50 µS/m) together with the immersed manipulated microobjects. In the experiments we use the polystyrene spheres with the diameter of 50 µm. For a comparison, the approximate sizes of a few comparable biological cells are shown in Table 6.1. Based on the desired degree of the motion freedom (1D or 2D), the parallel or the four-sector electrode layout is used. Both of these types were already described in Sections 3.1 and 4.1. Their photos are shown in Figures 6.1 and 6.2. For more details, please see [34–35].

object	size
human red blood cell	9 µm
most eukaryotic animal cells	10 − 30 µm
most eukaryotic plant cells	10 − 100 µm
small Amoeba	90 µm
human egg	90 µm

Table 6.1. The approximate sizes of the biological cells that are closest to the size of the test beads. The data in the table are taken from [36].

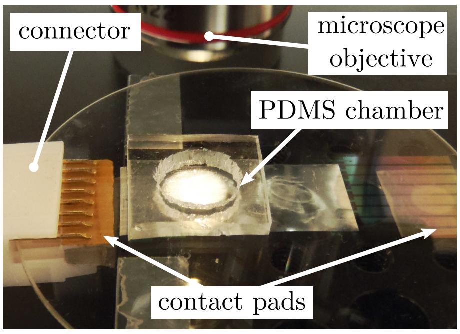

Figure 6.1. Photo of the parallel electrode array placed under the microscope.

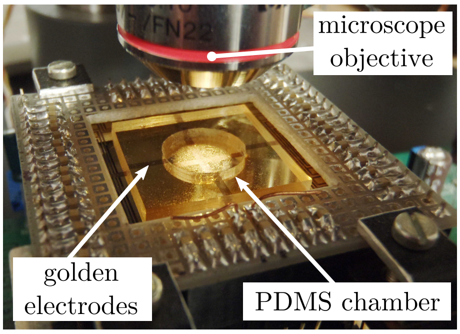

Figure 6.2. Photo of the four-sector electrode array placed under the microscope.

The second varying part of the experimental setup is the block of the voltage generation. The used hardware depends evidently on the choice of the controlled signal property. This can be either the phase shift between the individual output channels or the voltage amplitudes. Both of these hardware variations will be, in brief, discussed below, and where possible, a reference to the more in-depth description will be provided.

6.1.1 Amplitude control

The hardware setup for the amplitude control is capable of setting the amplitude of the sinusoidal voltage individually for each of its channels in a range of 0 V to 10 V and additionally a phase shift of 0 ° or 180 ° (this corresponds to the negative amplification factor of the basic signal). There can be maximally eight channels in total. This limitation is given by the number of the analog outputs of the PC's input/output card.

The basic part of the amplitude control hardware setup is the standard function generator (Agilent 33220A) used for a precise generation of the basic sinusoidal voltage of a given frequency. This signal is then as an input fed to a set of eight four-quadrant analog multipliers (AD633) and it is multiplied by eight voltages fetched from the PC's input/output card.

The used frequency of the sinusoidal signal for the DEP control is in our case 300 kHz, which corresponds to the negative DEP. This particular frequency value was selected so that the low frequency electrokinetic effects are avoided and the bandwidth of the used multipliers (1 MHz) is not exceeded.

A diagram depicting the laboratory setup used for controlling the DEP forces by changing the voltage amplitudes is in Figure 6.3.

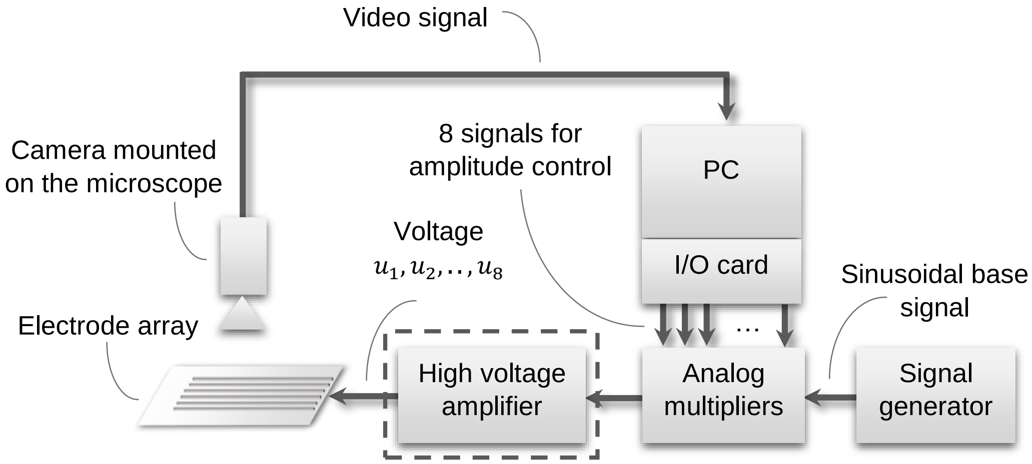

Figure 6.3. The diagram of the laboratory setup used for the DEP control capable of regulating the amplitudes of the voltage signals.

6.1.2 Phase shift control

The equipment for the phase shift control allows us to generate in total 64 channels containing rectangular signals shifted in the phase. The shift can be set discretely to 16 different values (0, $^{\pi}/_{8}$, ...). The respective generator was in a detail described many times (see [35, 11]). The basic frequency of the voltage signal was again set to 300 kHz.

A diagram depicting the laboratory setup used for controlling the DEP forces by adjusting the phase shifts of the used voltage signals is in Figure 6.4

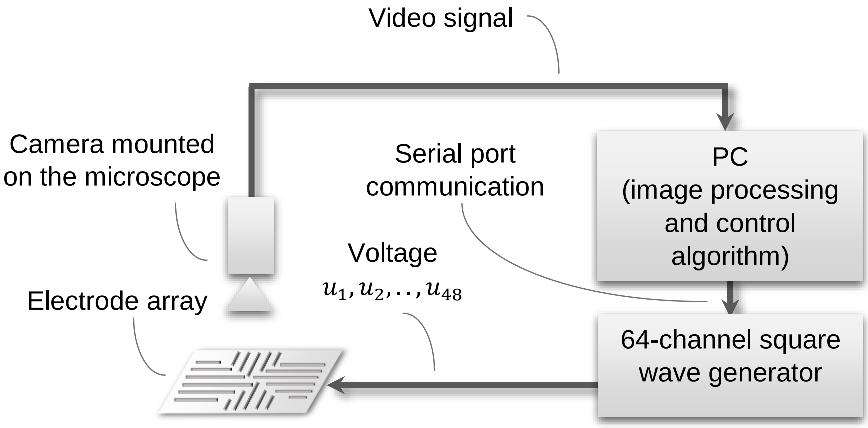

Figure 6.4. The diagram of the laboratory setup used for the DEP control capable of the phase shift setting of the used voltage signals individually on up to 64 electrodes.

6.2 Notes to the experiments

The experiments were typically preceded by a preparation phase. First, before a set of experiments was conducted, a thorough wash out of the manipulation chamber with a deionized water was done. This way, a presence of the dust particles and other dirt affecting the beads movement is reduced. The beads themselves are taken from the already diluted solution and inserted in an ampoule filled by a pure deionized water. Next, they were centrifuged, excessive water was sucked out and the beads were finally injected into the manipulation chamber. This way, the deionized water in the manipulation chamber should maintain its resistivity.

Then the beads were carefully carried by a water flow (created by a slight pumping with the pipette) into the field of view of the camera. This is done while the electrodes are under voltage and creating a repulsive DEP force preventing the particles from sticking to the bottom of the chamber. A force field under which they levitate at a height of 130 µm is used. At the same time this is assumed to be the initial levitation height for the consecutive experiments.

6.3 Parallel electrode array

First, a few experiments demonstrating just one bead position control were conducted. A user interface allowing the reference position change during the experiment was utilized. The presses of keyboard arrows were captured and according to them the reference position was incremented, respectively decremented by a small value (so small that it seems continuous in the reality). A graph from such the experiment is shown in Figure 6.5. It is obvious, that although some steady state errors are present (in the worst-case about 30 µm), the manipulation in a wide range of positions above the whole array is achievable. This confirms the prognosis based on the simulations in Section 3.2. The controller is robust enough that even without the vertical position measurement (and just assuming that the levitation height remains constant) the system works.

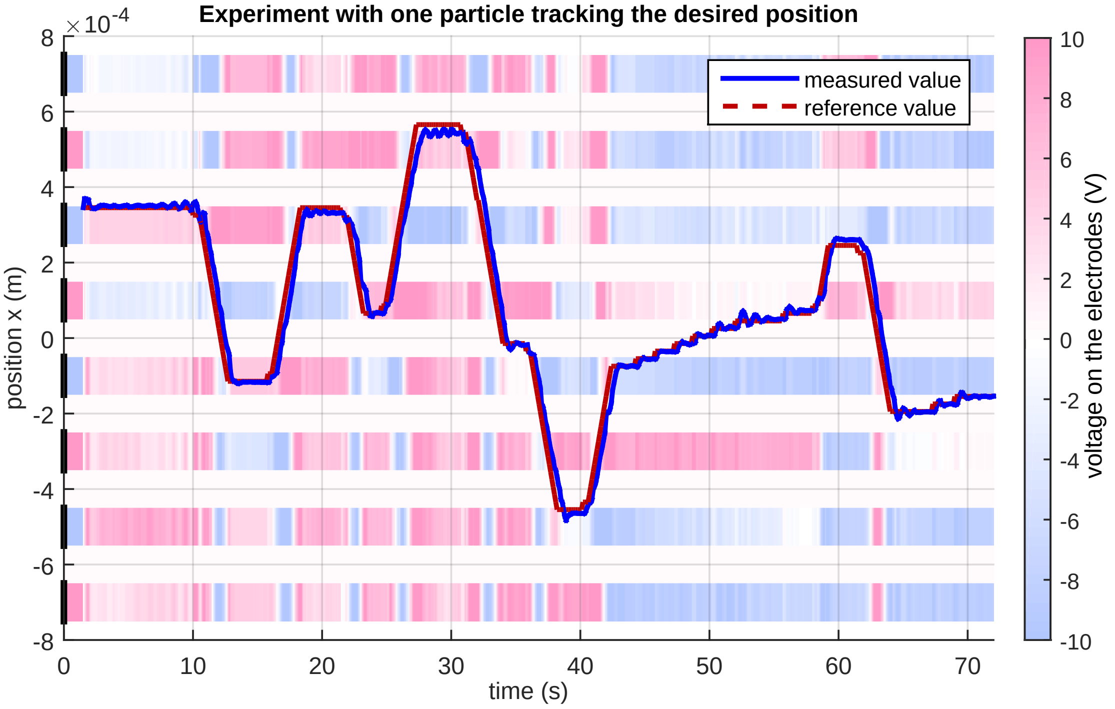

Figure 6.5. The experiment demonstrating one particle position control. The reference value was set manually by the operator during the experiment.

Next, a more detailed analysis of the manipulation precision (measured as the steady state position error) was done. A number of experiments was conducted, in which the particle was steered in sequence to the set of positions above the whole array. These comprised of the centers of the electrodes, their edges and the centers of the inter-electrode gaps. Each position was reached at least ten times. The resulting steady state errors were then statistically processed and the mean value and the standard deviation of the absolute value of the error was calculated. Figure 6.6 presents these results.

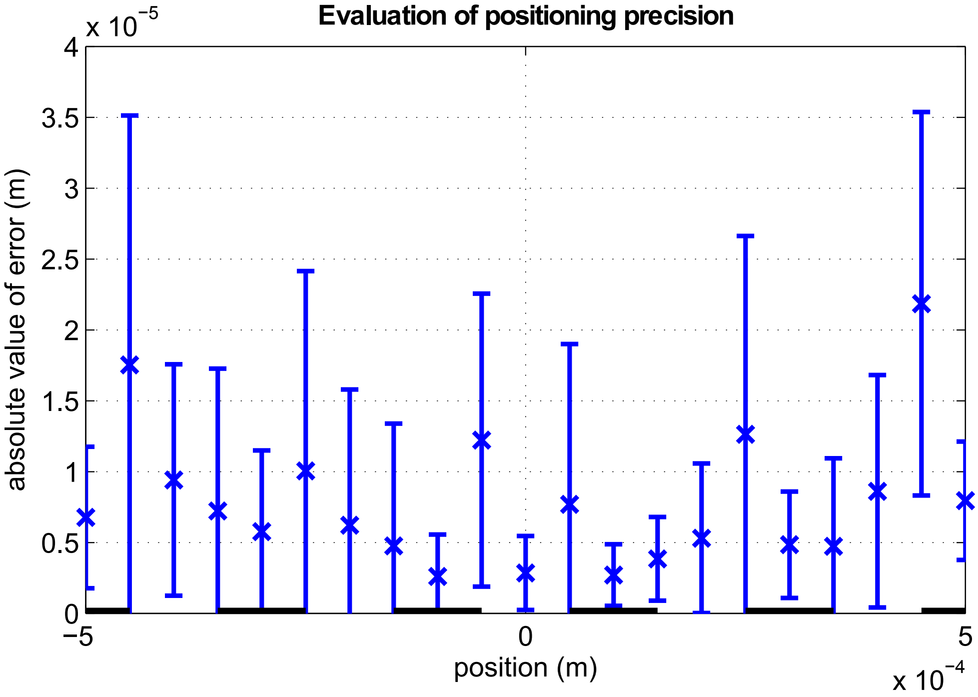

Figure 6.6. Mean value and the standard deviation of the absolute value of the error in different places of the array acquired from the series of measurements. Taken from [18].

Generally the error is larger above the edges of the electrodes and towards the end of the manipulation area (around 20 µm). The mean value of the error, however, still constitute only a fraction of the dimension of the bead (around 44 % at the worst, but typically only about 12 % of the diameter of the bead).

An example of these precision measurements was also used for the comparison of the experimental results and the simulation. Figure 6.7 shows that in the case of the experiment, the response of the system to a change in the reference is faster, but the overshoot (up to 37 µm) and the steady state errors (up to 17 µm) are larger than in the simulation. It was impossible to improve these values by further tuning of the proportional controller. Neither its extension by integration nor derivative components was helpful.

Simultaneous control with several particles was also tried. Figures 6.8 and 6.9 show the parallel independent control of the two, respectively three particles. Here the separation strategy based on the unstable equilibrium formation is used (see Section 3.2). This is necessary because the DEP forces acting on the two objects are identical if these have the same x coordinate positions. Practically, it is sufficient when the x coordinates of the beads are almost identical. This happens for example at the times: 52 s, 64 s, 87 s or 98 s. The same holds also for the three particle case in Figure 6.9.

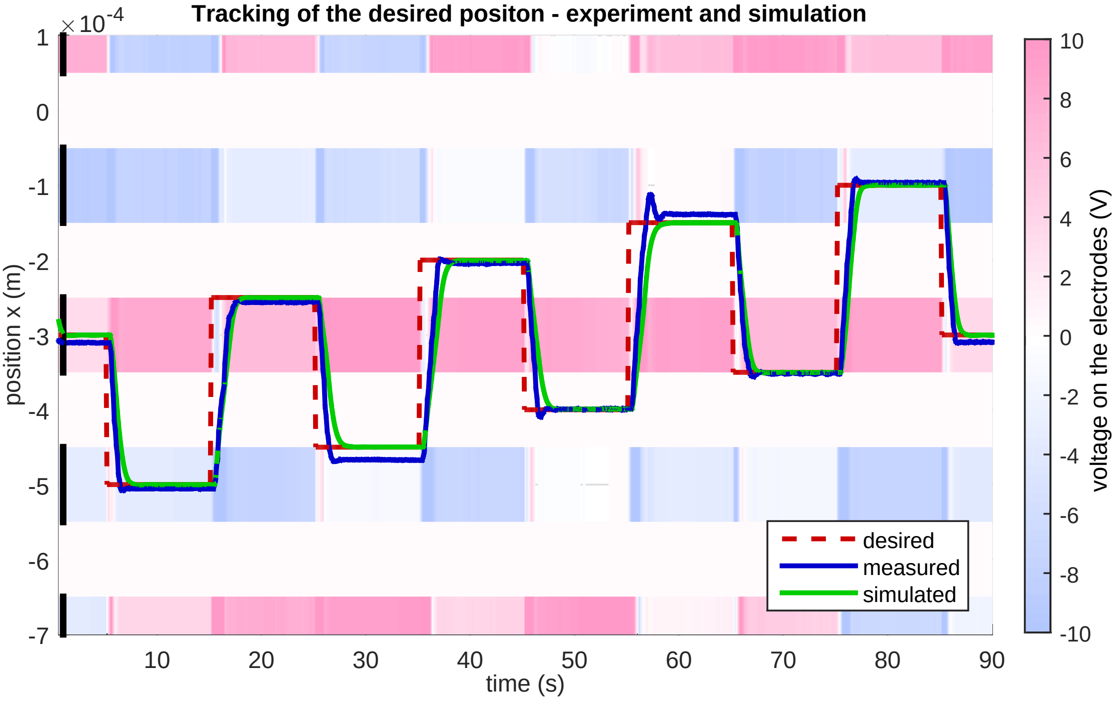

Figure 6.7. The comparison of the experiment and the simulation. The experimental data comes from the performed steady state error measurements. [18]

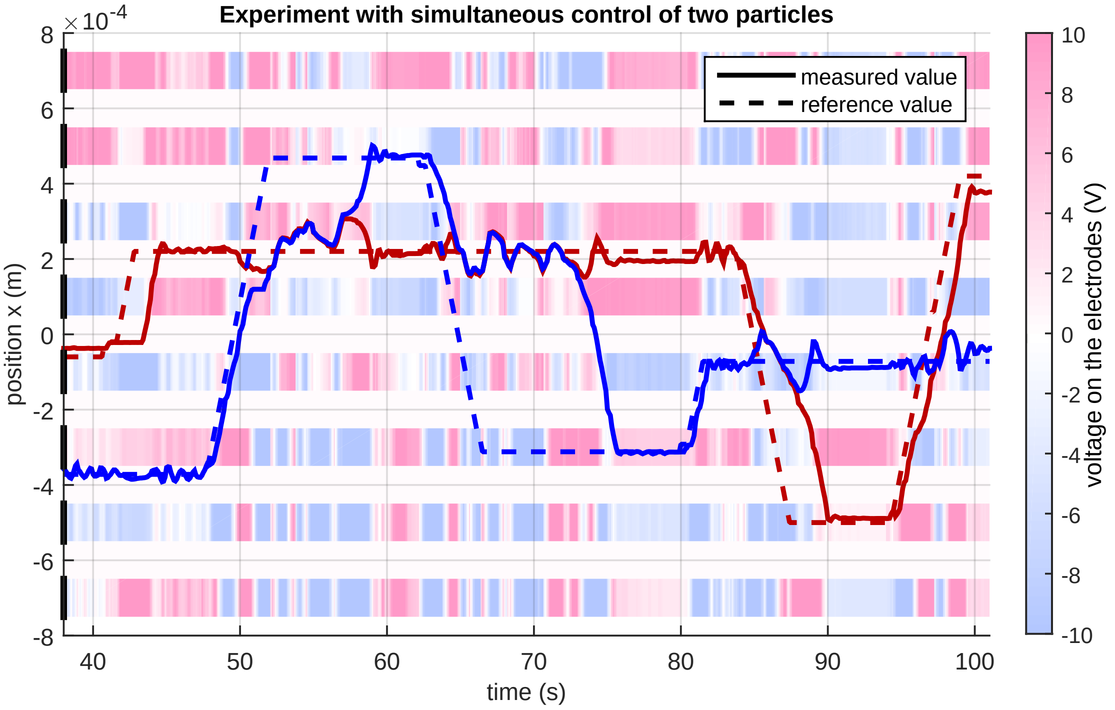

Figure 6.8. The experimental results showing simultaneous independent control of the two particles. The separation strategy based on the unstable equilibrium formation described in Section 3.2 is used when the two particles share the same position coordinate.

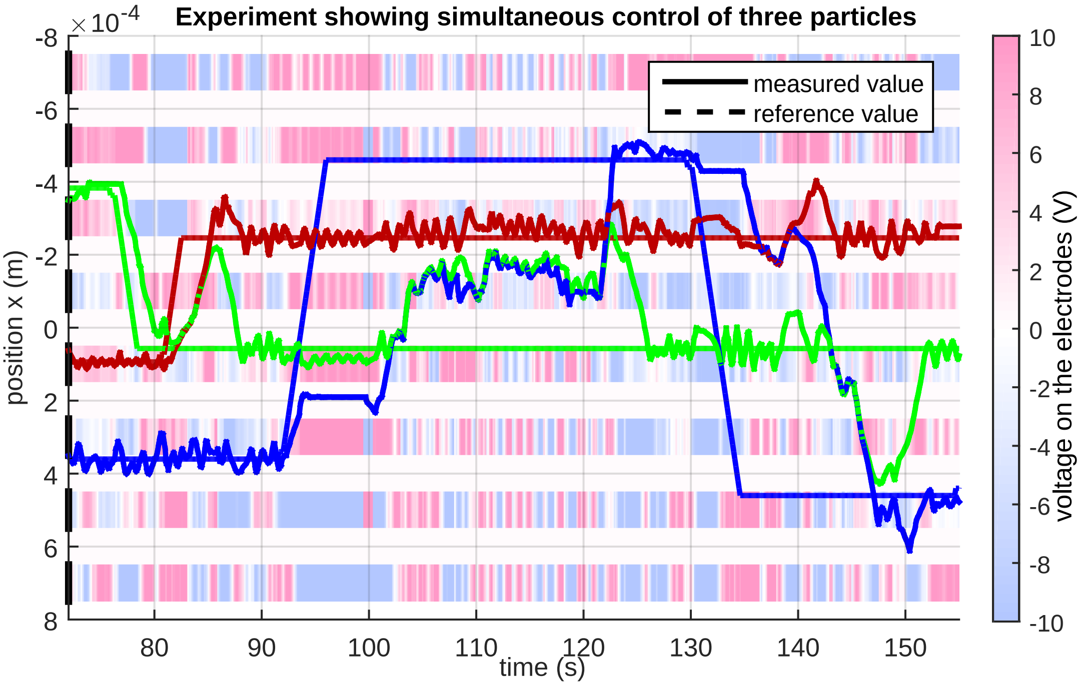

Figure 6.9. Experimental results showing the simultaneous control of three particles. [18]

It is evident that the more particles is controlled, the greater the steady state position errors become. Especially for the three particle case the measured positions are very oscillatory and the deviations from the desired finial positions of the beads reach up to 70 µm, a lot more than in the case of one bead control. This is due to the fact that the optimization task is more complex and a better solution is not found in the given time restrictions. Screenshots corresponding to this last described experiment showing the positions of the beads at times $t = 83\,\mathrm{s}$, resp. $t = 89\,\mathrm{s}$ are in Figure 6.10.

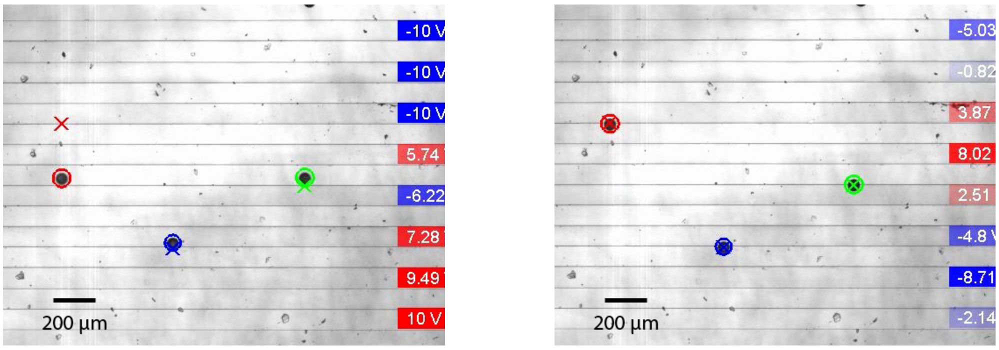

a) b)

Figure 6.10. The video screenshots with the marked beads and labels of the electrodes showing the currently present voltage. The images correspond to the times (a) $t = 83\,\mathrm{s}$ and (b) $t = 89\,\mathrm{s}$ of the experiment shown in Figure 6.9. Taken from [18].

The position interchange maneuver was, however, successfully completed even for the three particles. Hence we can conclude that the simultaneous manipulation of three particles is possible.

6.4 Four-sector electrode array

First, alike as in the case of the parallel array, the experiments demonstrating just one bead position control were conducted. The results are shown in Figures 6.11 and 6.12. It is evident that the real capabilities of the control system match the predictions from the simulations. Indeed, it is not only possible to move the bead in the direction perpendicular to the underlying electrodes, but also in the direction parallel to them. This is because the optimization based controller is still able to deliver a satisfactory force by utilizing the impact of even the far electrodes.

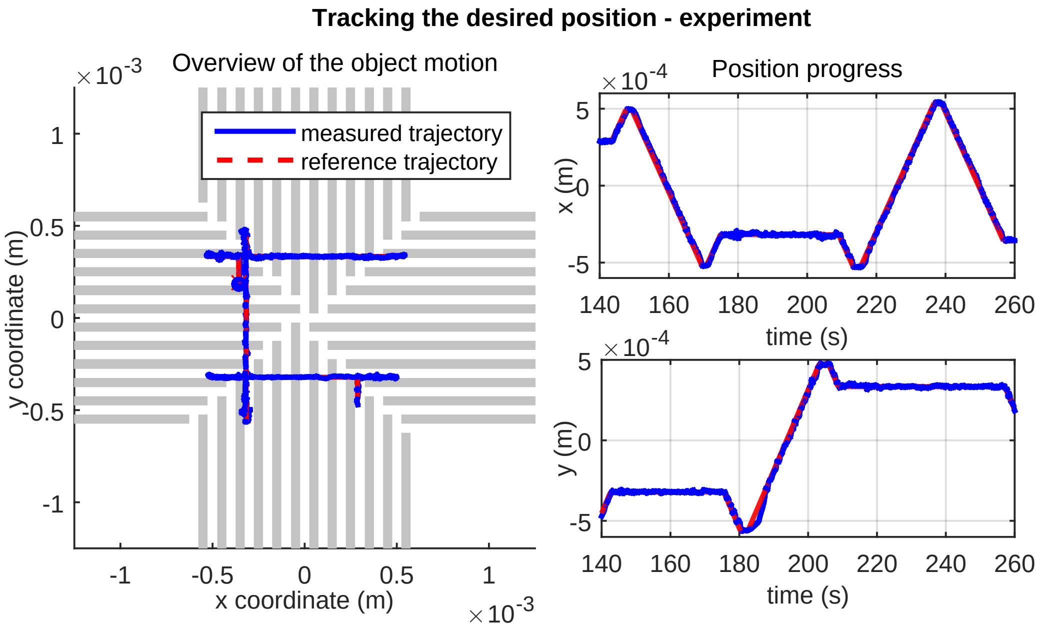

Figure 6.11. Experiment demonstrating the manipulation capabilities with one bead.

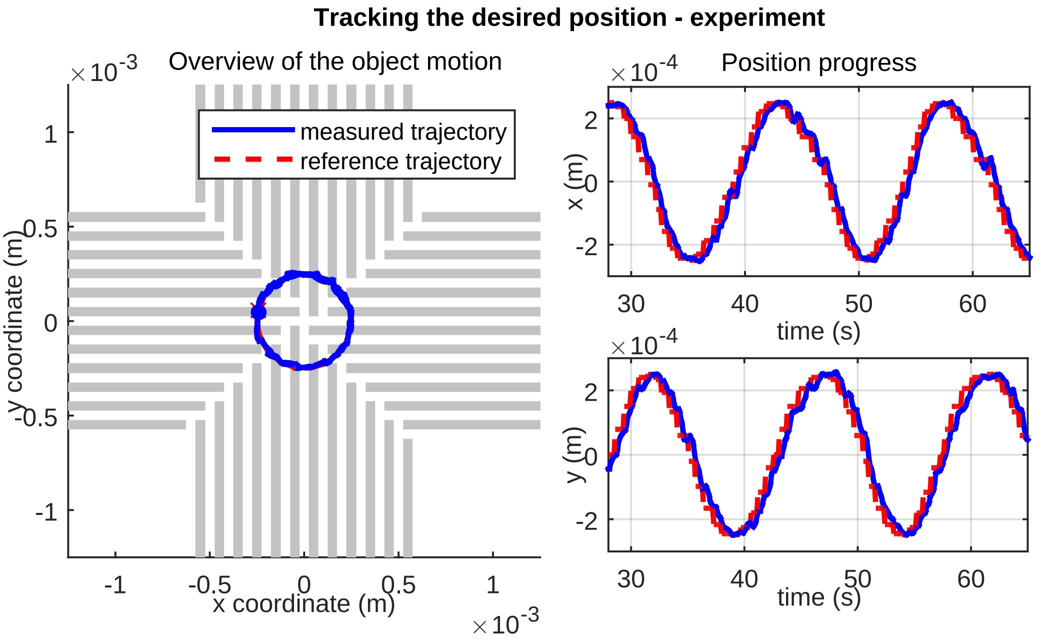

Figure 6.12. Experiment showing the circular reference trajectory tracking.

The both figures are in addition supplemented with the screenshots from the videos enhanced by visualization. The colored stripes labeling the electrodes are related to the phase shift of the voltage signal applied to them. The gray surface above the electrodes in a 3D graph visualizes the virtual potential. The bead sitting on its surface always moves down the hill in a direction of a negative gradient. In Figure 6.13 a situation when the bead is steered from the corner of the array is shown, whereas in Figure 6.14 a bulge pushing the bead ahead of itself along the circular trajectory is shown.

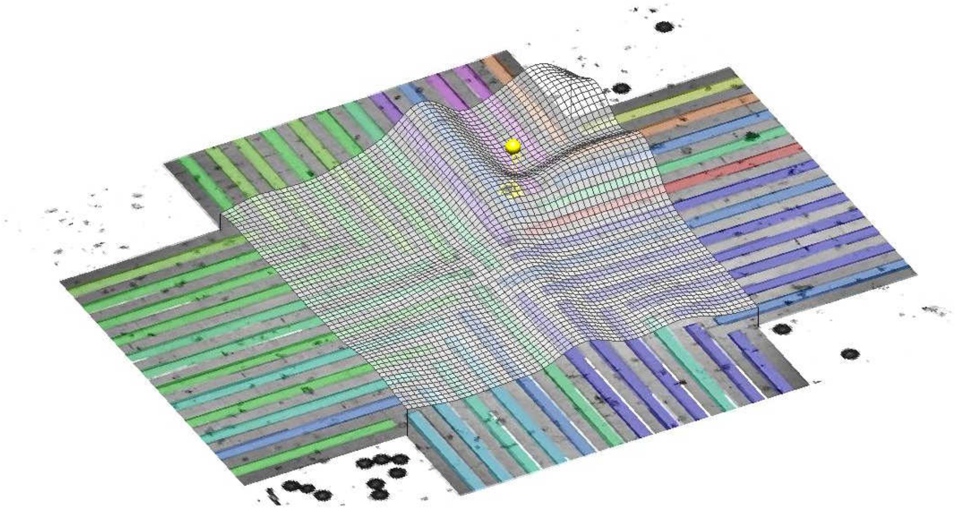

Figure 6.13. Visualization of the virtual potential landscape for the first experiment.

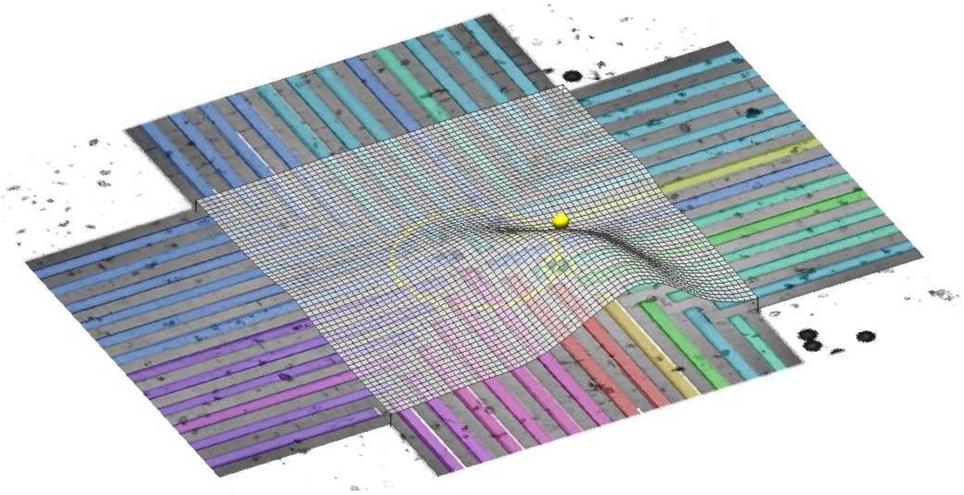

Figure 6.14. Visualization of the virtual potential landscape for the second experiment.

In the next set of experiments, the manipulation precision in the form of the steady state error for different reference positions was measured. For the sake of reducing the experimental load, the fact that the array is symmetric was exploited and just one of the four identical quarters was used for the measurement. A grid of 12×12 points was generated and the bead was repeatedly steered to them. Some minimal distance between the subsequent reference positions was kept in addition, so that the bead always approached the reference point having the maximal velocity. The steady state errors were then recorded and statistically processed. The mean and the standard deviation of the absolute error values were computed for each of the points and are shown in Figure 6.15.

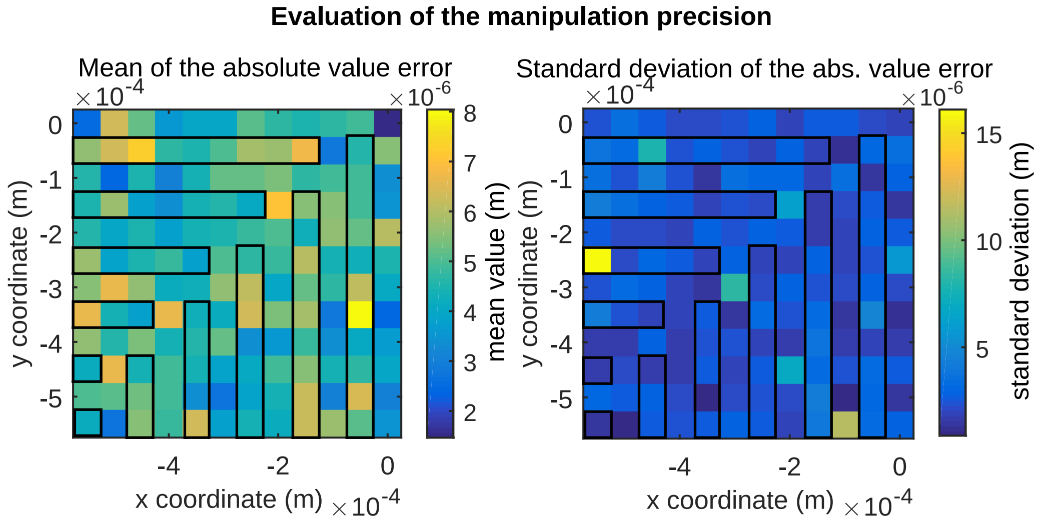

Figure 6.15. The evaluation of the positioning precision – the mean and the standard deviation of the absolute error value.

The comparison of the experiment and the appropriate simulation was also performed. Tracking of the circular trajectory was used and the results are shown in Figure 6.16. Even in reality, the controller is able to steer the bead along such a trajectory. The reason why the circle traveled in the simulation has a smaller radius (217 µm compared to the full size of 250 µm) is that bead does not move so fast as in the reality and thus lags behind the reference signal. This causes that the simulated particle takes a shorter path through the inside of the circle.

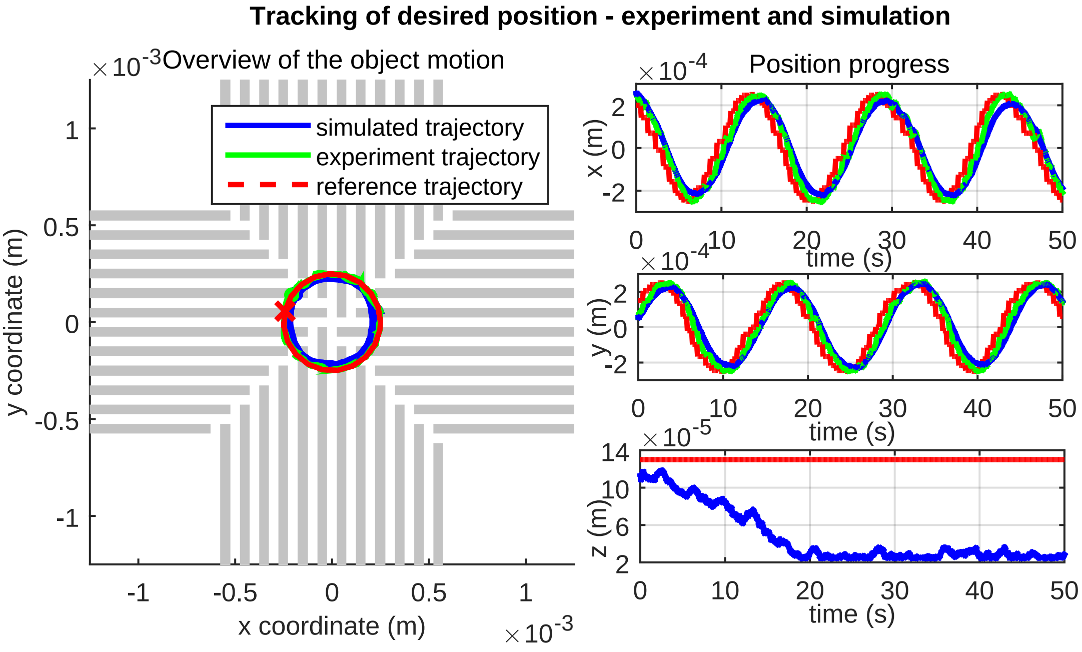

Figure 6.16. Tracking of the circular trajectory – experiment and simulation.

Finally, the manipulation of more particles was tried. The results of the experiment with parallel manipulation of the two beads is shown in Figure 6.17. Independent steering of the two particles was successfully demonstrated. Furthermore, in the scope of this experiments, the beads were repeatedly brought together and then again separated without any difficulties.

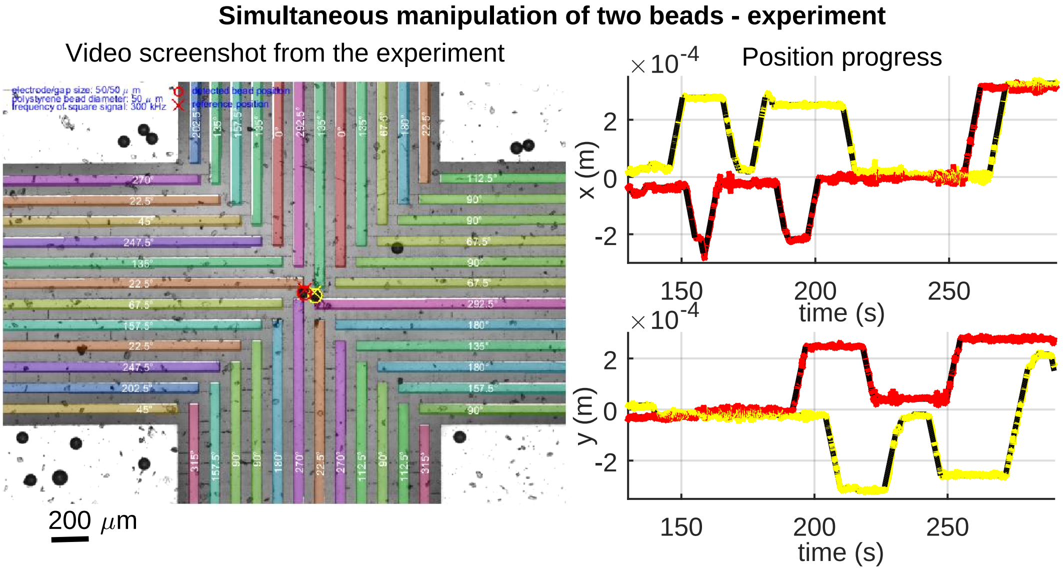

Figure 6.17. The simultaneous manipulation of the two particles. In the scope of this experiments, the beads were repeatedly brought together and then again separated.

In Figure 6.18, the manipulation of three particles is presented. As more force requirements are added to the optimization criterion, it again becomes more difficult to meet all of them at the same time. Although the independent manipulation of the three beads is still possible, it can be seen that the beads oscillate a lot around their respective steady state positions. The virtual potential visualization shows how the final positions of the beads are permanently being corrected, because no local minima are created for them.

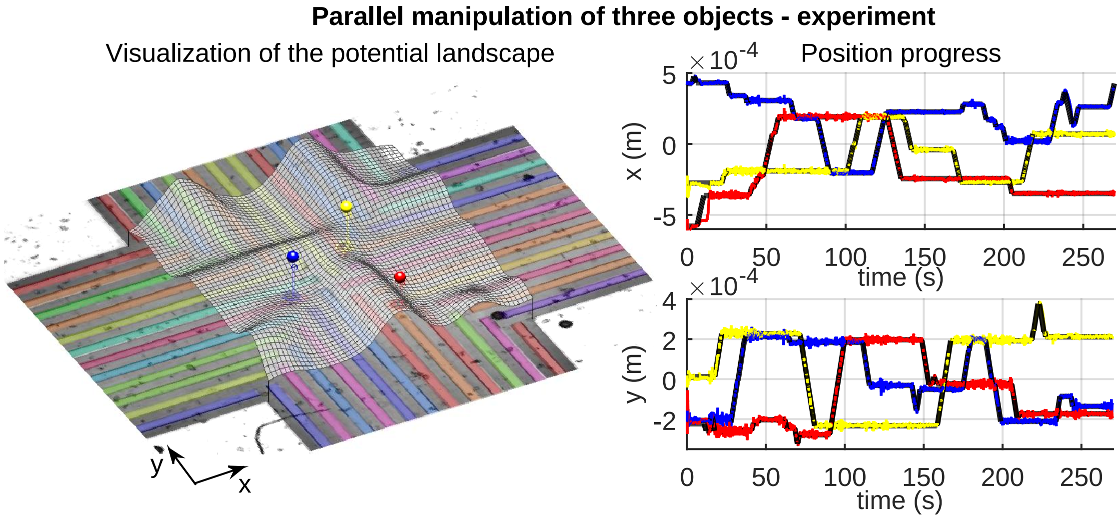

Figure 6.18. The experiment showing the simultaneous position control of the three particles.

Chapter 7
Computational issues

One of the key advantages of the proposed control algorithm is its versatility concerning the used electrode array layout design. This was demonstrated in Chapter 4.1 by applying practically the same control algorithm, as was used in the case of the parallel electrode array, to the more sophisticated four-sector electrode array. This property not only provides a great flexibility in an electrode array design, but also naturally raises a question of the system scalability. By simply adding more electrodes to the parallel array the manipulation area can be extended and the 1D motion can occur and be controlled over greater distances. Moreover, by using some even more sophisticated electrode array layouts allowing for the 2D manipulation and at the same time being easy extensible in all the directions (e.g. the matrix electrode array) the 2D/3D manipulation over a theoretically arbitrarily large area should be possible.

There are, however, two major obstacles that have to be overcome in the practical realizations. The first one is related to the capabilities of the sensor. So far, we have been using in our experiments a camera mounted on the microscope, which has relatively small field of view at the given necessary magnification factor. Some experiments with lens-less position sensing using a bare camera CMOS chip laying under the transparent electrode array were, however, carried out successfully. Although no efforts were invested in the investigation of using an array of these chips so far, I believe it could be a future way of the position sensing on the larger electrode arrays. Nevertheless, this reason alone does not allow us to experiment with much larger electrode arrays. The second problem regarding the system scalability is the computational demand of the control algorithm, which will rise with the increasing number of electrodes and the manipulated particles. This chapter will be devoted to the investigation of these issues and the suggestions of the possible solutions.

7.1 Using more beads

The influence of the increasing number of beads onto the computational demands was tested in a set of measurements. The most demanding is the control algorithm, specifically the optimization task solved within it. The parallel array controlled only by the changes of the voltage phase shifts was used for the analysis. One benchmark task was solved subsequently for an increasing number of particles and its computational demand was measured (as the optimization run time). Again the notebook equipped with Intel i5 (2.27 GHz), 8 GB RAM and Windows 7 (64-bit) was used for the measurement. For the each given number of beads the task was solved 1000 times and the averaged results were used to eliminate the stochastic nature of the SA optimization approach as much as possible. The positions of the beads were not chosen randomly, but always equidistantly and the group was centered above the array at the working height of 130 μm. The separation distance was either 200 μm in a case when all the beads fitted into the range −600–600 μm or appropriately smaller (the utmost beads were then at ±600 μm). The optimization goals (the desired forces) were chosen in all the cases based on the same precomputed reference force field so that it was known for sure that an exact zero error solution to the optimization task exists.

The only difficulty in these measurements was that the parameters of the SA solver (the number of iterations, ...) had to be adjusted manually for each particular number of particles in order to guarantee the acceptable errors (specified as the error in the force direction being lower than 5 %) of the found solution with the minimal computational demands at the same time. The parameter tuning is unfortunately not unambiguous and so the results presented in Figure 7.1 are rather approximate. Still the trend is pretty clear. The linear dependence of the combinational time on the number of particles is obvious from the figure. This nice property will not pose any insurmountable difficulty regarding the future system expansion.

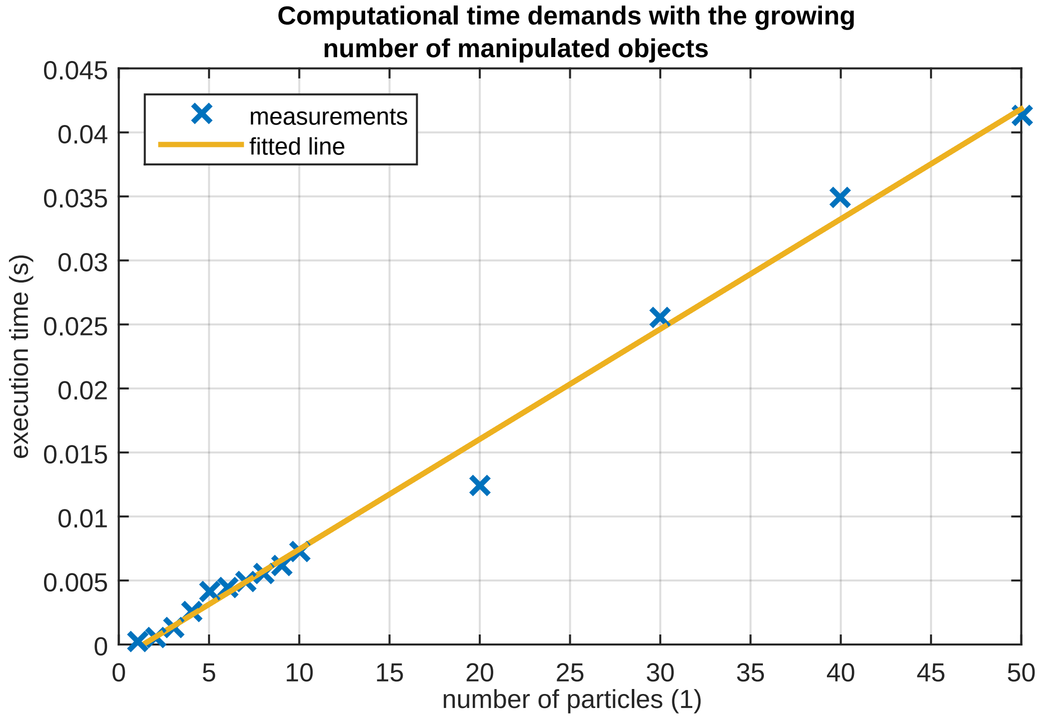

Figure 7.1. The analysis of the increase in the computational time demands with the growing number of the manipulated objects.

7.2 Using more electrodes

Just as in the case of the increasing number of particles, the computational demands also grow with the increasing number of electrodes. More electrodes means directly more variables over which the optimization runs. Furthermore, besides the growing computational demands, a memory issues may arise.

For a particular number of electrodes, a horizontal force having the magnitude of 25 N in the array center and at the height of 130 µm was searched. This was again done repeatedly (100×) and the resulting execution times were averaged. The Figure 7.2 shows these measurements. The acquired data can be fitted by a cubic function. The conclusion that the computational demands rise with the cube of the number of the electrodes could pose a major obstacle in the future system expansion.

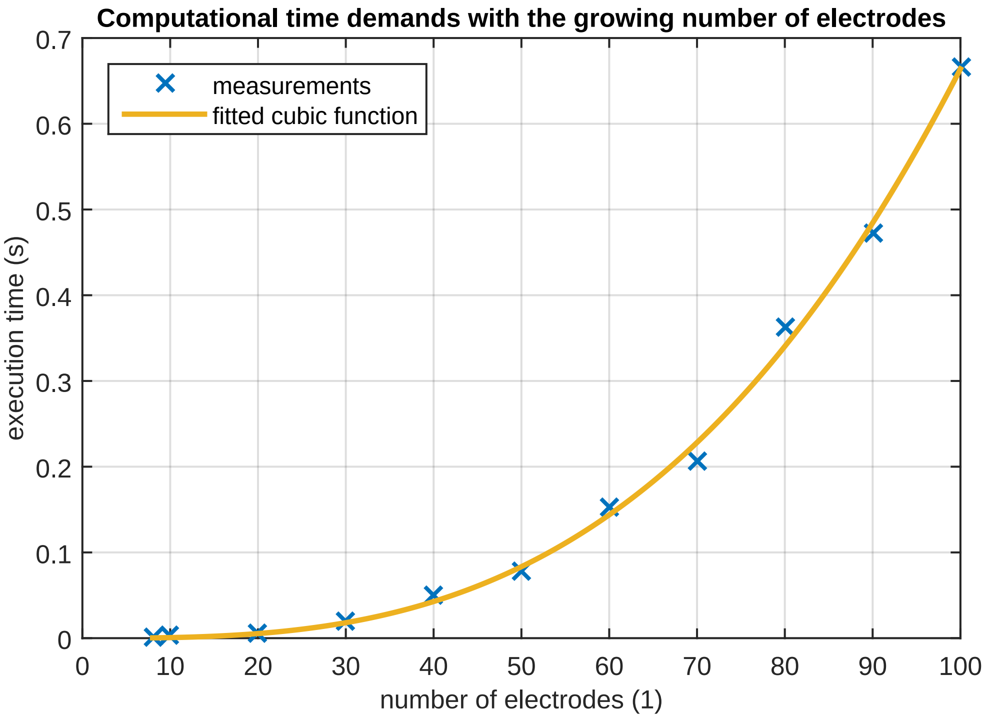

Figure 7.2. The analysis of the increase in the computational time demands with the growing number of the actuating electrodes.

7.3 Localized optimization

A straightforward possible solution to the aforementioned computational issues is to divide the one large optimization problem into a number of smaller subproblems, solve these only locally and then merge the local solutions into a global one complying with the original force requirements. This is possible just because the force at a given place is influenced only by the near electrodes and that the far electrodes can be neglected. The problem decomposition, local solving and the subsequent solution merging can be performed in many different ways. In this section I will introduce several of the them and analyze in a greater detail the most promising ones.

First of all, however, I will investigate what is the minimal distance for the electrode to have a negligible influence. This is the key information needed in all the approaches. To this purpose I performed a set of measurements using the optimization task for the 20 parallel electrodes and just the phase shift control. First, voltage signals with a random phase shifts were applied to the electrodes and the force arising in the middle of the array and in the levitation height of 130 µm was computed. This was taken as a reference solution and then modified in a way that only signals on the N electrodes closest to the particle stayed untouched and the remaining ones were set to have a random phase shift. A new simulation was then again performed and the error in the direction as well as in the magnitude between the reference force and the newly calculated one was recorded. The whole described procedure repeated 10000 times for each value of $N = 2, 4, 8, \dots$ and the resulting errors were then averaged for each N. The graph showing the results can be seen in Figure 7.3. By prescribing the error tolerance separately on the error in the magnitude and in the direction (denoted by the dashed line), I found out that the number of the closest electrodes that have non-negligible influence in the point of interest is equal to 10. This is definitely not a small number.

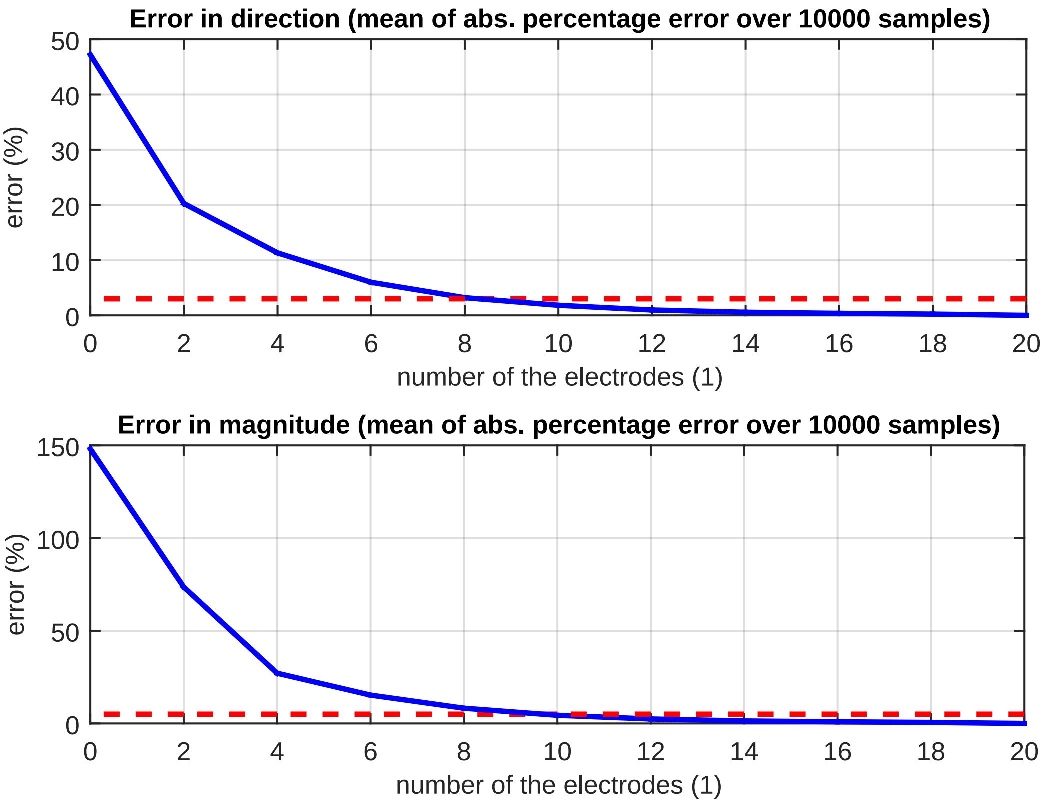
Error in direction (mean of abs. percentage error over 10000 samples)

Error in magnitude (mean of abs. percentage error over 10000 samples)

Figure 7.3. The analysis of the influence of the electrodes with the growing distance from the point of the interest.

In a case when the distribution of the particles in the manipulation area is rather sparse and there does not exist any electrode contributing significantly to the force of more than one particle, the optimization decomposition problem is relatively straightforward. One optimization task over the set of the influential electrodes is solved for each of the particles and the determined voltage phase shifts are directly applied to the corresponding electrodes. The phase shifts on the rest of the electrodes can be set arbitrarily, since the effect of these electrodes on the resulting forces at the locations of the beads is negligible. The difficulty arises when some of the particles are so close to each other that they share some of the influential electrodes (there exist some electrodes having the non-negligible effect on more than one particle at the same time). A few of the ideas for solving such situations are the following:

- The manipulation area would be divided into a number of fixed clusters of a given size (e.g. such that each would contain a certain number of electrodes) and the optimization task would be solved in each one of them separately. There would be also necessary an inter-cluster communication in situations when the particles would be located near the cluster boundaries.
- The clusters would be created dynamically based on the occurrence of the particles. In a case of more particles close to each other the appropriate clusters would be merged in a one bigger.
- Consider each one particle as being an agent enforcing its own interests (the desired force in a given location). In case of a conflict (when there are more particles close to each other sharing the actuators and possibly having different requirements for the forces) the compromise would be searched.

The problem of the first and the most straightforward idea is the already mentioned situation with the particles near the cluster boundaries. The inter-cluster communication would be probably too challenging in these cases.

The dynamical clusters, which, if necessary, merge into a bigger one totally avoid the communication needs. The problem may however arise, when the object distribution generates excessively large clusters – in extreme case just one cluster containing all the particles. In such a case, this strategy does not help at all.

The last stated approach seems the most promising. One way of accomplishing this is to use an algorithm based on the so-called distributed subgradient method [37]. The idea taken over is that each agent (in this particular case the bead) would have assigned its own optimization problem (minimizing error of the force acting on it) which will be simultaneously solved by some kind of the gradient method. After each iteration of this method, some information (a partial solution) would be locally interchanged between the near beads (sharing some of the electrodes). The receiving bead would then combine its own partial solution and the solution fo the neighbors through some defined weights (see Figure 7.4) and perform the next optimization step. Ideally, this will result in the solution convergence.

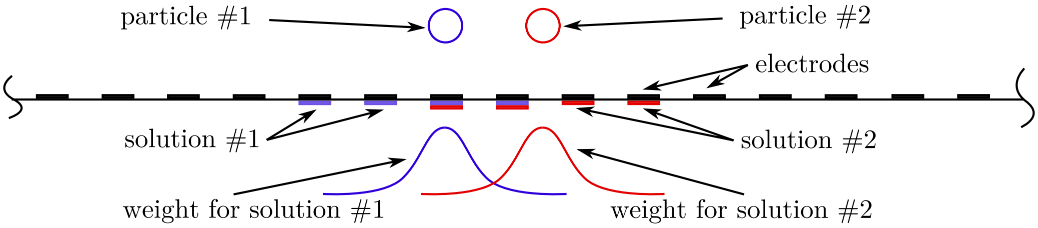

Figure 7.4. The typical weights used in the process of the solution merging. For a simplicity, each shown solution prescribes the voltages only on the four electrodes closest to the particle (two of them are shared). On the first shared electrode, the solution #1 will dominate, since the its weight is higher. Similarly, in the case of the second shared electrode, the second solution will dominate (although not so much this time).

The main obstacle is that all the papers describing the distributed subgradient method are devoted towards the convex optimization solvable using the gradient descent methods. As was shown in Chapter 5.1, this does not fit to our problem. However, using the SA it is at least possible to simulate the iterative convergence of the partial solutions. This is done by limiting the number of the SA inner iterations and by starting its next run from the last found solution. The test of this approach, however, gave only unsatisfactory results (even when a solution provably existed).

Another quite similar approach is to perform the optimization in a sequence. For a simpler explanation, let us consider for example an optimization searching forces for the three particles. First, an optimization task involving just the first particle and its objectives is solved over the 10 closest significant electrodes. The partial solution is then stored into a shared vector for the global solution. Then the second optimization task based on the demands of the second particle takes place. This time the starting value of the SA is set based on the corresponding values from the global vector of the solutions. The results are again stored, possibly overwriting the present values. The same happens with the third particle and then the whole process repeats. However, the more iterations pass off, the less is the SA allowed to move from its starting point. This is accomplished by keeping a counter for each element of the global solution and decrementing its value with each writing into it. The idea again is that the global solution could converge this way. The experimental results are, however, not very promising. A good solution was found only for a trivial case of the two particles separated by a distance of around 300 µm at a minimum and even in this case a rather large number of the iterations was required (around 100).

The last tried approach to merging the several different solutions into the global one is based on the idea that it would be easier if the individual solutions somehow built on themselves. For example, by firstly negotiating the force field for the whole manipulation area all the compromises would be solved and there would be no more any conflicting goals in the individual optimization tasks (see Figure 7.5). Since all of them make an effort to satisfy a common objective, the final merging of the individual solutions could be an easier task to do. The mutually corresponding elements of the found solutions (either the vectors of the control variables or rather their differences) could have similar values. This is, however, not guaranteed (and as it showed later in the experiments, it sometimes really need not to happen). The composition of the global final solution could be therefore done by their simple averaging (see Figure 7.6). Additionally, the weights could by included for preferring the elements of the partial solutions corresponding to the close locations.

For a better understanding, I will demonstrate the whole process on a simple example, where a force field the bringing two particles together is searched for. Large parallel electrode array with 20 electrodes is used. The beads are located at the coordinates $x = \pm 100\,\mu\text{m}$, $y = 130\,\mu\text{m}$ (depicted as black circles in Figure 7.7). In the same figure the red lines beginning in the centers of the circles represent the direction of the desired force. As it was described in the previous paragraph, the common force field is negotiated first. This is demonstrated in Figure 7.5. The red, respectively blue lines represent the desired forces demanded by the first, respectively the second particle. The specific shape of these curves is based on the typical force profile get in the simulations performed for one particle. The yellow line in the same figure then represents the averaged desired force. Based on this, the inputs to the two individual optimization tasks will be determined. The optimization will run over 10 electrodes, which cover pretty large area. Therefore more than one force objectives has to be used. In fact, 15 objectives are used in each of the task (in figure they are marked by the red, resp. the blue dots). Note that they are not distributed equidistantly in the x direction, but they are a little denser close to the position of the corresponding particle. This way, the error in force at the given position will be small enough and at the same time at least the essence of the overall demanded force profile will be achieved. Results of the two optimization tasks are shown in Figure 7.6. Since the optimization runs over the control variable differences, the result consist only from 19 elements. Because both of the task tried to achieved the same goal, their results are almost the same. The yellow circles represent then the merged solution (weighted average with the weights influenced by the distance from the corresponding particle). The resulting force field is depicted in Figure 7.7.

The example was chosen so that the number of the electrodes shared by the two particles was large and thus the solution merging could be nicely demonstrated. The same approach can be used for finding the solutions also in cases where more than two particles are present. The purpose of the method is clear – instead of performing the optimization over many electrodes but with a small number of objectives (two for each particle), the optimization runs just over 10 electrodes but with a much higher number of objectives (15× the number of particles N). Based on the measurements of the computational demands made earlier, this should be advantageous when having an array with 38 or more electrodes.

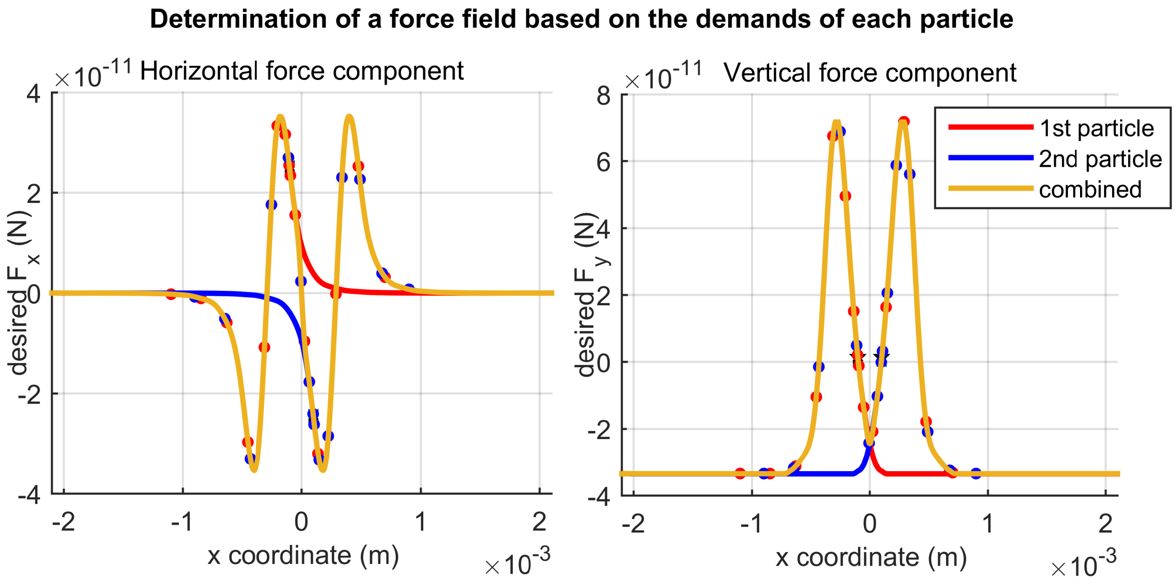

Figure 7.5. The creation of a common force field further used as a base for the optimization.

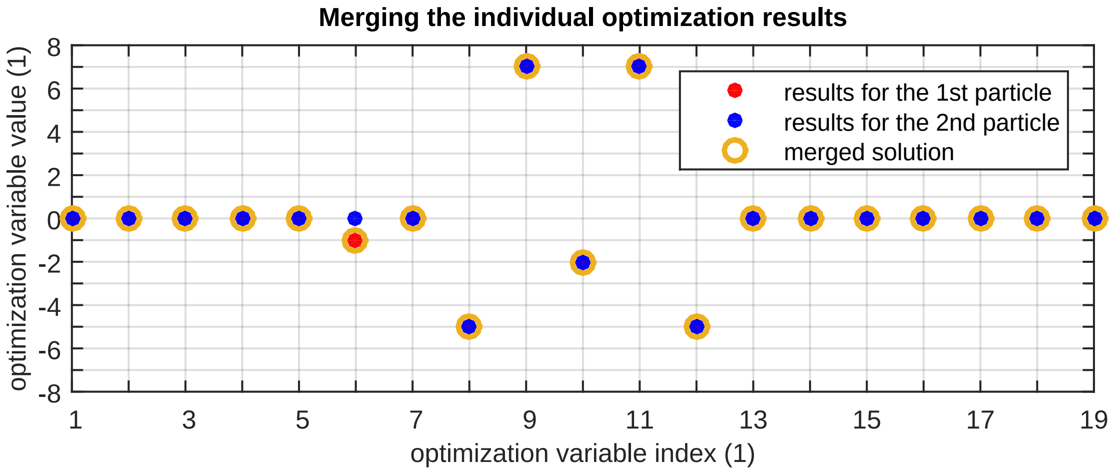

Figure 7.6. The merging the two optimization solutions into the one global.

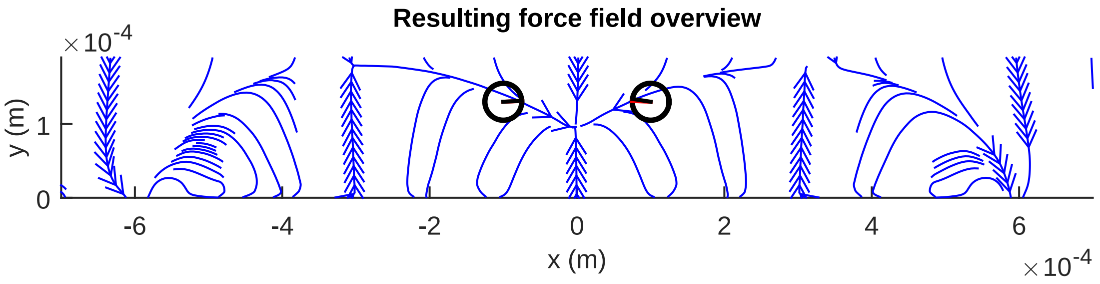

Figure 7.7. The resulting force field simulation (just the central segment of the array).

The method was tested on a few other simple tasks, but it has unfortunately not always achieved such nice results as in the above example. Although the individual optimization tasks end up successfully, the solutions could not be merged by a simple weighted average. One of the possible problematic parts may be the determination of the common force field, since its formation is currently rather heuristic.

7.4 Mutual particle interactions

In a typical micromanipulation device, a common required task is to bring two or more particles together or to separate them. Moreover, solutions (in the chemical meaning of the word) containing tens or hundreds of particles are used. These come naturally often in a close contact with each other. In all of these situations the mutual interaction forces between the particles become non-negligible and should be therefore taken into account. So far the performed experiments included just one isolated particle or a small number of sufficiently distant particles. Therefore the modelling of the mutual particle interactions was of no interest. However, with the extension of the control scheme for a platform capable of 2D manipulation (and thus opening the new experimental possibilities), the interactions effects should be studied.

The vast majority of the papers dealing with mutual particle interactions concentrate on the case of the two particles located in the uniform electric field. Their stable respectively unstable orientations are in such a case determined. In the most common case where both the particles experience either the positive or the negative DEP, the stable orientation is parallel to the applied field [3]. On the contrary, the unlike particles orient perpendicularly to the applied field. These results agree with the experimental observations, the so-called pearl-chaining.

A few different and variously accurate methods for modelling of the mutual particle force interactions were reported in the literature. The most accurate, but also the most computationally demanding, is the aforementioned MST method. Using a FEM solver and the arbitrary Lagrangian-Eulerian method (ALE) Ai and Qian [38] considered even the hydrodynamic interactions which are according to them non-negligible at short distances. Computationally less demanding, but still unsuitable for the control usage is the hybrid immersed boundary and the immersed interface methods [39]. A completely different approach is to use the *equivalent multipole method* [40], which is, however, already just approximate. The level of the approximation may be however chosen by the degree of the used multipoles [41]. Since we are highly restricted by the computational time limits, we will use just the simple point-dipole (possibly further extended by a simple hydrodynamic) interactions model described in [42]. The drawback is of course its accuracy at the very short inter-particle distances.

I will begin by considering a situation where N particles are mutually influencing each other just electrostatically. According to the referred paper, the total electrostatic force affecting the ith particle can be approximated by

$$\mathbf{F}_{\mathrm{E},i} = \mathbf{F}_{\mathrm{DEP},i} + \mathbf{F}_{\mathrm{D},i} - \mathbf{F}_{\mathrm{rep},i}, \quad i = 1...N, \tag{7.1}$$

where $\mathbf{F}_{\mathrm{DEP},i}$ is the DEP force acting on the ith particle (see Eq. (3.6)), $\mathbf{F}_{\mathrm{D},i} = \sum_{\mathrm{I}=1,i\neq j}^{N} \mathbf{F}_{\mathrm{D},ij}$ and $\mathbf{F}_{\mathrm{rep},i} = \sum_{\mathrm{I}=1,i\neq j}^{N} \mathbf{F}_{\mathrm{rep},ij}$ are the electrostatic interaction, respectively the repulsive force acting on the ith particle. The purpose of the repulsive force is to prevent the particles from overlapping. As it is apparent, the interaction force is composed of the individual contributions from the $N-1$ other remaining particles. These can be expressed after time-averaging as

$$\mathbf{F}_{\mathrm{D},ij} = \frac{1}{4\pi\varepsilon_{\mathrm{m}}} \cdot \frac{3}{\mathbf{R}_{ij}^{5}} \begin{pmatrix} \mathbf{R}_{ij}\mathcal{R}\left[\frac{1}{2}\tilde{\mathbf{p}}_{\mathbf{i}}^{\mathbf{T}}\tilde{\mathbf{p}}_{\mathbf{j}}^{*}\right] + \mathcal{R}\left[\frac{1}{2}\left(\mathbf{R}_{ij}^{T}\tilde{\mathbf{p}}_{\mathbf{i}}\right)\tilde{\mathbf{p}}_{\mathbf{j}}^{*}\right] + \\ +\mathcal{R}\left[\frac{1}{2}\left(\mathbf{R}_{ij}^{T}\tilde{\mathbf{p}}_{\mathbf{j}}\right)\tilde{\mathbf{p}}_{\mathbf{i}}^{*}\right] - \frac{5}{\mathbf{R}_{ij}^{2}}\mathcal{R}\left[\frac{1}{2}\left(\tilde{\mathbf{p}}_{\mathbf{i}}^{\mathbf{T}}\mathbf{R}_{\mathbf{ij}}\right)\left(\tilde{\mathbf{p}}_{\mathbf{j}}^{\mathbf{T}}\mathbf{R}_{\mathbf{ij}}\right)^{*}\right] \end{pmatrix}, \tag{7.2}$$

where $\tilde{\mathbf{p}}_\mathbf{i} = \mathbf{4}\pi\varepsilon_\mathrm{m}\mathbf{Kr^3}\tilde{\mathbf{E}}_\mathbf{i}$ is the effective dipole moment, where $K = \frac{\varepsilon_\mathrm{p}^* - \varepsilon_\mathrm{m}^*}{\varepsilon_\mathrm{p}^* + 2\varepsilon_\mathrm{m}^*}$ is the Clausius-Mossotti factor, $(\cdot)^*$ denotes the complex conjugate, $\mathbf{R}_{ij} = \mathbf{R}_j - \mathbf{R}_i$, where $\mathbf{R}_i$, $\mathbf{R}_j$ are the respective position vectors of the particles i and j and $R_{ij} = \|\mathbf{R}_{ij}\|_2$ is the magnitude of the vector. The short range repulsive force arising from the interactions between the particles is usually introduced in a form (see [42, 41])

$$\mathbf{F}_{\mathrm{rep},ij} = 2F_\mathrm{max} e^{-100\left(\frac{\mathbf{R}_{ij}}{r} - 1\right)} \hat{\mathbf{R}}_{ij}, \tag{7.3}$$

where F_max is taken as the maximal DEP force and $\hat{\mathbf{R}}_{ij} = \frac{\mathbf{R}_{ij}}{R_{ij}}$ is a unit vector in the direction of $\mathbf{R}_{ij}$.

Expression (7.1) can be used either in the current form only for the simulation purposes or it can be further rearranged and utilized in the control algorithm. My goal will be to restate the expressions as the quadratic forms and thus allow a straightforward update of the existing optimization criterion.

For the sake of brevity, I will not include the whole derivation here, but rather describe the individual steps that are necessary to take in order to reformulate the problem and then I will only state only the final result. First, all the vector products present in the four individual summands in (7.2) has to be multiplied out and only the real part of them extracted where prescribed. During this process, some of the newly-emerged terms will mutually eliminate themselves. Next, we apply the same procedure we have done already few times before — substituting the electric intensities by a product of the input voltages, $\bar{\mathbf{u}}$ and the "unit" electric intensities $\bar{\mathbf{E}}_a$, and then use the transposition where necessary to enable factoring out the input voltages. After performing the final summation, $\mathbf{F}_{\mathrm{D},i}$ can be expressed as

$$\begin{aligned}
\mathbf{F}_{\mathrm{D},i,A} &= \bar{\mathbf{u}}_\mathrm{R}^T \mathbf{P}_{\mathrm{R,D},i,A} \bar{\mathbf{u}}_\mathrm{R} + \bar{\mathbf{u}}_\mathrm{I}^T \mathbf{P}_{\mathrm{I,D},i,A} \bar{\mathbf{u}}_\mathrm{I}, \\
\mathbf{P}_{\mathrm{R,D},i,A} &= \sum_{i=1, i\neq j}^{N} \left(\frac{6\pi\varepsilon_\mathrm{m}^2 r^6 \mathbf{R}_{ij} \|K\|_2^2}{R_{ij}^5} \sum_{a\in\{x,y,z\}} \left(\begin{array}{l} \bar{\mathbf{E}}_{\mathrm{R}a}^i \bar{\mathbf{E}}_{\mathrm{R}a}^{jT} + \mathbf{R}_{ij,a} \bar{\mathbf{E}}_{\mathrm{R}a}^i \bar{\mathbf{E}}_{\mathrm{R}A}^{jT} + \\ \mathbf{R}_{ij,a} \bar{\mathbf{E}}_{\mathrm{R}a}^j \bar{\mathbf{E}}_{\mathrm{R}a}^{iT} - \frac{5}{\mathbf{R}_{ij}^2} \sum\limits_{b\in\{x,y,z\}} \bar{\mathbf{E}}_{\mathrm{R}a}^i \bar{\mathbf{E}}_{\mathrm{R}b}^{jT} \end{array} \right) \right), \\
\mathbf{P}_{\mathrm{I,D},i,A} &= \sum_{i=1, i\neq j}^{N} \left(\frac{6\pi\varepsilon_\mathrm{m}^2 r^6 \mathbf{R}_{ij} \|K\|_2^2}{R_{ij}^5} \sum_{a\in\{x,y,z\}} \left(\begin{array}{l} \bar{\mathbf{E}}_{\mathrm{I}a}^i \bar{\mathbf{E}}_{\mathrm{I}a}^{jT} + \mathbf{R}_{ij,a} \bar{\mathbf{E}}_{\mathrm{I}a}^i \bar{\mathbf{E}}_{\mathrm{I}A}^{jT} + \\ \mathbf{R}_{ij,a} \bar{\mathbf{E}}_{\mathrm{I}a}^j \bar{\mathbf{E}}_{\mathrm{I}a}^{iT} - \frac{5}{\mathbf{R}_{ij}^2} \sum\limits_{b\in\{x,y,z\}} \bar{\mathbf{E}}_{\mathrm{I}a}^i \bar{\mathbf{E}}_{\mathrm{I}b}^{jT} \end{array} \right) \right), \\
a \; &\in \{x, y, z\}.
\end{aligned} \tag{7.4}$$

The notation in these expressions becomes unfortunately even more complicated. The superscripts i and j denote that the corresponding quantity is evaluated in the position of the respective ith or jth particle, e.g. $\bar{\mathbf{E}}_{\mathrm{R}x}^i = \bar{\mathbf{E}}_{\mathrm{R}x}(\mathbf{R}_i)$ is the vector composed of the real parts of the electric intensity x component evaluated in the position of the ith particle. Each of the components of this vector corresponds to the one electrode generating the electric field by 1 V voltage, (while the other are at 0 V).

The matrices defining the two quadratic forms in the above expressions, $\mathbf{P}_{\mathrm{R,D},i,A}$ and $\mathbf{P}_{\mathrm{I,D},i,A}$, can be easily used for the extension of the previously described $\mathbf{P}$ matrices from the optimization criterion, specifically

$$\mathbf{P}_{a,i} = \begin{bmatrix} \mathbf{P}_{\mathrm{cDEP},a,1,1} + \mathbf{P}_{\mathrm{R,D},i,a} & \mathbf{P}_{\mathrm{twDEP},a,1,2} \\ 0 & \mathbf{P}_{\mathrm{cDEP},a,2,2} + \mathbf{P}_{\mathrm{I,D},i,a} \end{bmatrix}, \; a \in \{x, y, z\}, \; i = 1 \ldots N. \tag{7.5}$$

Note that this time the matrices $\mathbf{P}$ have additional index i denoting the corresponding particle they belong to. Since the repulsive force is not dependent on the input voltages, it can be easily included in the optimization criterion the same way as, for example, the sedimentation force is. For clarity, I will show an example of the optimization task definition for the most general case, when both the amplitudes and the phases of the input voltages are allowed to change:

$$\begin{aligned}\bar{\mathbf{u}}^{\mathrm{opt}} &= \arg\min_{\bar{\mathbf{u}}} \sum_{i}^{N} \left[\begin{array}{l} \left(\sum\limits_{a\in\{x,y\}} \left|\bar{\mathbf{u}}^{T} \mathbf{P}_{a}\left(x,y,z\right)\bar{\mathbf{u}} + F_{\mathrm{rep},a,i} - F_{a}^{\mathrm{des}}\right| \right) + \\ + \left|\bar{\mathbf{u}}^{T}\mathbf{P}_{z}\left(x,y,z\right)\bar{\mathbf{u}} + F_{\mathrm{sed}} + F_{\mathrm{rep},z,i} - F_{z}^{\mathrm{des}}\right| \end{array} \right] . \quad (7.6) \\ &\mathrm{s.\,t.}\ u_i^2 + u_{n+i}^2 \leq U_{\max}^2 \end{aligned}$$

As indicated above, the interaction model can be further extended to account even for the simple hydrodynamic interactions. The motion of the particles induced by the DEP in a liquid medium causes a flow field felt by the other near particles. The particles will experience a force, which results from the hydrodynamic interactions with the original particle. According to [42], by solving the Stokes' equation for the two-particle case, the expression for the hydrodynamic force acting on the first particle due to the second one is

$$\mathbf{F}_{\mathrm{drag},1} = -6\pi\mu r\mathbf{v}_1 + 6\pi\mu r\frac{3r}{4R_{21}}\left(\mathbf{1} + \hat{\mathbf{R}}_{21}\hat{\mathbf{R}}_{21}^{T}\right)\mathbf{v}_2, \tag{7.7}$$

where μ is the dynamic viscosity of the medium, r is the particle radius, R_{21} is the distance between the two particles, $\mathbf{1}$ is the unit tensor, $\hat{\mathbf{R}}_{21}$ is the unit vector directing from the second to the first particle and $\mathbf{v}_1$, $\mathbf{v}_2$ are the velocities of the respective particles. This expression is in general valid only for the two particles interaction, but since the correction terms arising from N-body interaction are of high order and do not need to be taken into account, the expression can be generalized the following way [42]

$$\mathbf{F}_{\mathrm{drag},i} = -6\pi\mu r\mathbf{v}_i + \sum_{j=1,j\neq i}^{N} 6\pi\mu r\frac{3r}{4R_{ij}}\left(\mathbf{1} + \hat{\mathbf{R}}_{ij}\hat{\mathbf{R}}_{ij}^{T}\right)\mathbf{v}_j, \tag{7.8}$$

In order to use this hydrodynamic model for beads movement simulation, we use this expression instead of the original simple Stokes' law (see Eq. (3.1)). We substitute $\mathbf{F}_{\mathrm{drag},i} = -\left(\mathbf{F}_{\mathrm{E},i} + \mathbf{F}_{\mathrm{sed}}\right)$ and solve for the velocities $\mathbf{v}$. The $\mathbf{F}_{\mathrm{sed}} = \begin{bmatrix} 0 & 0 & F_{\mathrm{sed}} \end{bmatrix}^T$ is the vector of the sedimentation force. This can be done simply by solving the following system of linear equations into which the above expression can be reformulated

$$\begin{bmatrix} A_{11} & A_{12} & \cdots & A_{1N} \\ A_{21} & A_{22} & \cdots & A_{2N} \\ \vdots & \vdots & \ddots & \vdots \\ A_{N1} & A_{N2} & \cdots & A_{NN} \end{bmatrix} \begin{bmatrix} \mathbf{v}_1 \\ \mathbf{v}_2 \\ \vdots \\ \mathbf{v}_N \end{bmatrix} = \begin{bmatrix} \mathbf{F}_{\mathrm{E},1} + \mathbf{F}_{\mathrm{sed}} \\ \mathbf{F}_{\mathrm{E},2} + \mathbf{F}_{\mathrm{sed}} \\ \vdots \\ \mathbf{F}_{\mathrm{E},N} + \mathbf{F}_{\mathrm{sed}} \end{bmatrix}, \tag{7.9}$$

where $A_{ii} = 6\pi\mu r I$ (I is the 3×3 identity matrix), $A_{ij} = 6\pi\mu r\frac{3r}{4R_{21}}\left(\mathbf{1} + \hat{\mathbf{R}}_{ij}\hat{\mathbf{R}}_{ij}^{T}\right)$ and $\mathbf{v}_i = \begin{bmatrix} v_{i,x} & v_{i,y} & v_{i,z} \end{bmatrix}^T$ are the vectors contacting components of particle velocities for the three directions along the individual axes.

Now we are a step closer to take into account the model of the hydrodynamic interactions by the control algorithm. What only remains is to rebuild the control loop in such a way that the controlled quantity will not be the resulting forces acting on the particles, but rather directly the particle velocities. In fact, this is not as huge change as it may sound, because the velocity was already coupled with the force only by a simple linear relationship (3.1). After all, prescribing the velocity of the manipulated objects may seem even more meaningful than pursuing the force. The controller then based on these velocities computes the required forces $\mathbf{F}_{\mathrm{E},i} + \mathbf{F}_{\mathrm{sed}}$. This is done using again the relationship (7.9), this time with the roles of the knowns and the unknowns being switched. Having the required forces, the same optimization task as described above can be solved.

Both the electrostatic and the hydrodynamic interaction models were implemented in the simulation. Figure 7.8 shows a case, when two particles were placed 150 µm apart from each other above the parallel electrode array. Voltages of maximal the amplitude of 10 V with the alternating phase shifts of 0 ° and 180 ° were present on the electrodes. Although no DEP force acts in the direction parallel to the electrodes, the two beads approached each other and finally touched. This is caused by the electrostatic interaction. The attracting force is greater as the inter-particle distance declines.

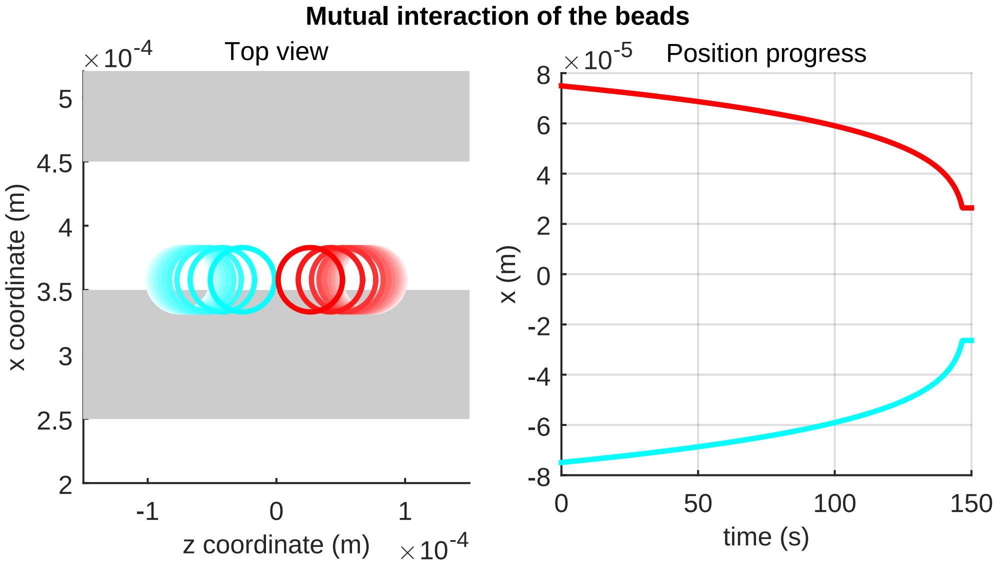

Figure 7.8. The simulation showing the mutual interaction of the two beads (electrostatic and hydrodynamic). The position in the y coordinate does not change since it corresponds to the stable equilibrium in given voltage configuration.

Unfortunately, a controller preventing this from happening is impossible to design for this type of an array. This is caused by an absence of the DEP force in the direction along the z axis. A controller taking into account the interaction forces has still a value at least for the direction along the x axis. In a case of the four-sector array, the abilities of this controller could be however better illustrated. Figure 7.9 shows altogether eight records of the simulated test scenario — five of them being controlled ignoring the mutual particle interactions (left column) and the other five taking them into account (right column). The task was to move one bead along the dashed line to the final position marked out by the cross, while the other particle should have stayed at its initial position (also denoted by the cross). The progress of the two beads positions in time is represented by the circles of different shades, each corresponding the end of one control period. Since the second bead passes during its motion by the first one in its close vicinity, the mutual electrostatic and hydrodynamic interactions are non-negligible. Indeed, from the first column of the figure (control ignoring the interactions) it can be seen that two particles sooner or later come together and the requested task is not fulfilled. On the other hand, the second set of the simulation results shows, that the controller taking the studied interactions into account prevents the particles from merging. Both will therefore reach their goal positions.

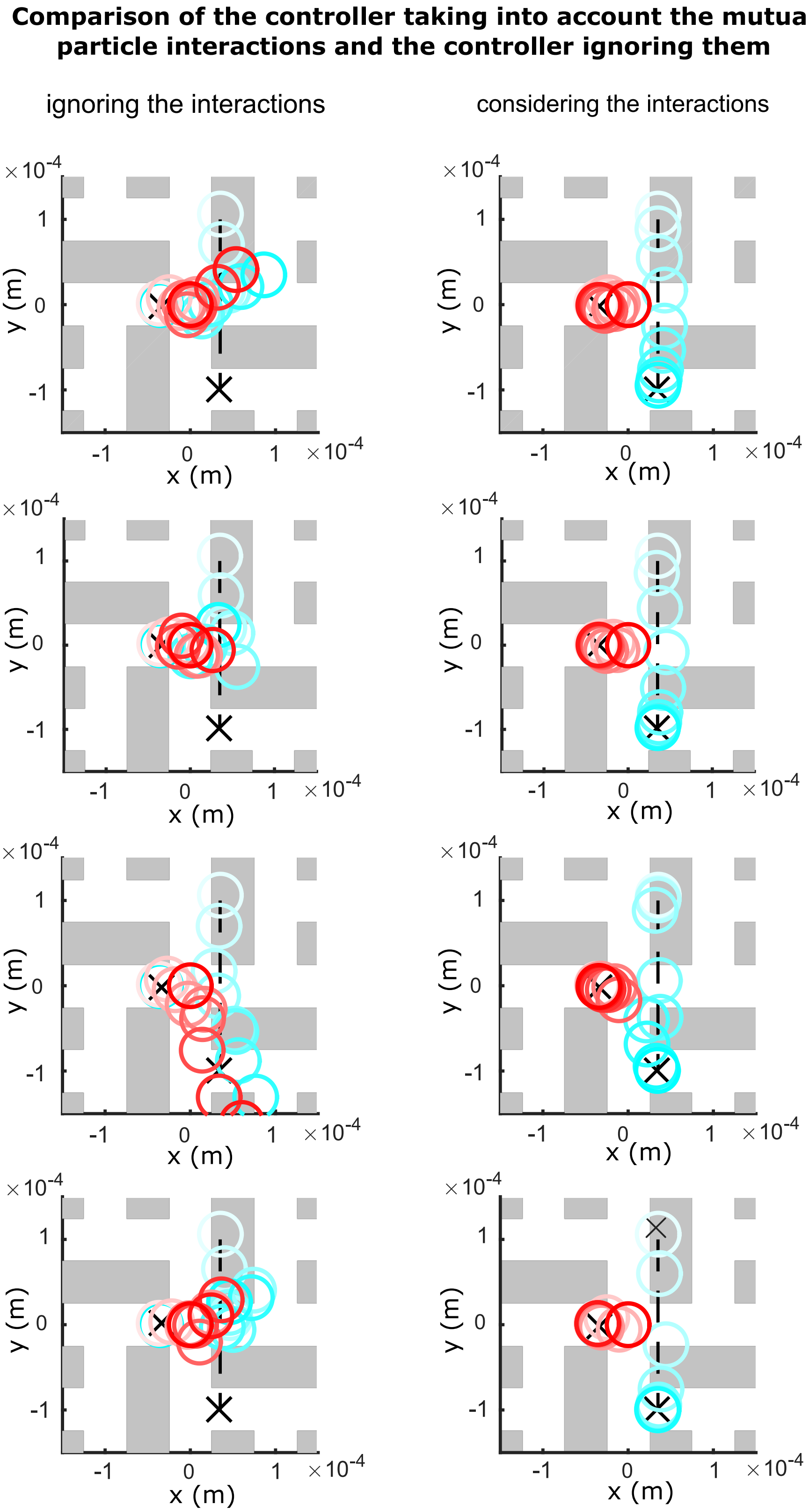

Figure 7.9. The comparison of the controller taking into account the particle interactions and the controller ignoring them while they are still present.

Chapter 8

Position uncertainty

In this chapter, I will analyze the effects of the uncertainty presence in the position measurements and I will suggest and test possible solutions to this issue. For the sake of simplicity, I will consider only the parallel electrode array and furthermore I will overlook the fact that the position measurement is available only in the direction along the x axis.

Since the optimization tries to ensure the desired force only exactly in the measured position, the particle may actually feel a quite different force if the measurement is imprecise and thus the true position of the bead is a little different. To evaluate this effect, I will introduce the concept of a *tolerable uncertainty*, meaning the uncertainty that still leads to a small enough error in the requested force. More specifically, we will express it as the maximal radius of a circular neighborhood of a point in which the directional error of the force is below 5 %. Taking into account the achievable measurement precision of the used laboratory setup, the tolerable radius of such an area should be preferably not less than 4 µm (which is the dimension corresponding to a one pixel of the camera image). Figure 8.1 shows an example of the tolerable uncertainty region (the darkest color) together with the inscribed circular point neighborhood (in the green color). The red circle marks the mentioned boundary of 4 µm. Since the green circle lies inside the red one, it is obvious that the minimal required size of the uncertainty region is not achieved in this case.

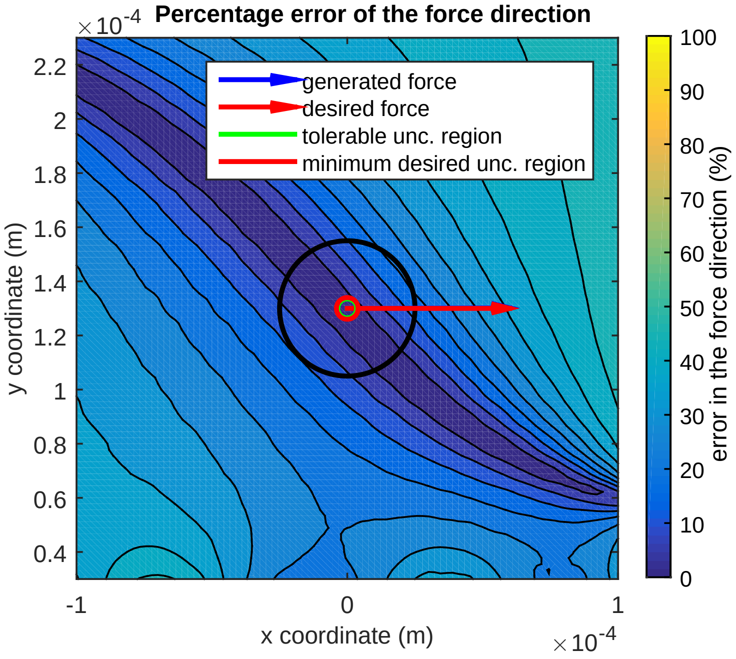

Figure 8.1. The example of the tolerable uncertainty region for the one particular bead position and the force requirement (the darkest region).

The size of the tolerable uncertainty can generally be different for the every given position and the desired force. In order to avoid the brute force evaluation, the matrices $\mathbf{P}_x$ and $\mathbf{P}_y$ can be studied instead. These matrices define the quadratic norms in the DEP force expressions (3.10) and are always enumerated for a particular position. Analyzing the spatial derivatives of their individual elements it is possible to identify the problematic ones, which are prone to big changes. Two samples of the matrices formed by these derivatives for the two different positions of the beads are shown in Figures 8.2 and 8.3.

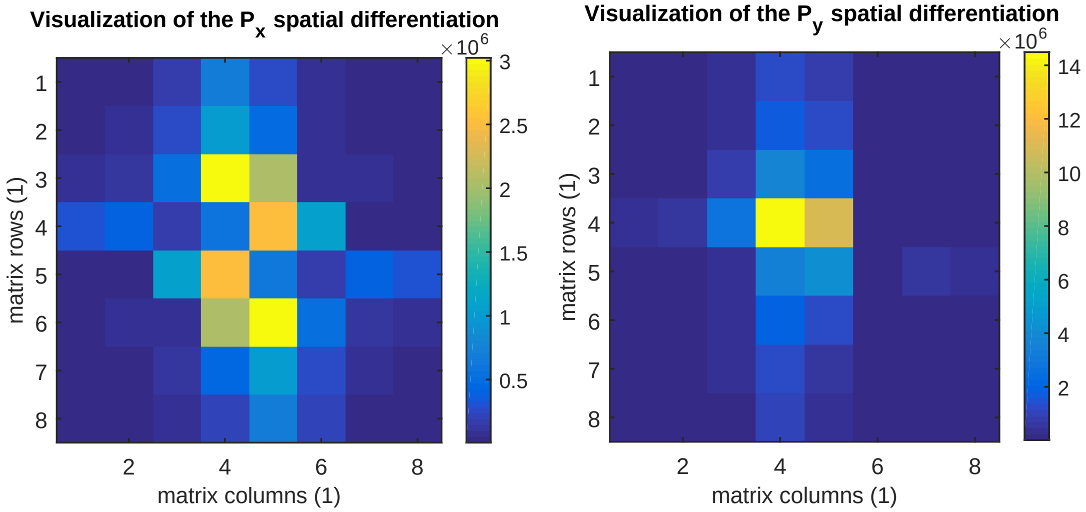

a) b)

Figure 8.2. Visualization of the spatial derivatives of the (a) $\mathbf{P}_x$ (b) $\mathbf{P}_y$ matrices evaluated at point $x = 0\,\mu\text{m}$, $y = 130\,\mu\text{m}$.

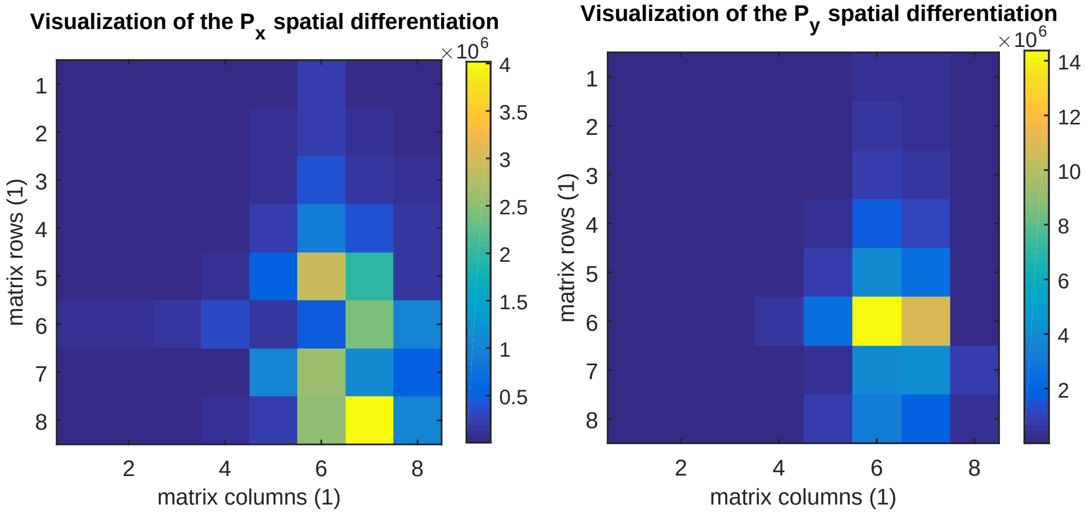

a) b)

Figure 8.3. Visualization of the spatial derivatives of the (a) $\mathbf{P}_x$ (b) $\mathbf{P}_y$ matrices evaluated at point $x = 400\,\mu\text{m}$, $y = 130\,\mu\text{m}$.

Typically, as it is apparent from the figures, these problematic elements are then multiplied by the voltage amplitudes corresponding to the electrodes near the particle position. (based on Eq. (3.10)). This is because the effect of the closest electrodes on the manipulated object is not only the strongest, but also the most unsteady. This means that the force changes dramatically with only a slight shift in the particle position. The causes are just the large derivatives (1^{st} and the 2^{nd}) of the electric intensity contribution close to the electrode which generated it. By applying a small voltage values to these electrodes, it is therefore possible to trade off the energetic efficiency of the manipulator for the extension of the tolerable uncertainty region.

The preceding consideration was implemented in two different ways. First, a simplistic approach introducing the different weights on the individual electrodes in a form

$$\bar{\mathbf{u}}^T \begin{bmatrix} w_1 & 0 & \cdots & 0 \\ 0 & w_2 & \ddots & \vdots \\ \vdots & \ddots & \ddots & 0 \\ 0 & \cdots & 0 & w_n \end{bmatrix} \bar{\mathbf{u}} \tag{8.1}$$

was tried. The numbers w_i $(i = 1 \ldots n)$ on the main diagonal are determined by evaluating a defined weighting function at the coordinates of the respective electrodes. This function can be chosen arbitrarily, but it should have one peak always at the position of the bead (e.g. the Gaussian curve can be used). This way, however, the non-diagonal interactions are dropped.

In the second approach, the weighting matrix was created directly based on the matrices $\mathbf{P}_x$ and $\mathbf{P}_y$. First, they were transformed according to

$$\mathbf{P}_{a,\text{diff}} = \mathbf{U}^T \mathbf{P}_a \mathbf{U}, \quad \mathbf{U} = \begin{bmatrix} 0 & 0 & \cdots & 0 \\ 1 & 0 & \ddots & \vdots \\ 1 & 1 & \ddots & 0 \\ \vdots & \ddots & \ddots & 0 \\ 1 & \cdots & 1 & 1 \end{bmatrix}, \quad a \in \{x, y\}, \tag{8.2}$$

which is the same relation that was used when optimizing over the control variable differences (see (5.4)). Then all the elements were replaced by the absolute value of their spatial derivatives (otherwise the positive and the negative elements could mutually compensate). The sum of these two modified matrices (multiplied by some factor defining the balance between the importance of this objective with respect to the other objectives calling for the force) is then taken to be the weighting matrix. This time also the non-diagonal interactions are incorporated. It is necessary that the absolute values of the control variable differences are weighted by this matrix the following way

$$\left|\bar{\mathbf{d}}^T\right| \left| \frac{\partial^2}{\partial x \partial y} \left[\mathbf{P}_{x,\text{diff}} + \mathbf{P}_{y,\text{diff}}\right](x, y) \right| \left|\bar{\mathbf{d}}\right| . \tag{8.3}$$

A few examples comparing the original controller and the improved one striving to enlarge the tolerable uncertainty region are depicted in Figure 8.4. Different bead positions and force requirements are captured. From these graphs, it is apparent that by incorporating the additional weights into the optimization criterion the tolerable uncertainty region indeed enlarged. In some cases, however, the improvement need not to very significant (for example in the second case, where the new region has a diameter of only 142 % of the original one, whereas in the first and the second example it is 694 % and 195 % of the original diameter respectively). It should be kept in mind that the improvement comes at the cost of the worst energy efficiency, because the controller intentionally prefers the usage of far actuators over the near ones.

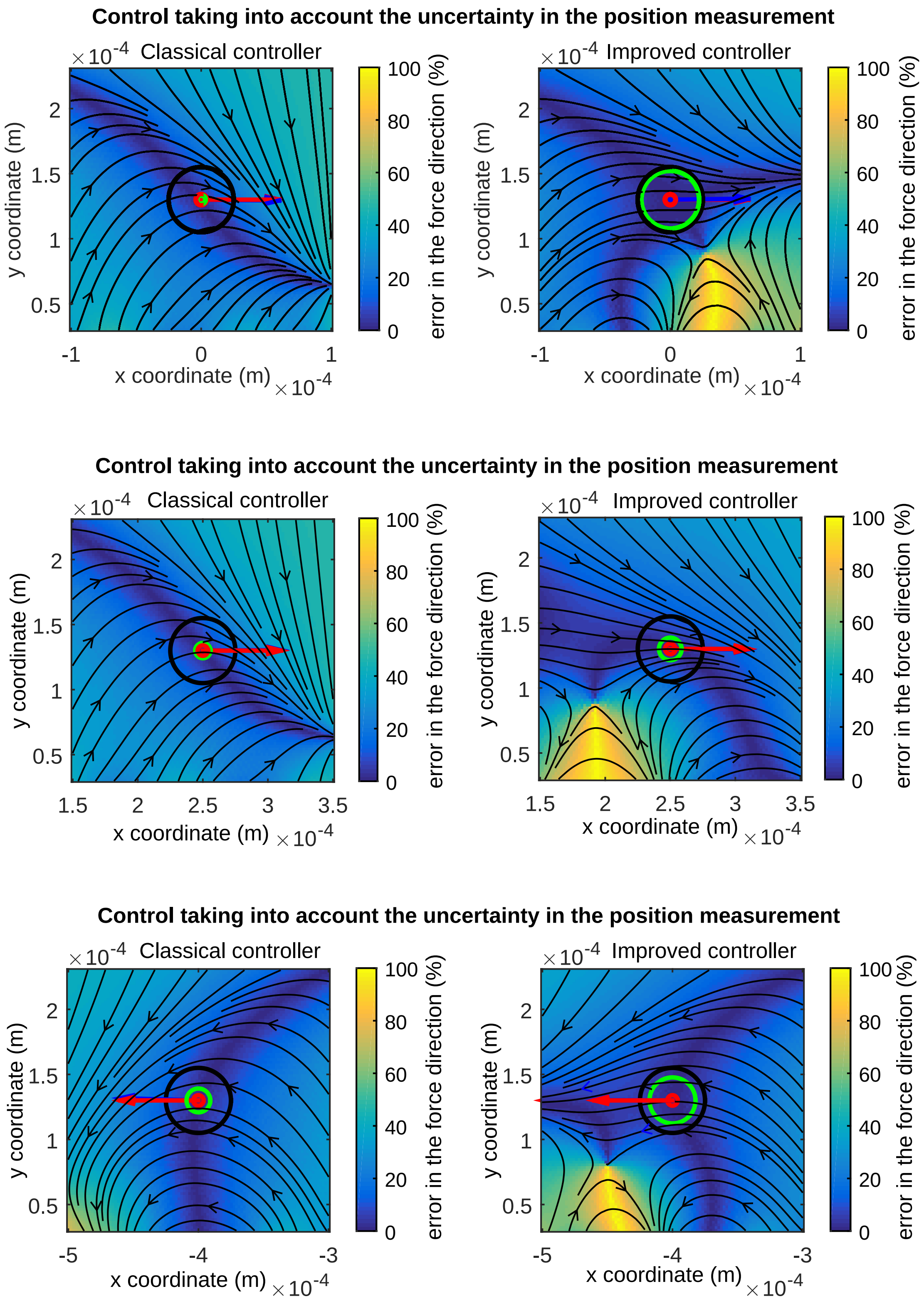

Figure 8.4. Comparison of the classical controller and the improved one taking into account the position measurement uncertainty.

Chapter 9
Conclusion

In this thesis I described the optimization based control system for the dielectrophoretic micromanipulation utilizing the parallel electrode array. Furthermore, I extended the optimization task formulation in such a way that both voltage amplitudes and mutual phase shifts can be utilized for the control. In the first place, this should allow not only the conventional but also the traveling wave dielectrophoresis control. Its induction is, however, impossible in the experiments, because of the currently available and used objects/medium combination. Apart from this, the phase control enabled me the utilization of a larger and more complicated four-sector electrode array. I conducted the experiments involving both of the arrays in order to demonstrate their manipulation capabilities and evaluate their performance. Surprisingly, the four-sector electrodes arrangement allows the manipulation even along arbitrary trajectories, which was not expected before. Next, I analyzed the system scalability with respect to the growing number of particles and electrodes and investigated a few methods dealing with the arising computational issues. No well working solution was however found. Further, I supplemented the system model by the mutual particle interactions and adapted the controller for taking them into account. Its function was then verified on simulations. Finally, I studied the sensitivity of the control algorithm to the position measurement uncertainties and I tested one of the possible approaches to the minimization of their effects. The modified optimization task was tested on a simplified simulation and the results seemed promising.

There are many potential improvements and also new ideas that would be worth of exploring in the future work. For example, the extension of the manipulator by adding the subsystem for the levitation height measurement (developed by my colleague Martin Gurtner in parallel with my thesis) could be done. Actually, the first trials of doing that have already started. Next, it would be great to come up with a better nonstochastic approach of solving the optimization task. Comparison of the simulated and actual mutual particle interactions would also be interesting. A big challenge would be the replacement of the deionized water and the polystyrene beads by some biological cells and solutions. This would be a huge step forward towards the intended applications.

References

[1] K.-F. Bohringer, K. Goldberg, M. Cohn, R. Howe, and A. Pisano. *Parallel microassembly with electrostatic force fields.* In: *1998 IEEE International Conference on Robotics and Automation, 1998. Proceedings*. 1998. 1204–1211 vol.2.

[2] Jaime Castillo, Maria Dimaki, and Winnie Edith Svendsen. Manipulation of biological samples using micro and nano techniques. *Integrative Biology: Quantitative Biosciences from Nano to Macro*. 2009, 1 (1), 30–42. DOI 10.1039/b814549k.

[3] Hywel Morgan, and Nicolas G. Green. *AC Electrokinetic: Colloids and Nanoparticles*. 1st edition edition. Philadelphia, PA: Research Studies Pr, 2002. ISBN 978086 3802553.

[4] David G. Grier. A revolution in optical manipulation. *Nature*. 2003, 424 (6950), 810–816. DOI 10.1038/nature01935.

[5] Albrecht Haake, and Jurg Dual. Contactless micromanipulation of small particles by an ultrasound field excited by a vibrating body. *The Journal of the Acoustical Society of America*. 2005, 117 (5), 2752–2760. DOI 10.1121/1.1874592.

[6] Nicole Pamme, and Claire Wilhelm. Continuous sorting of magnetic cells via on-chip free-flow magnetophoresis. *Lab on a Chip*. 2006, 6 (8), 974–980. DOI 10.1039/B604542A.

[7] W. A. Bonner, H. R. Hulett, R. G. Sweet, and L. A. Herzenberg. Fluorescence Activated Cell Sorting. *Review of Scientific Instruments*. 1972, 43 (3), 404–409. DOI 10.1063/1.1685647.

[8] Ronald Pethig, Vincent Bressler, Catherine Carswell-Crumpton, Yan Chen, Linda Foster-Haje, Marcos E. García-Ojeda, Richard S. Lee, Gary M. Lock, Mark S. Talary, and Keri M. Tate. Dielectrophoretic studies of the activation of human T lymphocytes using a newly developed cell profiling system. *ELECTROPHORESIS*. 2002, 23 (13), 2057–2063. DOI 10.1002/1522-2683(200207)23:13¡2057::AID-ELPS2057¿3.0.CO;2-X.

[9] Xujing Wang, Xiao-Bo Wang, and Peter R. C. Gascoyne. General expressions for dielectrophoretic force and electrorotational torque derived using the Maxwell stress tensor method. *Journal of Electrostatics*. 1997, 39 (4), 277–295. DOI 10.1016/S0304-3886(97)00126-5.

[10] Michael Pycraft Hughes. *Nanoelectromechanics in Engineering and Biology*. CRC Press, 2002. ISBN 9780849311833.

[11] Tomáš Michálek. *Maticové elektrodové pole pro dielektroforézu – základní řízení polohy*. 2013.
`https://dip.felk.cvut.cz/browse/pdfcache/michato4_2013bach.pdf`. bachelor's thesis.

[12] N. Manaresi, A Romani, G. Medoro, L. Altomare, A Leonardi, M. Tartagni, and R. Guerrieri. A CMOS chip for individual cell manipulation and de-

tection. *IEEE Journal of Solid-State Circuits*. 2003, 38 (12), 2297–2305. DOI 10.1109/JSSC.2003.819171.

[13] G. Medoro, C. Nastruzzi, R. Guerrieri, R. Gambari, and N. Manaresi. Lab on a Chip for Live-Cell Manipulation. *IEEE Design Test of Computers*. 2007, 24 (1), 26–36. DOI 10.1109/MDT.2007.21.

[14] G. Medoro, N. Manaresi, A Leonardi, L. Altomare, M. Tartagni, and R. Guerrieri. A lab-on-a-chip for cell detection and manipulation. *IEEE Sensors Journal*. 2003, 3 (3), 317–325. DOI 10.1109/JSEN.2003.814648.

[15] B. Edwards, and N. Engheta. Electric tweezers: negative dielectrophoretic multiple particle positioning. *New Journal of Physics*. 2012, 14 (6), 063012. DOI 10.1088/1367-2630/14/6/063012.

[16] M. Kharboutly, A Melis, M. Gauthier, and N. Chaillet. *2D open loop trajectory control of a micro-object in a dielectrophoresis-based device.* In: 2012. 950–955.

[17] M. Kharboutly, and M. Gauthier. *High speed closed loop control of a dielectrophoresis-based system.* In: 2013. 1446–1451.

[18] Jiří Zemánek, Tomáš Michálek, and Zdeněk Hurák. Feedback control for noise-aided parallel micromanipulation of several particles using dielectrophoresis. *Electrophoresis*. (in press),

[19] Karl F. Böhringer, Bruce R. Donald, Lydia E. Kavraki, and Florent Lamiraux. *A Distributed, Universal Device For Planar Parts Feeding: Unique Part Orientation in Programmable Force Fields*. 2000.
`http://link.springer.com/chapter/10.1007/978-1-4615-4545-3_1`.

[20] John W. Suh, R. Bruce Darling, Karl F. Böhringer, Bruce R. Donald, Henry Baltes, and Gregory T. A. Kovacs. *CMOS Integrated Organic Ciliary Actuator Arrays For General-Purpose Micromanipulation Tasks*. 2000.
`http://link.springer.com/chapter/10.1007/978-1-4615-4545-3_10`.

[21] Dan Reznik, Emil Moshkovich, and John Canny. *Building a Universal Planar Manipulator*. 2000.
`http://link.springer.com/chapter/10.1007/978-1-4615-4545-3_8`.

[22] Peter U. Frei, Markus Wiesendanger, Roland Büchi, and Lorenz Ruf. *Simultaneous Planar Transport of Multiple Objects on Individual Trajectories Using Friction Forces*. 2000.
`http://link.springer.com/chapter/10.1007/978-1-4615-4545-3_3`.

[23] M.P.J. Fromherz, and W.B. Jackson. Force allocation in a large-scale distributed active surface. *IEEE Transactions on Control Systems Technology*. 2003, 11 (5), 641–655. DOI 10.1109/TCST.2003.816410.

[24] S. Konishi, and H. Fujita. System design for cooperative control of a microactuator array. *IEEE Transactions on Industrial Electronics*. 1995, 42 (5), 449–454. DOI 10.1109/41.464606.

[25] Satoshi Tadokoro, Satoshi Fuji, Toshi Takamori, and Keisuke Oguro. *Distributed Actuation Devices Using Soft Gel Actuators*. 2000.
`http://link.springer.com/chapter/10.1007/978-1-4615-4545-3_11`.

[26] Mohamed Kharboutly, Michaël Gauthier, and Nicolas Chaillet. Modeling the trajectory of a microparticle in a dielectrophoresis device. *Journal of Applied Physics*. 2009, 106 (11), 114312. DOI 10.1063/1.3257167.

[27] *General simulated annealing algorithm - File Exchange - MATLAB Central*. `http://www.mathworks.com/matlabcentral/fileexchange/file_infos/10548-general-simulated-annealing-algorithm`.

[28] Z. Hurak, and J. Zemanek. *Feedback linearization approach to distributed feedback manipulation.* In: *American Control Conference (ACC), 2012*. 2012. 991–996.

[29] J. Zemanek, J. Drs, and Z. Hurak. *Dielectrophoretic actuation strategy for micromanipulation along complex trajectories.* In: *2014 IEEE/ASME International Conference on Advanced Intelligent Mechatronics (AIM)*. 2014. 19–25.

[30] Carlos Rosales, and Kian Meng Lim. Numerical comparison between Maxwell stress method and equivalent multipole approach for calculation of the dielectrophoretic force in single-cell traps. *ELECTROPHORESIS*. 2005, 26 (11), 2057–2065. DOI 10.1002/elps.200410298.

[31] T.B. Jones. Basic theory of dielectrophoresis and electrorotation. *IEEE Engineering in Medicine and Biology Magazine*. 2003, 22 (6), 33–42. DOI 10.1109/MEMB.2003.1304999.

[32] *fminsearchbnd, fminsearchcon - File Exchange - MATLAB Central*. `http://www.mathworks.com/matlabcentral/fileexchange/file_infos/8277-fminsearchbnd--fminsearchcon`.

[33] ”Jean-François Cardoso, and Antoine Souloumiac”. ”Jacobi angles for simultaneous diagonalization”. *”SIAM J. Mat. Anal. Appl.”*. 1995, ”17” (”1”), ”161–164”.

[34] Jiří Zemánek. *Noncontact parallel manipulation with micro- and mesoscale objects using dielectrophoresis*. 2009.

[35] Jakub Drs. *Čtyrsektorové elektrodové pole pro dielektroforézu*. 2012. `http://support.dce.felk.cvut.cz/mediawiki/images/1/1c/Bp_2012_drs_jakub.pdf`. bachelor’s thesis.

[36] *Cell Biology/Introduction/Cell size - Wikibooks, open books for an open world*. `http://en.wikibooks.org/wiki/Cell_Biology/Introduction/Cell_size`.

[37] A. Nedic, and A. Ozdaglar. Distributed Subgradient Methods for Multi-Agent Optimization. *IEEE Transactions on Automatic Control*. 2009, 54 (1), 48–61. DOI 10.1109/TAC.2008.2009515.

[38] Ye Ai, and Shizhi Qian. DC dielectrophoretic particle–particle interactions and their relative motions. *Journal of Colloid and Interface Science*. 2010, 346 (2), 448–454. DOI 10.1016/j.jcis.2010.03.003.

[39] Mohammad Robiul Hossan, Robert Dillon, Ajit K. Roy, and Prashanta Dutta. Modeling and simulation of dielectrophoretic particle–particle interactions and assembly. *Journal of Colloid and Interface Science*. 2013, 394 619–629. DOI 10.1016/j.jcis.2012.12.039.

[40] M. Washizu, and T.B. Jones. Dielectrophoretic interaction of two spherical particles calculated by equivalent multipole-moment method. *IEEE Transactions on Industry Applications*. 1996, 32 (2), 233–242. DOI 10.1109/28.491470.

[41] Annop Limsimarat, and Boonchai Techaumnat. Dynamic simulation using a multipolar model of particles under dielectrophoretic force. *Journal of Electrostatics*. 2007, 65 (10–11), 672–679. DOI 10.1016/j.elstat.2007.05.003.

[42] Yuan Lin, Gustav Amberg, Fredrik Aldaeus, and Johan Roeraade. Simulation of Dielectrophoretic Motion of Microparticles Using a Molecular Dynamics Approach. 2006, 1–10. DOI 10.1115/ICNMM2006-96095.

Appendix A
Specification

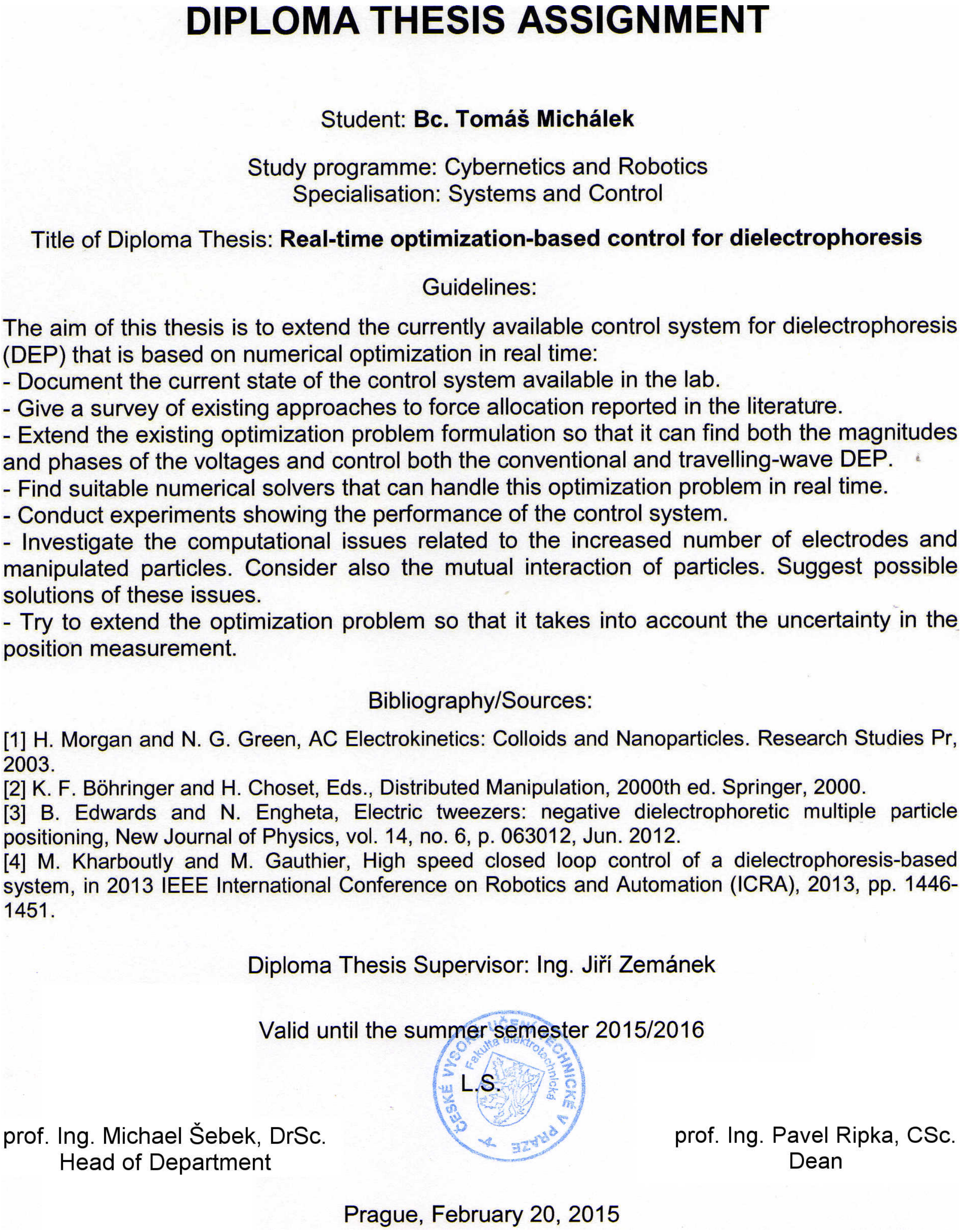

DIPLOMA THESIS ASSIGNMENT

Student: **Bc. Tomáš Michálek**

Study programme: Cybernetics and Robotics
Specialisation: Systems and Control

Title of Diploma Thesis: **Real-time optimization-based control for dielectrophoresis**

Guidelines:

The aim of this thesis is to extend the currently available control system for dielectrophoresis (DEP) that is based on numerical optimization in real time:
- Document the current state of the control system available in the lab.
- Give a survey of existing approaches to force allocation reported in the literature.
- Extend the existing optimization problem formulation so that it can find both the magnitudes and phases of the voltages and control both the conventional and travelling-wave DEP.
- Find suitable numerical solvers that can handle this optimization problem in real time.
- Conduct experiments showing the performance of the control system.
- Investigate the computational issues related to the increased number of electrodes and manipulated particles. Consider also the mutual interaction of particles. Suggest possible solutions of these issues.
- Try to extend the optimization problem so that it takes into account the uncertainty in the position measurement.

Bibliography/Sources:

[1] H. Morgan and N. G. Green, AC Electrokinetics: Colloids and Nanoparticles. Research Studies Pr, 2003.
[2] K. F. Böhringer and H. Choset, Eds., Distributed Manipulation, 2000th ed. Springer, 2000.
[3] B. Edwards and N. Engheta, Electric tweezers: negative dielectrophoretic multiple particle positioning, New Journal of Physics, vol. 14, no. 6, p. 063012, Jun. 2012.
[4] M. Kharboutly and M. Gauthier, High speed closed loop control of a dielectrophoresis-based system, in 2013 IEEE International Conference on Robotics and Automation (ICRA), 2013, pp. 1446-1451.

Diploma Thesis Supervisor: Ing. Jiří Zemánek

Valid until the summer semester 2015/2016

L.S.

ČESKÉ VYSOKÉ UČENÍ TECHNICKÉ V PRAZE
Fakulta elektrotechnická

prof. Ing. Michael Šebek, DrSc.
Head of Department

prof. Ing. Pavel Ripka, CSc.
Dean

Prague, February 20, 2015

Appendix B
Nomeclature

B.1 Abbreviations

Here is a list of all the abbreviations and symbols ocurring in the text:

MACS	magnetic-activated cell sorting
FACS	fluorescence-activated cell sorting
DEP	dielectrophoresis
CMOS	complementary metal oxide semiconductor
cDEP	conventional dielectrophoresis
twDEP	traveling wave dielectrophoresis
PDMS	polydimethylsiloxane
FEM	finite element method
SIL	software-in-the-loop
MST	Maxwell stress tensor method
ALE	arbitrary Lagrangian-Eulerian method
RAM	random access memory (here in metaphoric meaning of the operational memory)
FEX	Matlab file exchange
IP	interior-point algorithm
LP	linear programming
SA	simulated annealing
ITO	indium tin oxide

B.2 Symbols

$\mathbf{F}_\mathrm{d}$	frictional force in the Stokes' law
μ	dynamic viscosity of the fluid
r	radius of the spherical particle
$\mathbf{v}$	flow velocity relative to the object
x, y, z	space coordinates
$\mathbf{F}$	vector of the resulting force acting on the particle
F_a	component of the force vector corresponding to the direction of axis a ($a \in \{x, y, z\}$)
$\mathbf{u}$	optimization variable vector, depending on the context it can be the amplitude of sinusoidal voltage signal or its phase shift
u_i	ith component of the optimization variable vector u
$\bar{\mathbf{u}}$	vector of the optimization variables (the voltage amplitudes or the phase shifts corresponding to individual electrodes)
Φ	electric potential
Φ_i	electric potential generated by applying 1 V to the ith electrode and 0 V to the rest of the electrodes

$\bar{\boldsymbol{\Phi}}$	vector of the electric potential composed the elements of Φ_i
$\mathbf{E}$	electric field intensity vector
E_a	component of the electric field intensity vector corresponding to the direction of the axis a ($a \in \{x, y, z\}$)
$\bar{\mathbf{E}}_a$	vector of the electric intensity components for the axis a ($a \in \{x, y, z\}$), the ith vector component is the electric intensity given by the potential Φ_i.
$\mathbf{F}_{\mathrm{cDEP}}$	conventional dielectrophoretic force
$\mathbf{F}_{\mathrm{cDEP},a}$	component of the cDEP force corresponding to the axis a ($a \in \{x, y, z\}$)
k, k_1	multiplicative factor used in the cDEP force expression
ε_{m}	permittivity of the medium
ε_{r}	relative permittivity of the given material
ε_0	permittivity of the vacuum
$\varepsilon^*_{\mathrm{m}}$	complex permittivity of the medium
$\varepsilon^*_{\mathrm{p}}$	complex permittivity of the manipulated object
σ	conductivity of the given material
ω	angular frequency of the applied sinusoidal voltage
j	imaginary unit
Ψ_{ab}	partial derivatives of the a-component of the electric intensity along the axis b ($a, b \in \{x, y, z\}$)
$\bar{\boldsymbol{\Psi}}_{ab}$	partial derivative of $\bar{\mathbf{E}}_a$ along the axis b ($a, b \in \{x, y, z\}$)
$\mathbf{P}_a$	matrix defining the quadratic form based on which the cDEP force in axis a is calculated ($a \in \{x, y, z\}$)
${F_a}^{\mathrm{des}}$	desired force in the direction of the axis a ($a \in \{x, y, z\}$)
F_{sed}	sedimentation force acting on the particle
$\bar{\mathbf{u}}^{\mathrm{opt}}$	control variable vector with the results of the optimization
$U_{\max}$	maximum voltage amplitude applicable to the electrodes
x_{pred}	prediction of the particle x coordinate position at the time the next control action is applied to the electrodes
N	number of the particles
$\tilde{\Phi}$	potential phasor
Φ_{R}	real component of the potential phasor
Φ_{I}	imaginary component of the potential phasor
$\tilde{\mathbf{u}}$	vector of the voltage phasors corresponding to the individual electrodes
$\bar{\mathbf{u}}_{\mathrm{R}}$	vector of the real components of the voltage phasors corresponding to the individual electrodes
$\bar{\mathbf{u}}_{\mathrm{I}}$	vector of the imaginary components of the voltage phasors corresponding to the individual electrodes
$u_{\mathrm{R}i}$	real component of the voltage phasor corresponding to the ith electrode
$u_{\mathrm{I}i}$	imaginary component of the voltage phasor corresponding to the ith electrode
$\tilde{\mathbf{E}}$	phasor of the electric intensity
$\mathbf{E}_{\mathrm{R}}$	real component of the electric intensity phasor
$\mathbf{E}_{\mathrm{I}}$	imaginary component of the electric intensity phasor
$E_{\mathrm{R}a}$	component of the vector $\mathbf{E}_{\mathrm{R}}$ corresponding to the axis a ($a \in \{x, y, z\}$)
$E_{\mathrm{I}a}$	component of the vector $\mathbf{E}_{\mathrm{I}}$ corresponding to the axis a ($a \in \{x, y, z\}$)
$\mathbf{P}_a$	matrix defining the quadratic form based on which the total DEP force in the axis a is calculated ($a \in \{x, y, z\}$)
$\mathbf{P}_{\mathrm{cDEP},a,1,1}$	block components of the matrix $\mathbf{P}_a$ influencing the cDEP force contribution
$\mathbf{P}_{\mathrm{cDEP},a,2,2}$	block component of the matrix $\mathbf{P}_a$ influencing the cDEP force contribution
$\mathbf{P}_{\mathrm{twDEP},a,1,2}$	block component of the matrix $\mathbf{P}_a$ influencing the twDEP force contribution

$\mathbf{F}_{\mathrm{twDEP}}$	traveling wave dielectrophoretic force
$\mathbf{F}_{\mathrm{twDEP},a}$	component of the twDEP force corresponding to the axis a ($a \in \{x, y, z\}$)
k_2	multiplicative factor used in the twDEP force expression
$\mathbf{F}_{\mathrm{DEP}}$	total dielectrophoretic force constituting of the conventional and the traveling wave components
$\mathbf{F}_{\mathrm{DEP},a}$	component of the DEP force corresponding to the axis a ($a \in \{x, y, z\}$)
$\bar{\mathbf{u}}'$	extended optimization vector containing separately the real and the imaginary components of the voltage phasors corresponding to the individual electrodes
m_i	voltage amplitude correspondign to the ith electrode
ϕ_i	voltage phase shift corresponding to the ith electrode
n	number of the electrodes
$\mathbf{e}$	error in the force
α	a trade-off between the quality of the approximation and the control efforts
$\bar{\mathbf{d}}$	vector of the optimization variables formed by the mutual differences of $\bar{\mathbf{u}}$ elements
$\mathbf{F}_{\mathrm{E},i}$	total electrostatic force affecting the ith particle
$\mathbf{F}_{\mathrm{DEP},i}$	the DEP force acting on the ith particle
$\mathbf{F}_{\mathrm{D},i}$	electrostatic interaction force influencing the ith particle
$\mathbf{F}_{\mathrm{rep},i}$	repulsive force acting on the ith particle
$\tilde{\mathbf{p}}_{\mathbf{i}}$	effective dipole moment
K	Clausius-Mossotti factor
$\mathbf{R}_{ij}$	position vector starting at the position of the jth particle and ending at the position of the ith particle
$\hat{\mathbf{R}}_{\mathbf{ij}}$	unit vector pointing from the particle j to the particle i
R_{ij}	magnitude of the $\mathbf{R}_{ij}$ or the distance between the particles i and j
$\mathbf{F}_{\mathrm{drag},i}$	hydrodynamic force acting on the ith particle
$\mathbf{1}$	unit tensor